STUDY OF LUNAR LANDING SENSOR PERFORMANCE

INTERIM REPORT NO. 1

NAS8-5205

21 June 1963

Prepared for

George C. Marshall Space Flight Center

Huntsville, Alabama

SPACE TECHNOLOGY LABORATORIES, INC.

A Subsidiary of Thompson Ramo Wooldridge, Inc.

One Space Park, Redondo Beach, California

STUDY OF LUNAR LANDING SENSOR PERFORMANCE

INTERIM REPORT NO. 1

NAS8-5205

21 June 1963

Prepared for
George C. Marshall Space Flight Center
Huntsville, Alabama

Prepared by: J. E. Holland
Project Engineer

Approved by: J. Heilfron,
Associate Director
Guidance Laboratory

SPACE TECHNOLOGY LABORATORIES, INC.
A Subsidiary of Thompson Ramo Wooldridge, Inc.
One Space Park, Redondo Beach, California

Table of Contents

List of Illustrations

1. INTRODUCTION

The Lunar Landing Sensor Performance Study was directed to determining the sensor requirements for effecting a soft lunar landing from a direct cis-lunar trajectory or an orbital descent. Both beacon-assisted and nonbeacon-assisted landings were investigated. After the requirements were determined, suitable modifications to STELATRAC--STL's all solid-state X-band beacon-tracking radar--were made to permit it to fulfill the mission requirements, and estimates of the performance, power consumption, weight, volume, and reliability potential of the modified equipment are presented. The experimental activity was devoted to delivering an X-band solid-state power source supplying 100 milliwatts output at 10.34 gc with an input of 2 watts at 647 mc. In addition, experimental work was performed to confirm the efficacy of the analytical results in the area of the extended range altimeter.

The sensor requirements were initially predicated upon the Lunar Logisitcs Support[1] vehicle for the orbital descent profile and the solid fueled, high thrust-to-weight (F/W) spacecraft considered in the Analysis of Systems for Accurate Lunar Landing[2] for the direct descent.* The former is liquid fueled with a F/W = 0.5 to 2.0, depending upon spacecraft configuration at approach braking, and employs low altitude staging. The latter employs a F/W = 1.5 and the solid propellant precludes the provision of sensor data during the main braking interval. The high F/W of the solid fueled spacecraft reduced the range at which sensor data was required, even if it were to be employed to signify first burning. Since low altitude staging was employed, a gimbaled antenna beacon tracker was provided only on the landing stage. If no low altitude staging occurs, a single beacon tracker suffices throughout the descent.

(1) Study of Spacecraft Bus for Lunar Logistics System, Vol. I, Summary 22 December 1962, 8689-6007-TU-000, Space Technology Laboratories, Inc.

(2) Final Report - Analysis of Systems for Accurate Lunar Landing, 4 January 1962, 9990-6022-RL-000, Space Technology Laboratories, Inc.

*The work performed under these studies was capitalized on to reduce the effort required to determine sensor requirements so that the modifications to STELATRAC could be investigated more thoroughly.

The Multimission Module was introduced into the Study near its terminal phase. Its inclusion modified the sensor requirements established earlier in two ways. First, no low altitude staging is performed. Secondly, an initial F/W of only 1/3 requires first burning during the direct approach trajectory to occur at a high altitude and hence a long range from an emplaced lunar beacon or the lunar surface.

In addition to the equipment aspects of the design, appropriate choices of frequency (to minimize flame and dust effects), antenna location (to reduce thermal impact from rocket exhaust and ensure adequate visibility), interface signals (to mate with computer or control system), and checkout and verification provisions (to confirm operational status while on the launch stand and again prior to use after earth-moon transit) have to be made. Because of the strong interface with the spacecraft and its guidance and control implementation, only generalized comments can be made regarding the last two aspects of the sensor design. The duration of operational life may permit weight and other economies to be effected on some missions.

It should be borne in mind that sensor specifications predicated on the above types of spacecraft impose constraints upon the guidance law to be followed during the descent. That is, spacecraft maneuvering is minimized to reduce the angular coverage volume, vehicle velocities, and accelerations; and trajectories are flown which elevate the line-of-sight as viewed from the beacon above a minimum obscuration angle. Suitable antenna locations are selected on the spacecraft to provide the visibility necessary to avoid multipath errors. During the system design phase of any soft lunar landing program, cognizance of these and other constraints must be taken to effect an optimized solution.

A high altitude altimeter and a slant range tracker-velocity meter evolved from the study which would satisfy the requirements of the mission profiles. The high altitude altimeter can be readily integrated with STELATRAC so that a total sensor complement of two devices will fulfill all mission objectives. By separating the low and high altitude sensors, each can be designed for its specific function and specifications.

With the requirements determined, alternative sensor implementations were evaluated commensurate with STELATRAC. The extended range altimeter required a high duty factor modulation waveform to be able to perform at the high altitudes. During the initial phases of the study, frequency shifting to track altitude, conventional FM/CW, modulation sweeping as in STELATRAC, and 50 percent duty factor pulse repetition frequency (PRF) tracking were evaluated. The latter was selected as providing the most satisfactory solution to the problem by being integrable with STELATRAC, having an altitude capability limited only by available power sources and/or antenna aperture, and could be configured to perform as a range and range rate tracker in a beacon tracking mode to provide backup guidance. The technology associated with the PRF tracker is new, but variations of it have been employed in altimeters in the past. Lastly, the altitude tracking mode is adaptable to the doppler velocity meter, minimizing sensor complexity.

Horizontal velocity information is not required until the terminal maneuver phase, which allows a body-mounted antenna to be utilized for this function. Since the need for transmitter-receiver isolation is still acute for slant ranges of 10 km and vehicle attitudes of 45 degrees from vertical, a PRF slant range tracker continues to offer advantages, but the design parameters can be appropriately modified for the shorter ranges and different regime of vehicle dynamics.

The experimental program was directed towards the implementation of the all solid-state extended range altimeter as such a sensor is not available and is required for all nonbeacon-assisted lunar landings studied to date. If DSIF data is not utilized for lunar orbit injection, an altimeter capable of operation up to approximately 1,000 km altitudes is indicated. The extended range altimeter possesses this capability.* The essence of the implementation lies in the altitude tracker which must track over a wide dynamic range of altitudes at low signal-to-noise ratios in a spread spectrum environment. The gain of the altitude tracker varies with altitude, necessitating adaptive features in the tracking loop. Error sensing information is obtained by dithering the PRF so that a portion of the received pulse is eclipsed. Any eclipsing asymmetry amplitude modulates the received signal, giving rise to

*Needless to say, an enlarged antenna aperture and/or operation at a lower frequency is required to provide such a capability.

an error signal appropriate for driving the PRF oscillator so as to track the altitude. A frequency tracking loop is required to permit narrowbanding of the receiver for sensitivity enhancement. Thus the altimeter can be readily adapted, by adding two receiver channels and associated r-f circuitry, to provide horizontal velocity data. The modules designed and tested include the PRF oscillator and gate generator, synchronous demodulator for sensing the dither-induced amplitude modulation and frequency discriminator for the frequency tracking loop. Additional funding support is required to complete the design of the remaining units, incorporate them in STELATRAC, and demonstrate feasibility.

Lastly, a X-16 power source providing 100 milliwatts at X-band was fabricated, tested, and delivered as an Item of Work under the Lunar Sensor Performance Study Contract. This unit was previously developed at STL under the auspices of the Independent Research Program.

2. SUMMARY

The first phase of the Lunar Landing Sensor Performance Study was devoted to determining the necessary characteristics of sensors for soft landing on the moon with and without beacon assistance. For orbital descent, a liquid fueled vehicle with a relatively high thrust-to-weight ratio and employing low altitude staging was examined. Such a spacecraft is typified by the Lunar Logistics Support vehicle previously studied by STL (Reference 1). Sensors appropriate to direct approach trajectories were initially studied in the context of a high thrust-to-weight solid fueled vehicle staged at low altitudes. Near the end of the study period, the Multimission Module was subjected to an abbreviated analysis to determine applicable sensor specifications. A significant attribute of the latter spacecraft is its low thrust-to-weight ratio which increased the sensor range performance specification appreciably for the direct approach descent.

As it is preferable to reduce the number of sensors required for all mission profiles, the requirements were examined to ascertain the minimum sensor complement. With this as an objective, it was found that only two sensors were needed.* Their requirements are tabulated in Tables 2-1 and 2-2.

With the specifications established, attention was directed to the specifics of the sensors' design. For beacon assisted descents, no significant modifications of STELATRAC are necessary to fulfill the requirements even out to 700 km. As the angle tracking accuracy was specified as 0.3 degrees over the angular region measuring 110 x 60 degrees, an angle sensing implementation of modest accuracy but requiring minimum complexity circuitry was suggested. Solid-state conical lobing is such a mechanization. Body-mounted interferometer antennas are not recommended

*For the Multimission Module on a nonbeacon-assisted direct approach trajectory, first ignition occurs at altitudes a little below 700 km. The presently designed X-band altimeter cannot signify commencement of first ignition. However, by operating at a lower frequency and/or with a larger antenna aperture, it can provide such data. Additional study is indicated in this area to ensure compatibility with STELATRAC when the altimeter is operated at a lower frequency than the beacon tracker.

due to the need for extended angular coverage and sufficient gain to economize on transmitter power. If the interferometer assembly were positioned in discrete steps, gimbaling is still required and the reliability potential is not enhanced as latching motors, bearings, and angle indicators are called for. In addition, ambiguity resolving circuitry must be incorporated.

Table 2-1

Sensor Requirements for Beacon-Assisted Descents*

Quantity	Measurement Interval	Accuracy (3σ)
Range	0 to 700 km**	0.05%*** $\pm$1.0 m
Range rate	-300 to +2500 m/sec	0.15 m/sec
Range acceleration	0 to 27 m/sec^2****	---
Angular coverage	110° x 60°	0.3°
Inertial angular rate	6°/sec	0.03°/sec
Inertial angular acceleration	0.6°/sec^2	---
Vehicle angle rate	6°/sec	---
Vehicle angle acceleration	3°/sec^2	---
Beacon antenna coverage	2 lobes near horizon, diametrically opposed 1 lobe vertical	---

*This sensor is integrated with the extended range altimeter.

**Necessary for Multimission Module on direct approach trajectory.

***Accuracy of 0.05% required for orbit determination while in lunar orbit. Otherwise, accuracy specification can be relaxed to 0.5% $\pm$1.0 m.

****For high F/W spacecraft.

Table 2-2

Sensor Requirements for Nonbeacon-Assisted Descents

Extended Range Altimeter*

Quantity	Measurement Interval	Accuracy (3σ)
Altitude	1.8 to 220 or 700 km**	0.5%
Altitude rate	0. to 2500 m/sec	***
Altitude acceleration	0 to 9 m/sec^2****	---
Antenna coverage	60^o x 60^o	---

Slant Range Tracker-Velocity Meter

Quantity	Measurement Interval	Accuracy (3σ)
Slant range	0 to 10 km	1.0% $\pm$1.0 m*****
Slant range rate	0 to 550 m/sec	1.0% $\pm$0.5 m/sec
Slant range acceleration	0 to 9 m/sec^2	---
Lateral rate	0 to 120 m/sec	2.0% $\pm$0.5 m/sec
Angle from vertical	0 to 45^o	

*This sensor integrated with STELATRAC.

**Necessary for Multimission Module on direct approach trajectory.

***Difference altitude data if required.

****This value of acceleration is based on a F/W = 1.0 capability, wherein the thrust is directed vertically. A higher acceleration magnitude will not unlock the altitude tracking loop of the receiver, but will increase dynamic errors.

*****Bias accuracy of 1.0 m pertains near vertical incidence.

With the form of the beacon tracking sensor established, an investigation was made of the antenna diameter and transmitted power prescribed as a function of separation range for a receiver noise figure of 11 db and a minimum 6 db signal-to-noise ratio in the phase tracking loops subsequent to the imposition of ranging modulation. Figure 2-1 illustrates the tradeoffs possible with respect to these parameters. For reasons pertaining to the sensitivity of the extended range altimeter, an antenna diameter of 0.6 m and a power level of 100 mw was selected. Operation is at X-band where flame effects are negligible for operation with two RL10A engines. Table 2-3 summarizes the characteristics and performance capability of the beacon tracker.

Table 2-3

Beacon Tracker Characteristics

Operational frequency	X-band
Transmitter power	100 mw
Antenna	
Radar	Gimbaled 0.6 m diameter flat plate conically lobed.
Beacon	Two lobes near horizon diametrically opposed 30x30 degrees. One lobe vertical 50x50 degrees.
Antenna freedom	120 x 60 degrees
Range interval	0 to 700 km
Range accuracy (3σ)	$\pm$0.05% $\pm$0.6 m
Range rate interval	-300 to +2500 m/sec
Range rate accuracy (3σ)	$\pm$0.15 m/sec
Angle accuracy (3σ)	$\pm$0.3 degrees

	Weight (lbs)	Volume (m^3)	Power Consumption (watts)	Mean-Time Between Failures* OGO Type Parts (hours)
Radar transceiver	17.1	.0105	34	9,100
Radar antenna**	23	N/A	25	14,835
Beacon	15.5	.0095	30	10,333
Beacon antenna	1	N/A	0	282,486

*By parts screening and burn-in the reliability performance can be improved at an increase in cost. See Section 8 for expected improvements.

**Common to extended range altimeter.

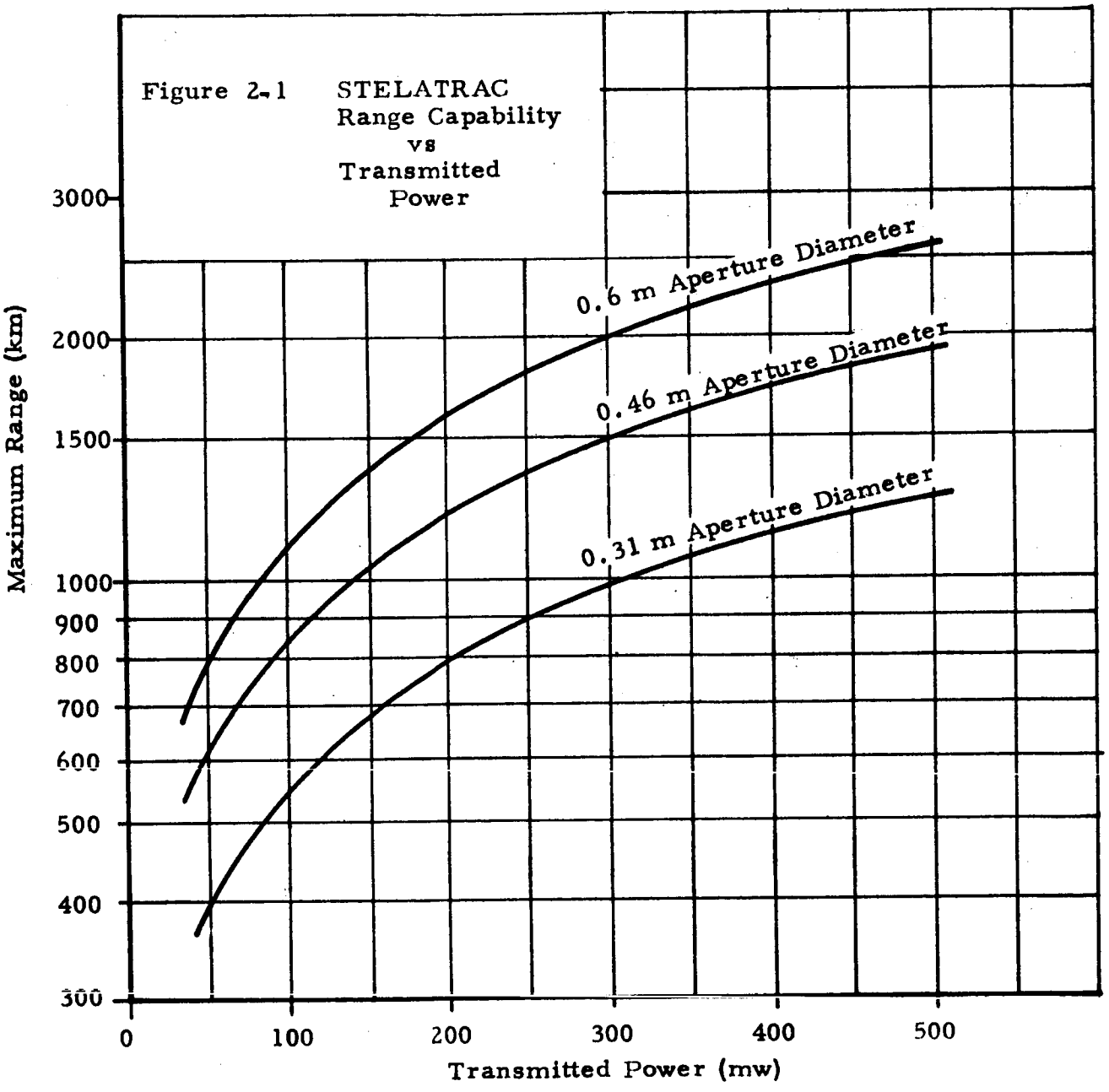
Figure 2-1 STELATRAC Range Capability vs Transmitted Power
Maximum Range (km)
3000
2000
1500
1000
900
800
700
600
500
400
300
0.6 m Aperture Diameter
0.46 m Aperture Diameter
0.31 m Aperture Diameter
0
100
200
300
400
500
Transmitted Power (mw)

The extended range altimeter is integrated with the beacon tracker to minimize components, with resultant saving in weight and volume. With this constraint, and the desire to operate up to altitudes of 220 km employing all solid-state techniques, the transmitter power-antenna aperture area product must be maximized and a high duty factor modulation envelope utilized. With the latter, discrimination against an extended range target accrues by means of a narrow radiation beamwidth, i.e. the beam limited case. For angle selectivity from a limited aperture, a large antenna diameter/wavelength ratio is indicated confirming the X-band frequency choice. Gimbaling of the extended range altimeter is readily achieved, although certainly not mandatory if the vehicle attitude is appropriately controlled, by employing the gimbaled beacon tracker antenna previously described. Since the beam is directed within a few degrees of vertical, at high altitudes for either orbital or direct descents, the specular character of the lunar terrain return can be capitalized upon to increase the sensitivity of the altimeter. It is shown in Section 4.4.2 that near vertical incidence the magnitude of the terrain scattering coefficient is 0 db or greater whereas at 20 degrees off vertical it is -5 db.

A high duty factor modulation envelope can be achieved by several techniques including frequency hopping between two frequencies separated by the i-f, conventional FM/CW, and PRF tracking. The latter is selected as requiring less advanced technology and is inherently compatible with STELATRAC and its solid-state power sources. Transmitter and receiver gating to the isolation levels required is readily performed by varactor bias modulation. Altitude error is established by dithering the PRF about its nominal value and synchronously detecting the spread spectrum return against the dither reference. In addition to coherently detecting, a very narrow band tracking loop can be implemented. A preliminary design analysis was made of the altitude (PRF) and velocity trackers to confirm design feasibility, select tentative control loop characteristics, and provide a basis for the error estimates. (Figure 4-13 is a block diagram of the altimeter.) A computer simulation of the altitude tracker using typical descent profiles is required to permit the final determination of the design parameters.

The altimeter is integrated with the beacon tracker as illustrated in Figure 2-2.*

The characteristics of the altimeter portion of the combined beacon tracker-extended range altimeter are tabulated in Table 2-4.

Table 2-4

Characteristics of Extended Range Altimeter

Operational frequency	X-band
Transmitted power	100 mw
Antenna coverage	60 x 60 degrees
Altitude interval	1.8 to 220 km
Altitude accuracy (3σ)	0.5% $\pm$1.5 meters**
Altitude rate interval	0 to 2500 m/sec

	Weight (lbs)	Volume (m^3)	Power Consumption (watts)	Mean-Time Between Failures OGO Type Parts (hours)
Transceiver	17.9	.0107	33	9,700
Antenna	Same as gimbaled antenna employed in beacon tracker.			

For nonbeacon-assisted terminal phase guidance, a body-mounted slant range tracker-velocity meter is recommended. Its radiation pattern consists of three beams, one oriented along the longitudinal axis of the vehicle and two beams displaced from this axis by 20 degrees and in orthogonal planes containing the vehicle axis. The squinted beams would be roll oriented to maximize the angle of incidence with respect to the lunar terrain. With this precaution, it is feasible to utilize a nongimbaled antenna.

Two altitude sensing modes are indicated due to the wide altitude spectrum. For higher altitudes or slant ranges, PRF tracking is utilized. When the PRF reaches 4 mc, it will be clamped, a reference will be injected

*A body-mounted antenna can be employed in lieu of the gimbaled beacon tracker antenna for missions wherein it is feasible to control the vehicle orientation when sensor data is required. The weight saving would be 19 lbs in such an eventuality and power consumption would be reduced. During the altimeter mode space stabilization of the antennas is not required if the beam is directed in discrete steps.

**With additional smoothing subsequent to that in the tracking loop.

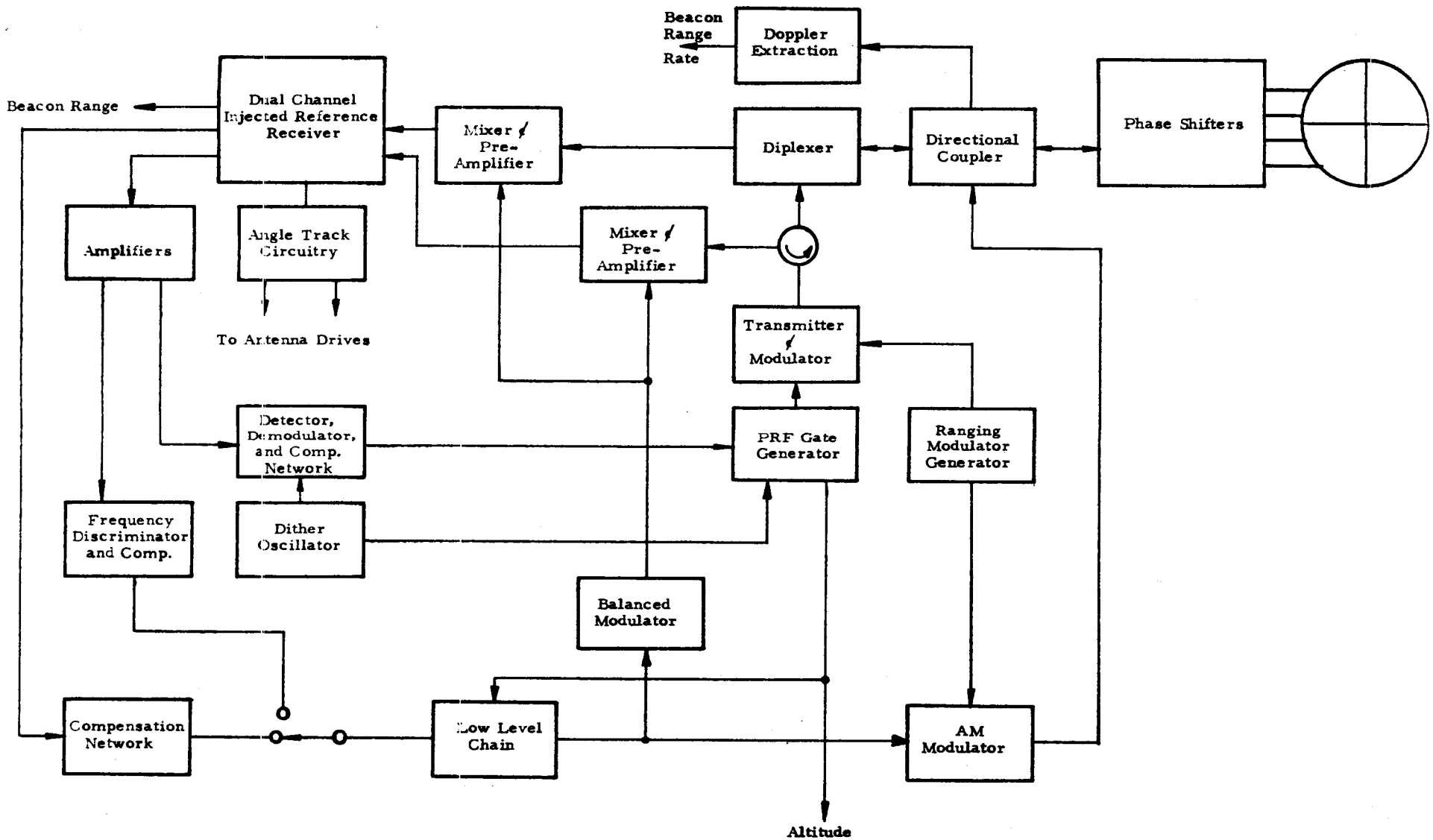

Figure 2-2 Integrated Beacon Tracker - Extended Range Altimeter

after the preamplifier, and range will be determined in a subsidiary module by phase comparison exactly as in STELATRAC. More than adequate energy will be received even though the return signal is eclipsed. With eclipsing, the eclipsing loss and the inverse square range dependence of the signal return balance each other, thus maintaining a constant signal level down to the altitude where the decay characteristics of the gated pulse are significant. (See Figure 4-19 for the block diagram of this sensor.)

Beam velocity in the longitudinal beam is determined by measuring the frequency of the return in a frequency tracker. The tracking oscillator is then used as a local oscillator signal for the two squinted beam channels so that the difference frequency of the two beams is directly established, thereby minimizing correlated errors. The design of the velocity tracker in the velocity meter is similar to that of the velocity tracker in the extended range altimeter. Thus component interchangeability is maximized for logistics purposes.

The characteristics of the slant range tracker-velocity meter are shown in Table 2-5.

Table 2-5.

Characteristics of Slant Range Tracker-Velocity Meter

Operational frequency	X-band
Transmitted power	100 mw
Angle from vertical	0 to 45 degrees
Slant range interval	0 to 10 km
Slant range accuracy (3σ)	
PRF tracking mode	1% $\pm$1.5 m
Phase tracking mode	1% $\pm$0.6 m
Slant range rate interval	0 to 550 m/sec
Slant range rate accuracy* (3σ)	
Along longitudinal beam	$<$0.75% $\pm$0.5 m/sec**
Difference of two beams	$<$0.5% $\pm$0.5 m/sec
Lateral rate interval	0 to 120 m/sec

*Velocities are referenced along beam axes. To determine worst case of lateral and longitudinal errors, many typical vehicle attitudes must be examined.

**A form of velocity aiding is assumed to reduce dynamic errors after smoothing.

(continuation of Table 2-5)

	Weight (lbs)	Volume (m^3)	Power Consumption (watts)	Mean-Time Between Failures OGO Type Parts (hours)
Transceiver	20	.0125	48	6,600
Antenna	4	N/A	Zero	211,864

3.0 SENSOR PERFORMANCE REQUIREMENTS

3.1 INTRODUCTION

The sensor performance specifications are intimately related to the mid-course guidance or orbital injection accuracy, spacecraft initial thrust-to-weight ratio (F/W and I_{sp}), IMU alignment and readout accuracy and performance capability, control system errors, allowable data smoothing interval, space-craft dynamics, guidance philosophy, and the desired terminal landing conditions. After performance parameters typical to the two classes of mission profiles have been established, the determination of the preferred sensor implementation can be made compatible with the contractual restriction that it be commensurate with STELATRAC--STL's all solid-state X-band beacon tracking radar.

For convenience, many of the sensor requirements and criteria were de-rived from Reference 2. Many of these requirements are suitable in general. However, some are peculiar to the use of relatively high initial thrust-to-weight solid propellant stages. This attribute minimizes the range-altitude at which sensor data is desired, while the solid propellant engine exhaust products impair the performance of r-f sensors so that no sensor data can be obtained during the main braking period. If a liquid engine such as the RL10A is employed, this limitation does not exist at X-band frequencies. For an orbital descent case where low altitude staging is employed, two beacon trackers are required for the beacon-assisted landing. It is impractical to locate a sensor just on the landing stage because of visibility limitations during main braking. (A boom was investigated for extending the antenna, but did not appear attractive because of installation, vibration and thermal control problems.) As a result, one beacon tracking radar is required on the deboost stage for main braking control, and another on the landing stage to control the hover and terminal landing conditions.

Sensor requirements for the Multimission Module were investigated. Two significant features of this spacecraft are its low initial thrust-to-weight ratio, high I_{sp} and high altitude staging. The former characteristics increase the initial range at which a sensor must perform, be it an altimeter

or beacon tracker, and the latter suggests that a sensor complement of these two devices is adequate for orbital descents and direct approaches if visibility can be assured in the latter instance during the main braking interval. This section of the report will discuss and present sensor requirements for lunar landing missions with respect to each of these landing approach profiles. The requirements are then condensed and presented in the Summary where it is shown that a combined beacon tracker-extended range altimeter and a slant range tracker-velocity meter will fulfill all r-f sensor requirements.

3.2 DIRECT APPROACH

So-called direct approach lunar landing trajectories can either be near rectilinear, i.e. a radial descent, or have obliquity angles up to about 50 degrees. If obliquity angles much larger are required, orbital descents are normally used. As a consequence, one can approximate the entire trajectory spectrum for lunar landing sensor purposes by considering the two extreme approaches, the radial direct approach and the orbital approach, and can be reasonably confident that the range of possibilities inbetween will be covered. This section then deals with the direct approach case.

3.2.1 Beacon-Assisted

The maximum range or altitude at which sensor data must be provided depends upon the initial thrust-to-weight ratio (F/W and I_{sp}) of the approaching spacecraft, position and angle errors at initiation of main braking, and the descent guidance law to be followed. The initial range for sensor operation is minimized if maximum thrust is utilized throughout the descent and a lower bound to the range is readily derived in this manner for a particular descent profile and F/W. For Reference 2, the maximum range was established as 280 km. Proper perspective regarding this result can be gained if it is appreciated that the F/W at initiation of main deboost for Reference 2 was 1.5 for the solid retro configuration and 0.9 for the H_2-O_2 engine.

The maximum spacecraft velocity occurs prior to braking and is approximately 2500 m/sec for a radial descent. (For a nonradial direct approach descent, the maximum range rate will be less than 2500 m/sec.)

The minimum rate is estimated to be 300 m/sec in the vicinity of the landing site. 300 m/sec was used for Reference 2 although lower terminal values might be desired for different configurations. The second derivative of range depends upon the initial thrust-to-mass weight ratio and I_{sp}. A maximum value of about 27 m/sec^2 at the end of main braking is representative for the spacecraft discussed in Reference 2.

The required angular coverage of the tracking antenna depends upon (1) the acquisition uncertainty angle, (2) the amount that the spacecraft pitches and yaws to achieve proper orientation of the thrust vector, (3) whether the spacecraft attitude control system assists in the search by moving the spacecraft, (4) the landing site in relation to the emplaced beacon, and (5) the trajectory near touchdown. During a previous study, Reference 2, the spacecraft tracked the LOS prior to main deboost, minimizing the antenna angular coverage requirements. After staging, a small (25 cm diameter) gimbaled antenna was required for vernier guidance purposes. A gimbal freedom of 100 to 110 degrees was indicated.

If landings offset from the beacon are effected only by overflying and landing beyond the beacon, this is adequate. For landings both before and beyond the beacon, it would be necessary to either roll the vehicle or have two mounting locations diametrically opposed. For purposes of this Study, only offset landing sites beyond the beacon are considered and the maximum offset is 18.5 km.

The low elevation angle coverage requirements of the beacon antenna are restricted to a quadrant of a sphere if only landings past the beacon are effected. Additionally, multipath generated by objects in front of the beacon can be discriminated against by proper shaping of the antenna radiation pattern.

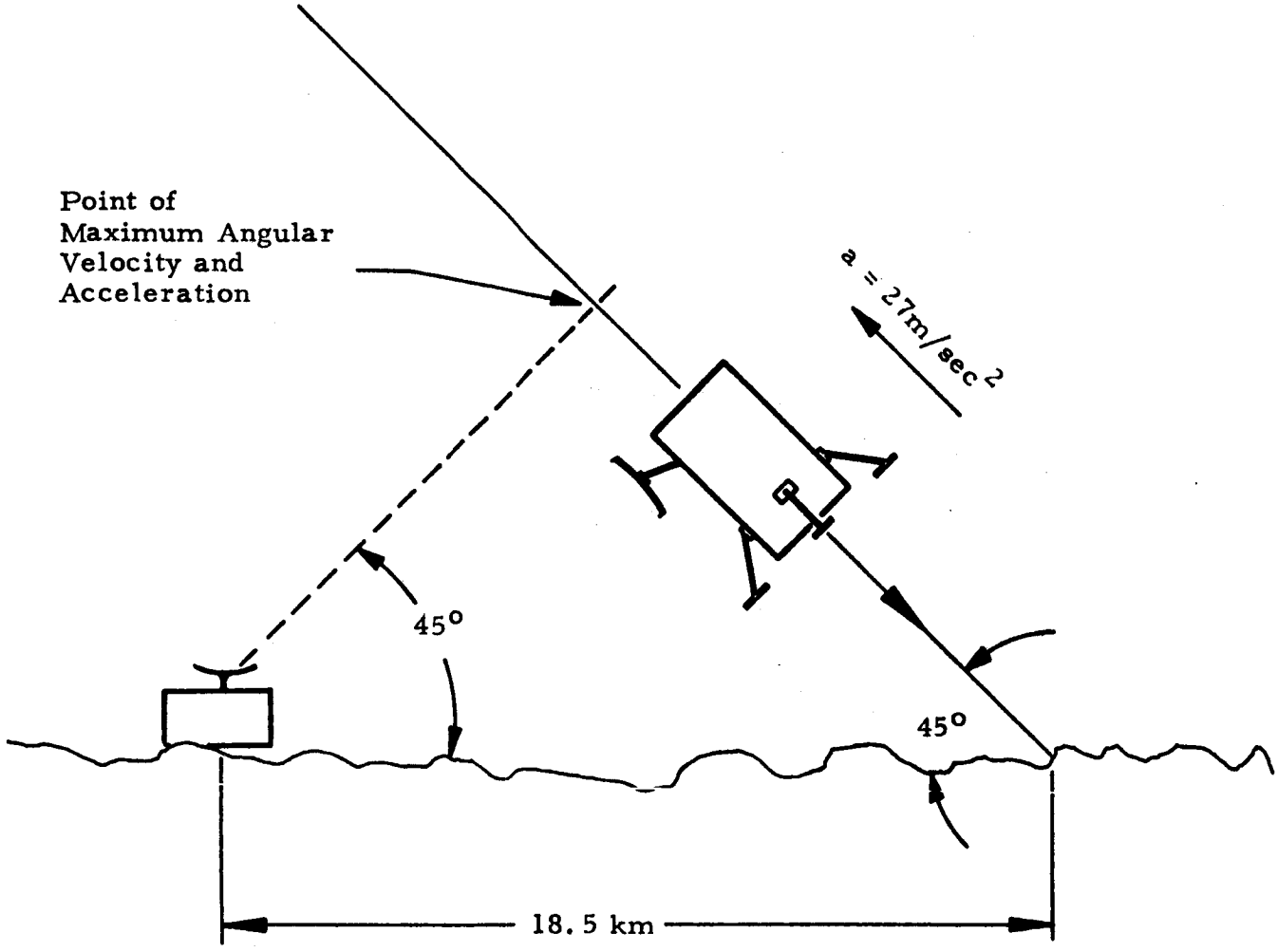

Figure 3-1 Touchdown Geometry for Estimating Maximum Angular Rates and Accelerations

The maximum angular rate and acceleration can be obtained from the flight profile. An approximate upper bound can be established by considering an acceleration capability of 27 m/sec^2 near touchdown (representative for the configuration of Reference 2), an offset of 18.5 km, and a 45-degree angle between the landing site vertical and the velocity vector. See Figure 3-1 for assumed geometry.

It is found that the inertial angle rates do not exceed 6°/sec (3.7°/sec for the geometry of Figure 3-1) and occur where signal levels are normally large. The inertial angular acceleration limit is approximately 0.6°/sec^2 (0.11°/sec^2 for the above geometry). Representative vehicle angle rate and acceleration limits are 6°/sec and 3°/sec^2, respectively, but again some variation from these limits can be anticipated, depending upon vehicle capability and guidance philosophy.

The performance of the sensor tracking loops described in subsequent sections of this report are such as to cause only small error magnitudes to be generated by even more severe vehicle dynamics.

The allowable measurement uncertainties can be set so that a negligible fuel consumption penalty during main braking is incurred and to ensure the requisite landing accuracy during the vernier phase. Prior to main braking, the beacon will be tracked in angle, and range and range rate will be measured. A range accuracy of 0.5 percent (3 σ) and an angle accuracy of 0.3° (3 σ) is indicated. The range rate for suitable landing control should be measured to 0.15 m/sec (3 σ). This is quite satisfactory for main braking. During the vernier phase, the above accuracies are sufficient if the slant range is established with a bias allowance of $\pm$1 m (3 σ). In addition, the angle rate error should be 0.03°/sec or less to ensure terminal landing accuracy for offset landing sites and to minimize fuel consumption during vernier guidance.

It is of interest to ascertain the landing accuracy achievable by the above described sensor when used with the spacecraft of Reference 2. For small offsets, less than 50 meters, the radius of 99 percent circular error probability (cep) is less than 2 meters. It generally has been conservatively assumed that altitude differences between the beacon and landing site will not be detectable outside of local survey of the spacecraft which carried the beacon.* Consequently for larger offsets, an altimeter is recommended. In addition, angular errors of the sensor cause serious altitude uncertainties at the greater offset distances. For offsets up to 6 km, the 99 percent cep increases to 40 m. For even greater offsets, a doppler navigator is necessary to prevent large lateral and lateral-rate landing errors due to beacon tracker angle and angle rate errors. The radius of 99 percent cep reaches 150 m for a 20 km offset. Clearly, these requirements can be relaxed as landing accuracy needs are lessened. However, the landing accuracies desired are typical and are within the sensor state-of-the-art.

For the beacon-assisted direct approach landing, the antenna requirements of the transponder must be established commensurate with the descent profile needs. During the initial phases of the descent, a small angular coverage region will suffice since the lateral uncertainties are

*Local surveillance may be effected by a TV camera or by astronaut visual observations.

small compared to the large ranges involved. However, for offset landings, the angular coverage of the beacon antenna near touchdown will have to extend over one quadrant of a sphere to provide for continuous beacon tracking by the landing spacecraft. Thus, for a direct approach trajectory, the main lobe of the beacon antenna, of approximately 50 degrees angular width (achievable with a 4 x 4 cm aperature at X-band) should be directed vertically and the radiation pattern tapered in the elevation plane to provide sufficient gain for landings past the beacon. Near the lunar horizon, i.e., for elevation angles of about 10 degrees, the antenna gain can be about one-hundredth that along the main beam axis and still provide signal levels comparable to those received shortly after acquisition. In addition to providing adequate antenna gain, the beacon antenna must be sited so as not to be obscured by nearby vehicles or other reflective objects or terrain, all of which can act as significant sources of multipath signals, causing degradation of range and angle tracking performance. It will be shown in Section 3.3.1, that for an orbital descent the beam axis should be oriented close to the horizon and not vertically. To ensure coverage for both approaches switching between antennas via a semiconductor switch is suggested. Each antenna aperture is small and a dual antenna installation will increase the transponder weight by less than one pound.

In Reference 2 several of the vehicles employed solid propellant rockets during main braking which impaired or precluded the receipt of guidance data during engine firing. Just prior to braking, the spacecraft-lunar beacon link is used for a navigation fix. The spacecraft is initially aimed, at thrust initiation, at a point biased slightly above the desired landing site. During the subsequent vernier phase, the necessary adjustments for variations in solid rocket performance and spacecraft weight are made. (With liquid fueled engines, e.g. the RL10A, sensor data could be obtained throughout the thrust interval to reduce position and velocity uncertainties at initiation of the vernier phase. This would allow for a shorter vernier period with a smaller initial velocity. In addition, the RL10A can be considered for future applications to have a throttling capability for use during vernier.)

Lastly, adequate LOS visibility clearance to reduce multipath to permissible limits should generally be available. This may necessitate extended antennas or a sensor on each stage if the spacecraft subsequently stages.

3.2.2 Nonbeacon-Assisted

The sensor combination required for a nonbeacon-assisted direct approach landing includes an altimeter to determine altitude and altitude rate prior to main braking supplemented with a velocity meter for the terminal phase to measure horizontal velocity components.

The altimeter, if employed to initiate main braking, would require approximately the same range capability as the beacon tracker, especially if the approach is near rectilinear. As will be shown in 4.2, an all solid-state altimeter with an altitude capability of >220 km will require a power output in excess of 100 mw*, an antenna aperture larger than 0.6 m in diameter, or a data smoothing time of greater than 20 seconds. For missions occurring during the next three years, it may be more advantageous to employ DSIF data to initiate main braking, particularly if the start of main deboost is in sight of the earth. In this case, the altimeter could be sized to terminate the main braking interval.** However, reliability considerations suggest a combined altimeter-DSIF configuration to initiate the main braking phase. Such a mechanization is feasible if a liquid engine is used. In this manner, a minimum weight beacon tracker-high altitude altimeter can be configured. If a solid fueled engine were employed, sensor altitude data would be available only upon thrust termination, which will increase the initial vernier altitude and other dispersions.

As before, the maximum altitude rate to be measured is 2500 m/sec. The maximum acceleration to be experienced during operation of the high altitude altimeter is 9 m/sec^2 and increases to about 27 m/sec^2 during the vernier phase.

---

*Within the next year, an X-band, 1-watt power source will become a reality and would permit the mechanization of a 600 km solid-state altimeter.

**Alternately, a horizon sensor could be utilized.

A generally suitable altitude accuracy for an efficient descent is 0.5 percent (3σ). The altitude rate should be measured to one percent (3σ). However, these requirements can be relaxed for some increase in deboost velocity requirements.

Look angle uncertainties for the high altitude altimeter used only for main braking initiation are small for a direct approach and require no antenna gimbaling.

The complimentary sensor required for vernier guidance purposes is an altimeter-velocity meter. If low altitude staging occurs, a natural point for mode switching presents itself at that time. The vehicle attitude may vary up to 45 degrees from local vertical and, if the antenna is body-mounted during vernier guidance, the altimeter becomes in fact a slant range measuring instrument. The ranging performance requirements are discussed first.

The slant range accuracy specification is determined by the dependence of lateral rates upon range (a scale error phenomenon) and the altitude at which vernier burning is terminated or final free fall is to occur (a bias effect). A one percent slant range uncertainty is tolerable at the longer distances and is within current sensor technology. It should be borne in mind that the range varies appreciably over the radiation beam-width for incidence angles of 45 degrees and is approximated by

$$\frac{\Delta R}{R} \simeq \Delta\theta \operatorname{ctn} \theta$$

where

$\frac{\Delta R}{R}$ = fractional range change over beamwidth

θ = depression angle

$\Delta\theta$ = half-power two-way beamwidth (radians)

For $\Delta\theta = 3.0$ degrees, $\theta = 45$ degrees, $\frac{\Delta R}{R} = 5\%$ across the beamwidth. Fortunately, the proposed altitude tracker is only susceptible to a small portion of the fractional range change as discussed in Section 4.3.

Near touchdown, the scale error is negligible (excluding for the moment dust effects) and bias errors predominate. If the vernier engine cut-off occurs at an altitude under 10 m, the permissible altitude bias error is typically 1 m. For any particular spacecraft, the period of free fall will be determined by structure limitations, type of cargo, need for spacecraft remaining upright for discharge of cargo, and lunar surface characteristics.

A maximum range rate of 300 m/sec can be expected for the vernier phase at altitudes occurring below 10 km. The accuracy required in the measurement of longitudinal or lateral rates is 1% $\pm$ 0.5 and 2% $\pm$ 0.5 m/sec respectively. This leads to a lateral landing velocity $<$1 m/sec, which definitely does not create an excessive structural weight penalty. In fact, the landing structure criteria is generally much larger than this.

During the final vernier phase, the vehicle attitude may vary by 45 degrees, but will approach vertical near touchdown. Fortunately, it is not necessary to gimbal the antennas of the velocity meter-slant range tracker, as the three beam antenna configuration discussed in Section 4.3 will always intercept the lunar surface at angles equal or less than 45 degrees from the local vertical.

3.3 ORBITAL DESCENT

3.3.1 Beacon-Assisted

The requirements for a beacon-assisted descent are similar in some respects to those for a direct approach. The significant sensor changes are due to changes in the range measurement interval, reduction in range acceleration, and the transponder antenna beam orientation.

Prior to thrusting out of lunar orbit, the beacon will be acquired at a range of approximately 600 km* and will be tracked to provide range, range rate, and line-of-sight angle data. The highest value of acceleration anticipated is 6.5 m/sec^2 for the C-5 spacecraft of Reference 1. The spacecraft pitch attitude may be varied to maximize the tracking interval and/or eliminate the requirement for initially gimbaling the antenna. As viewed from the transponder, the orbiting spacecraft can be picked up at low

*Based on a nominal 15-degree minimum elevation angle and a 200 km orbital altitude.

elevation angles, 15 to 20 degrees being typical, and remain visible from the transponder site for a total elevation angle excursion of about 140 degrees. For the orbital descent mission, maximum range occurs near the horizon in opposition to the direct approach case wherein the transponder antenna beam axis should be directed vertically. Several transponder antenna configurations come to mind which are compatible with orbital descent requirements. For example, a pair of radiation lobes can be diametrically opposed and elevated 20 degrees above the horizon to provide deboost coverage from either direction. The pattern gain can be shaped so that the power density resulting from the decrease in range will accommodate the loss in antenna gain as the elevation angle increases near the landing site. A half-power beamwidth of 20 degrees in the azimuthal plane is ample to provide sufficient antenna gain for at least ten consecutive orbital passes.

3.3.2 Nonbeacon-Assisted

For the nonbeacon-assisted descent from lunar orbit, an altimeter will be employed at high altitude, supplemented at lower altitudes by a horizontal velocity meter. The maximum range for the altimeter is essentially determined by the orbital altitude, 200 km. The spacecraft can be steered while in orbit so as to keep the antenna pointing downward to within $\pm$ 2 degrees. Vehicle steering is also feasible during the Hohmann transfer. The maximum altitude rate is near 300 m/sec for nominal Hohmann transfer trajectories.*

The altitude should be measured to 0.5 percent and altitude rate to 1 percent, comparable to the direct approach trajectory requirements.

The requirements for the vernier phase slant range tracker-velocity meter are equivalent to those for the direct approach, assuming comparable spacecraft and landing accuracies.

*For non-Hohmann transfers, this altitude rate can increase to 600 m/sec for steep transfer trajectories.

3.4 MULTIMISSION MODULE

The employment of the Multimission Module in lieu of a low altitude staging spacecraft modifies some of the previous results, especially those for the direct approach trajectory. The results of the preliminary analysis which could be accomplished in the remaining study time are presented in this section. A more detailed study involving the investigation of alternative trajectories and determining the pertinent sensor parameters appropriate to each should be made.

3.4.1 Direct Approach

3.4.1.1 Beacon-Assisted Descent

An analysis was performed to estimate the trajectory parameters of the Multimission Module vehicle using a rectilinear approach trajectory. The following assumptions were made yielding approximate results suitable for deriving sensor requirements.

a) Equal mass ratios for each phase, i.e., equal ideal velocity contributions*
b) 72-hour transit time
c) Constant lunar gravity during powered descent
d) An initial weight at first stage ignition of 90,000 pounds
e) Constant thrust during descent
f) Second stage ignition immediately following first stage burnout
g) Zero velocity terminal condition at the lunar surface

The propulsion characteristics and weight history are tabulated in Table 3-1.

Table 3-1

Propulsion and Weight Data

Engines: Two RL10A engines in each stage
Thrust: 15,000 pounds per engine
Specific Impulse: 430 seconds
Propellants: Hydrogen/Oxygen

First Stage Ignition Weight	90,000
Propellants Used	-25,484

*Changes to this assumption will not dramatically alter the conclusions, especially regarding sensor requirements.

(continuation - Table 3-1)

First Stage Burnout Weight	64,516
Jettison Weight	-7,220
Second Stage Ignition Weight	57,296
Propellants Used	-16,224
Second Stage Burnout Weight	41,072
Jettison Weight	-5,800
Total Weight on Moon	35,272

With the above assumptions, the following data was obtained pertaining to ignition altitude and maximum velocity and acceleration.

Table 3-2

Multimission Module Direct Approach Trajectory Characteristics

	Stage 1	Stage 2
Altitude at Ignition (km)	670	130
Maximum Velocity (m/sec)	2230	1250
Maximum Acceleration (m/sec^2)	4.6	7

A major difference between the spacecraft of Reference 2 and the Multimission Module lies in the need for longer range performance due to lower initial F/W and higher I_{sp}, if sensor data is to be employed for initiation of main deboost. Because of the long burning times, lunar gravity is also more significant. Lastly, the Multimission Module uses liquid fueled engines, permitting the employment of r-f sensors while thrusting, in contrast to the solid propellant employed in most of the spacecraft considered in Reference 2.

The inertial and vehicle angular rates and accelerations are anticipated to be similar to the vehicles in Reference 2. Vehicle dynamics depend upon attitude control system characteristics, and the values presented in Reference 2 are considered typical.

3.4.1.2 Nonbeacon-Assisted Descent

For the nonbeacon-assisted descent case, the altimeter altitude requirements are comparable to the beacon range requirements. The need for altitude data at first stage ignition can be obviated if a horizon

sensor or DSIF data is employed initially. The altimeter could be used for termination of first stage burning or start of second stage ignition at an altitude of approximately 150 km. Specific studies and appropriate error analyses should be conducted to derive the performance penalties associated with this technique. However, penalties are not expected to be overly severe.

Anticipated vehicle attitude changes are so small at high altitudes that antenna gimbaling is not necessary for the nonbeacon-assisted descent. As the altimeter antenna is gimbaled, since it is common with the beacon tracker, the gimbals can be locked prior to launch. Conversely, it could be replaced with a fixed antenna assembly if it were established that a beacon would not be provided. At lower altitudes, a change of sensors will be effected, but gimbaling is not necessary for typical spacecraft. A minimum altitude of 10 km is suggested for the mode change. At the lower altitude range, the requirements for the slant range tracker-velocity meter are the same as presented in Section 3.2.2.

3.4.2 Orbital Descent

3.4.2.1 Beacon-Assisted Descent

Two constant, continuous thrust flight profiles were provided by MSFC to be used for deriving sensor requirements for descents from a 185 km circular lunar orbit. They represented descent extremes in that one was a powered descent* directly from orbit and the other involved a Hohmann transfer to a periselenum of 25 km and then a descent to the lunar surface. The data provided was processed to give the slant range and range rate to the landing site** elevation angle as viewed from the

*The iteration period employed was five seconds. As a result, the profile data near the terminal point was not used in the computations.

**In addition to the descent trajectories, beacon acquisition and ignition loci for constant, continuous thrust descents were obtained. For a given minimum beacon elevation angle, the range at which beacon acquisition can be effected can be established as well as the central angle traversed during the descent.

landing site, and the spacecraft LOS angle referenced to the initial surface normal. These parameters are defined more fully in Figure 3-2, below.

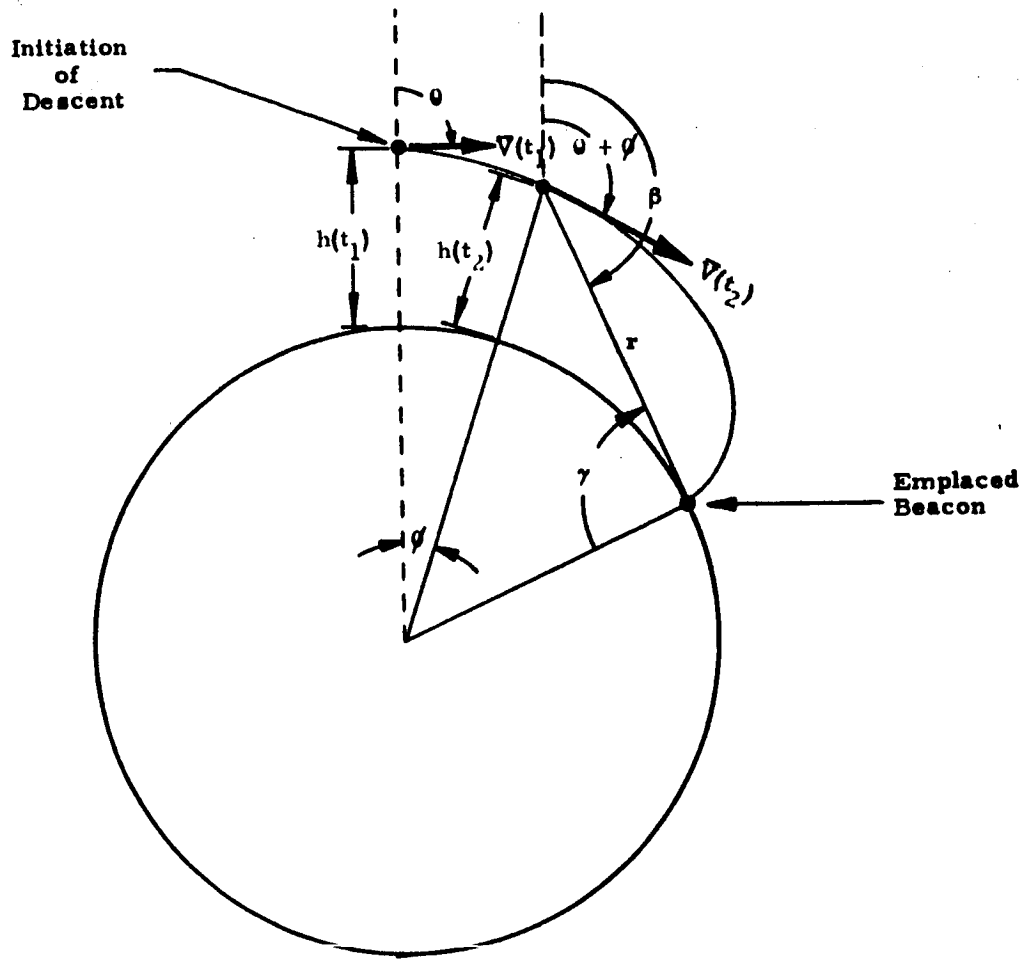

Figure 3-2 Lunar Descent Geometry

The slant range and range rate are plotted in Figure 3-3 versus time from initiation of direct descent from lunar orbit. The look angles from the radar and beacon, β and γ, respectively, are plotted in Figure 3-4. It is to be noted that β is referenced to the surface normal at the point of the descent kick. Knowledge of the vehicle attitude versus time would be necessary to convert β to a look angle referenced to vehicle coordinates. However, $\Delta\beta$ gives a reasonable estimate of the gimbal freedom requirement if large spacecraft attitude changes do not occur.

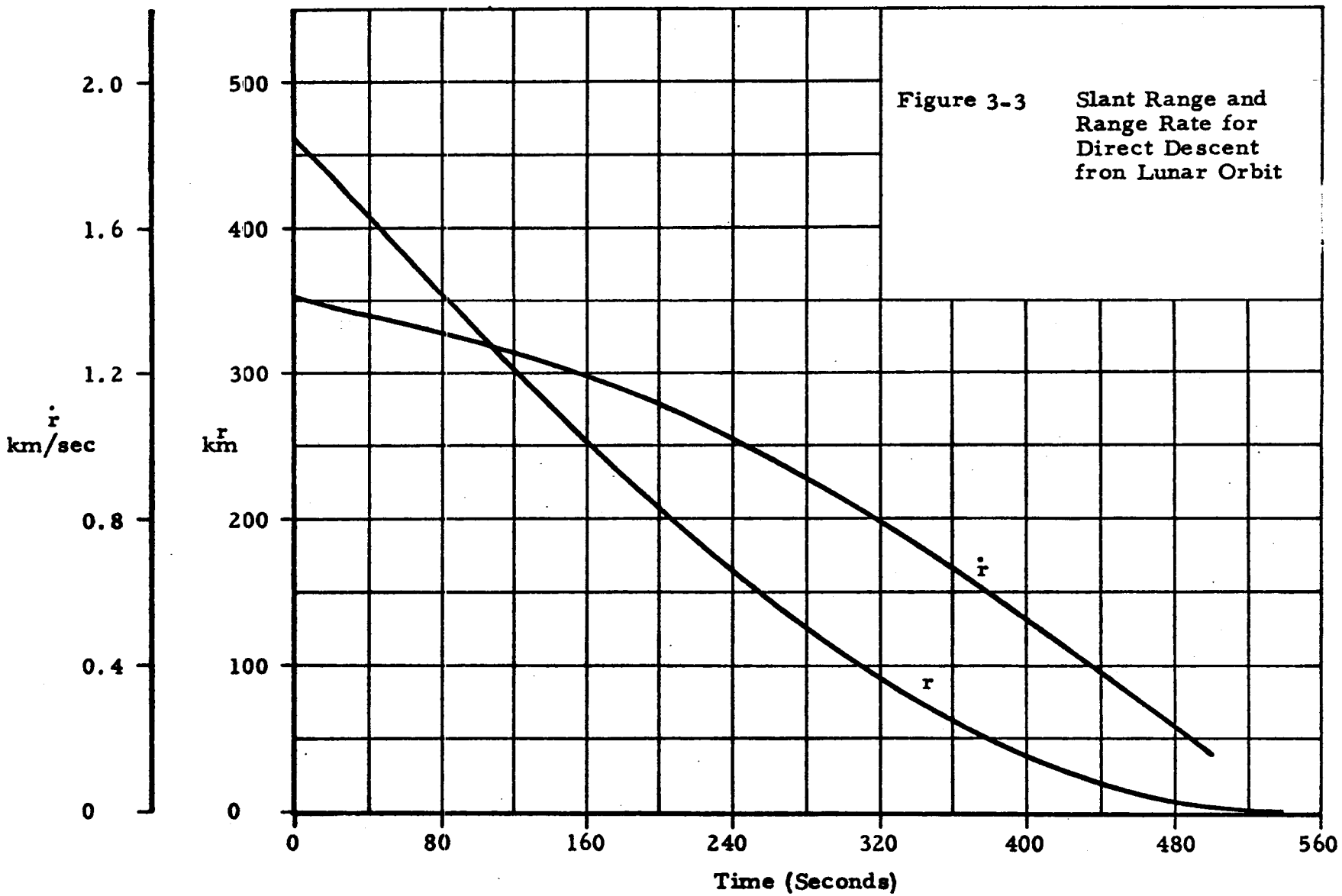

Figure 3-3 Slant Range and Range Rate for Direct Descent fron Lunar Orbit

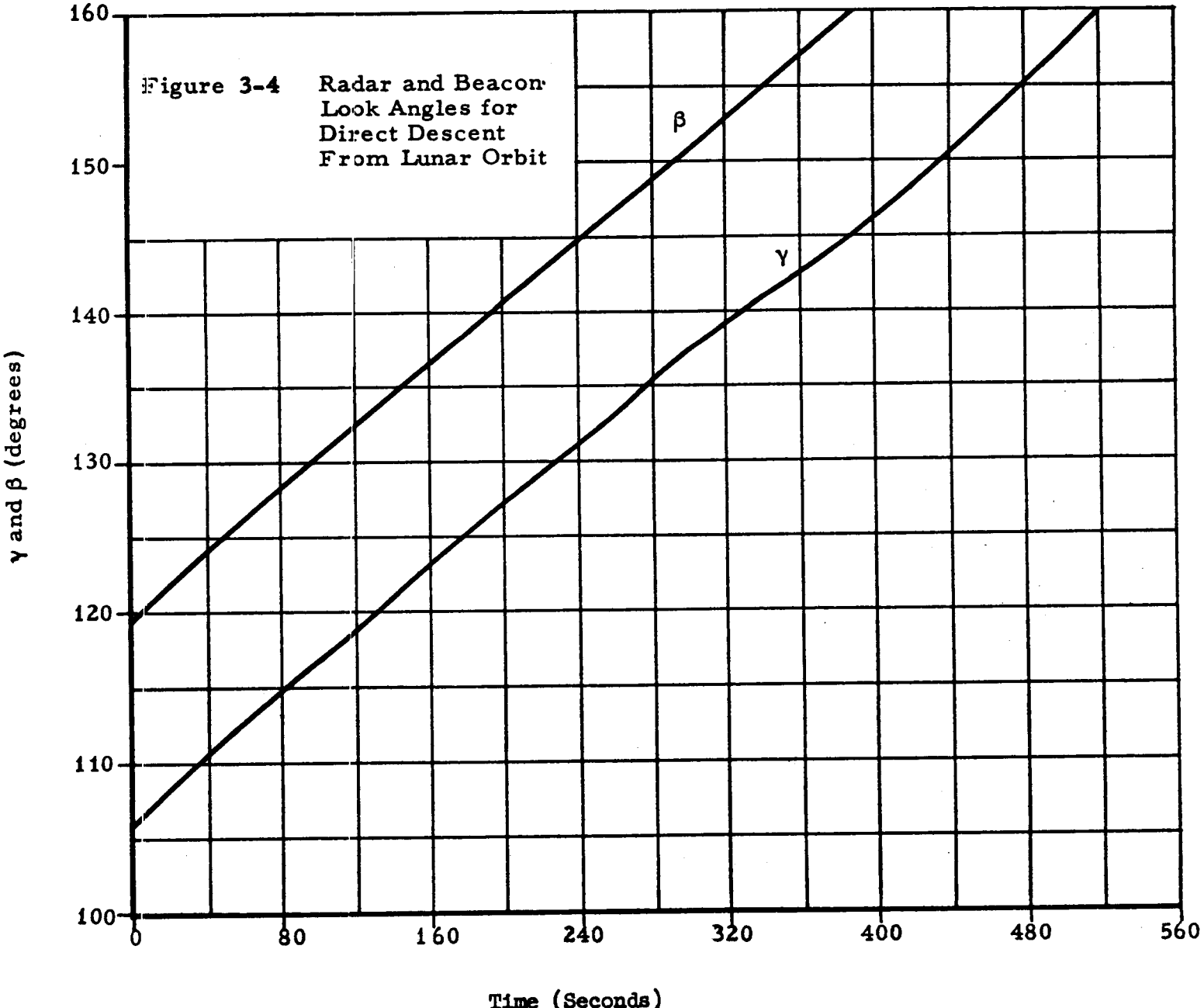

Figure 3-4 Radar and Beacon Look Angles for Direct Descent From Lunar Orbit

From the curves in Figures 3-3 and 3-4, estimates for the following ranges of parameters can be made:

Range	500 km (maximum)
Range Rate	1.5 km/sec (maximum)
Range Acceleration*	7.5 m/sec^2
Inertial Radar Look Angle**	~110 degrees
Radar Inertial Angular Rate	1°/sec**
Transponder Look Angle**	~75 degrees

A descent trajectory for a Hohmann transfer to a periselenum of 25 km and a subsequent powered descent to the surface was examined as to its effect upon lunar landing sensors. It should be pointed out that this trajectory was run purely on a performance basis and constitutes one extremum of a family of possible descent profiles. It would be supplemented by another profile for the terminal descent. Figure 3-5 depicts r and $\dot{r}$ versus time from initiation of the final descent kick. Figure 3-6 shows the previously defined angles β and γ versus time.

In comparing the two flight profiles, it is observed that a range capability of 500 km, range rate of 1.8 km/sec, and angular coverage of 110 degrees at the radar would be adequate. The angular rates and accelerations are within the envelopes previously defined for the powered descent from a 185 km circular lunar orbit. However, the elevation angle of the descending spacecraft, as viewed from the beacon, does not exceed 9 degrees and is as small as 1 degree shortly after descent where maximum antenna gain is required. Multipath would seriously impair the utility of the beacon tracker for this mission profile. Small terrain slopes (as small as 3 degrees) or nearby reflecting objects would completely prevent proper beacon operation during early portions of the flight.

*Greatest near touchdown.
**Depends on relation of landing site to beacon.

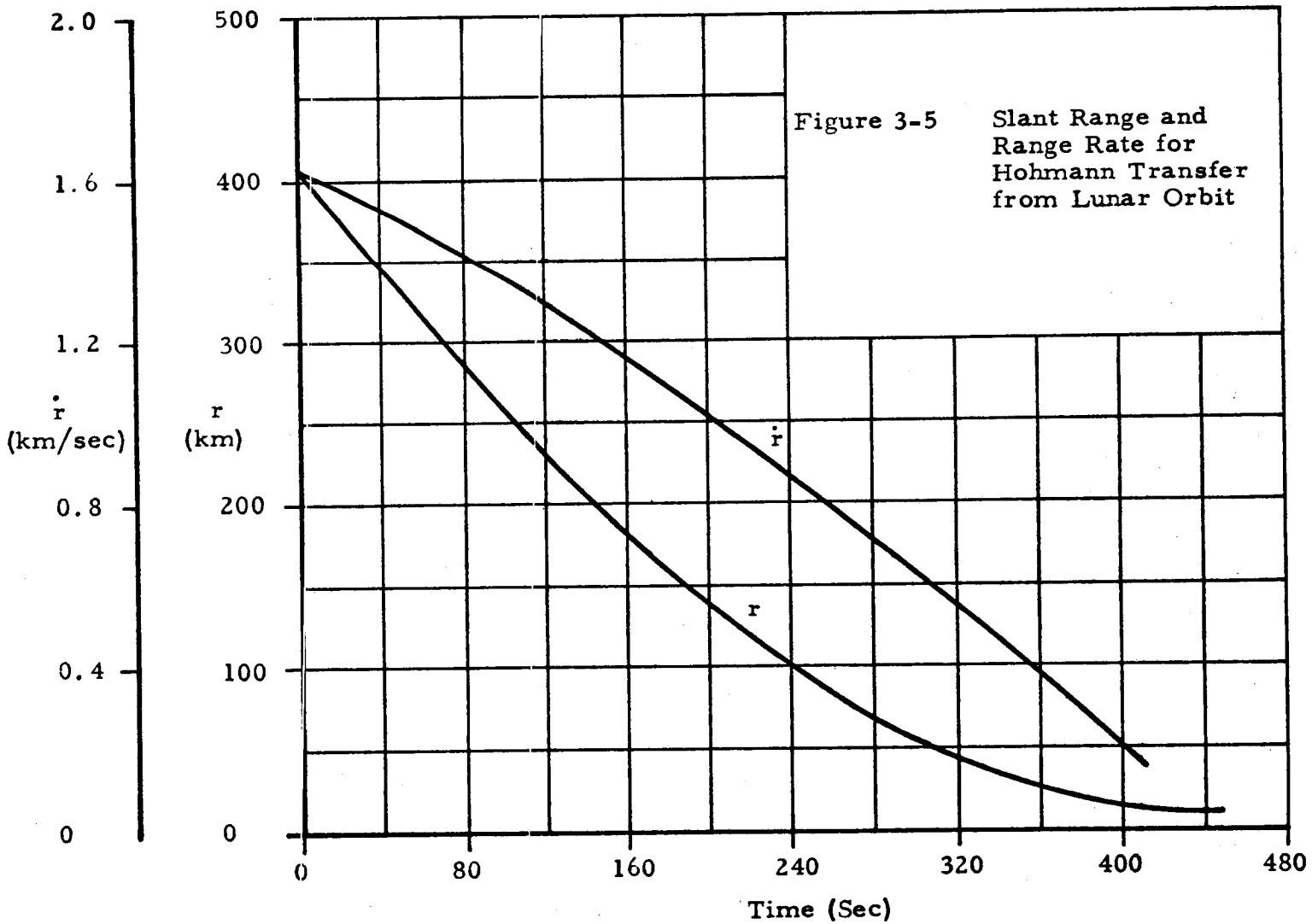

Figure 3-5 Slant Range and Range Rate for Hohmann Transfer from Lunar Orbit

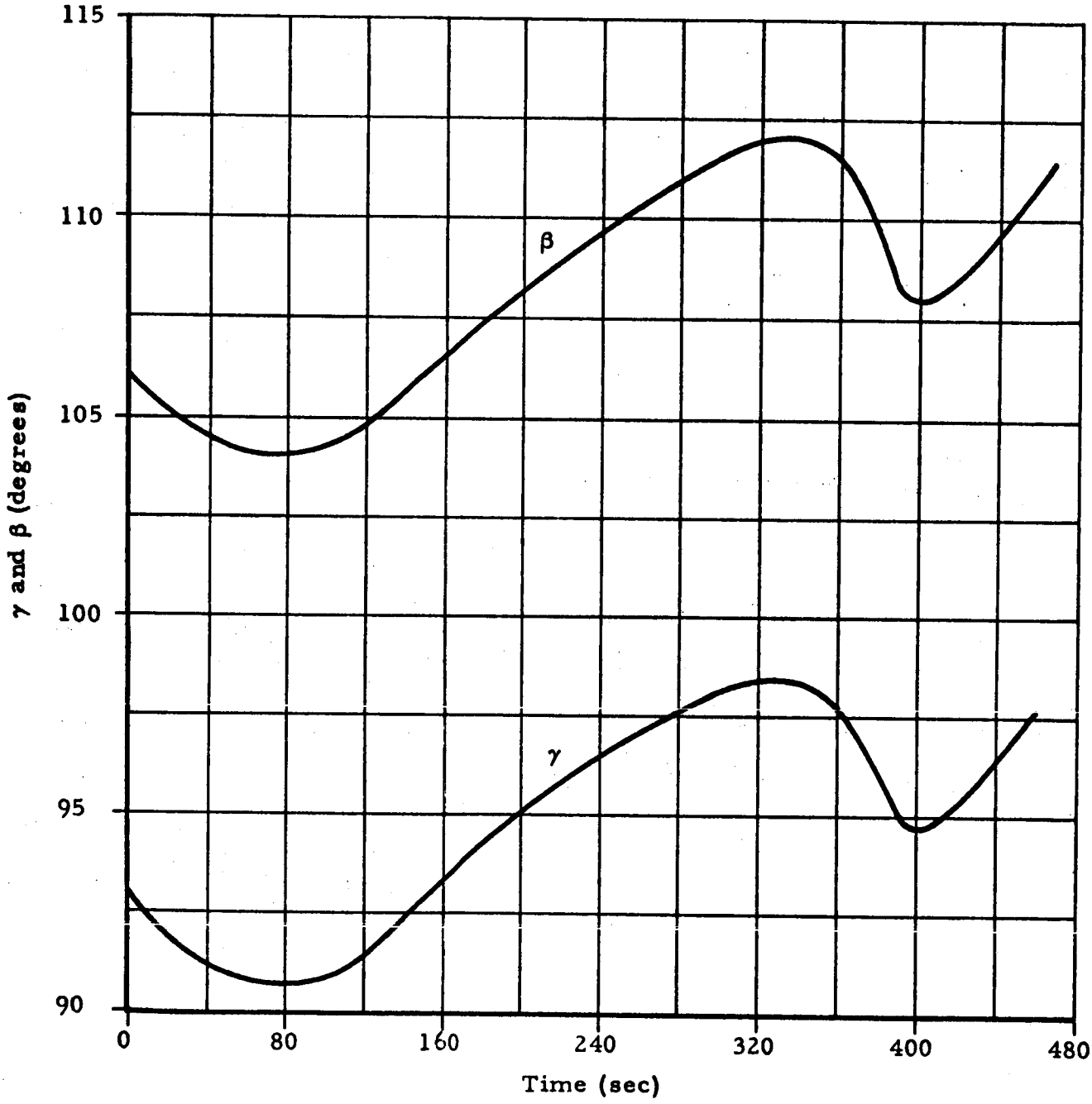

Figure 3-6 Radar and Beacon Look Angles for Hohmann Transfer from Lunar Orbit

3.4.2.2 Nonbeacon-Assisted Descent

The altitude, altitude rate, and angle between the local vertical and the vehicle velocity vector are presented in Figure 3-7 for a direct powered descent from a 185 km circular lunar orbit, and in Figure 3-8 for a Hohmann transfer. Comparing these parameter values with those presented in 3.3.2 indicated no change is required if the altimeter is configured to operate at descent rates up to 550 m/sec in lieu of 300 m/sec.

The velocity sensor should operate at longitudinal rates up to 250 m/sec if operation commences at a range of 10 km from the landing site. The requirements for this sensor are quite similar to those for the spacecraft of Reference 1 which was used as a model for orbital descents during most of the study period.

The sensor characteristics are tabulated in tables in the Summary. The guiding philosophy used was to select parameters so as to minimize the number of different sensors. This approach resulted in an overdesign configuration for particular mission profiles but would enhance versatility and logistics support.

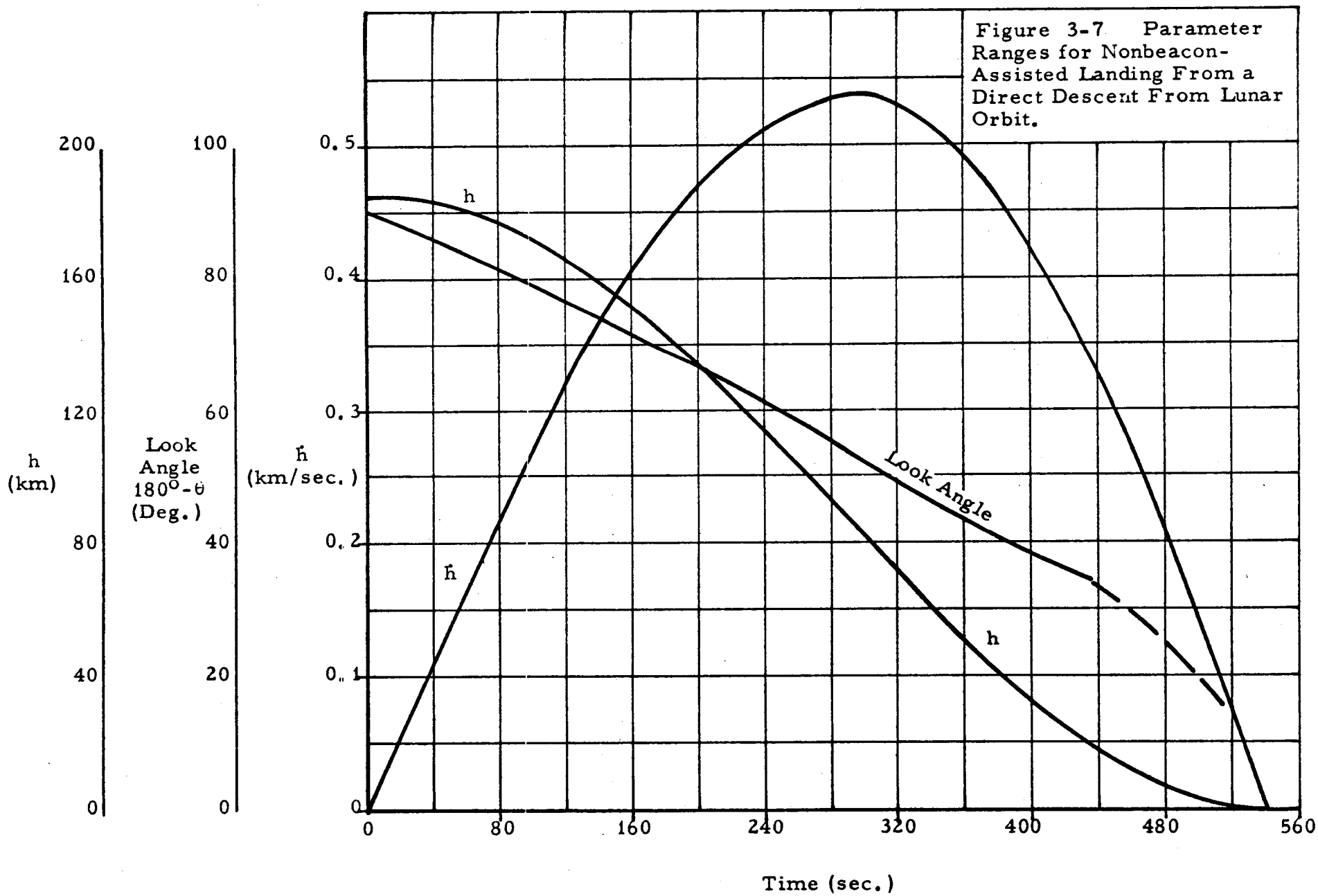

Figure 3-7 Parameter Ranges for Nonbeacon-Assisted Landing From a Direct Descent From Lunar Orbit.

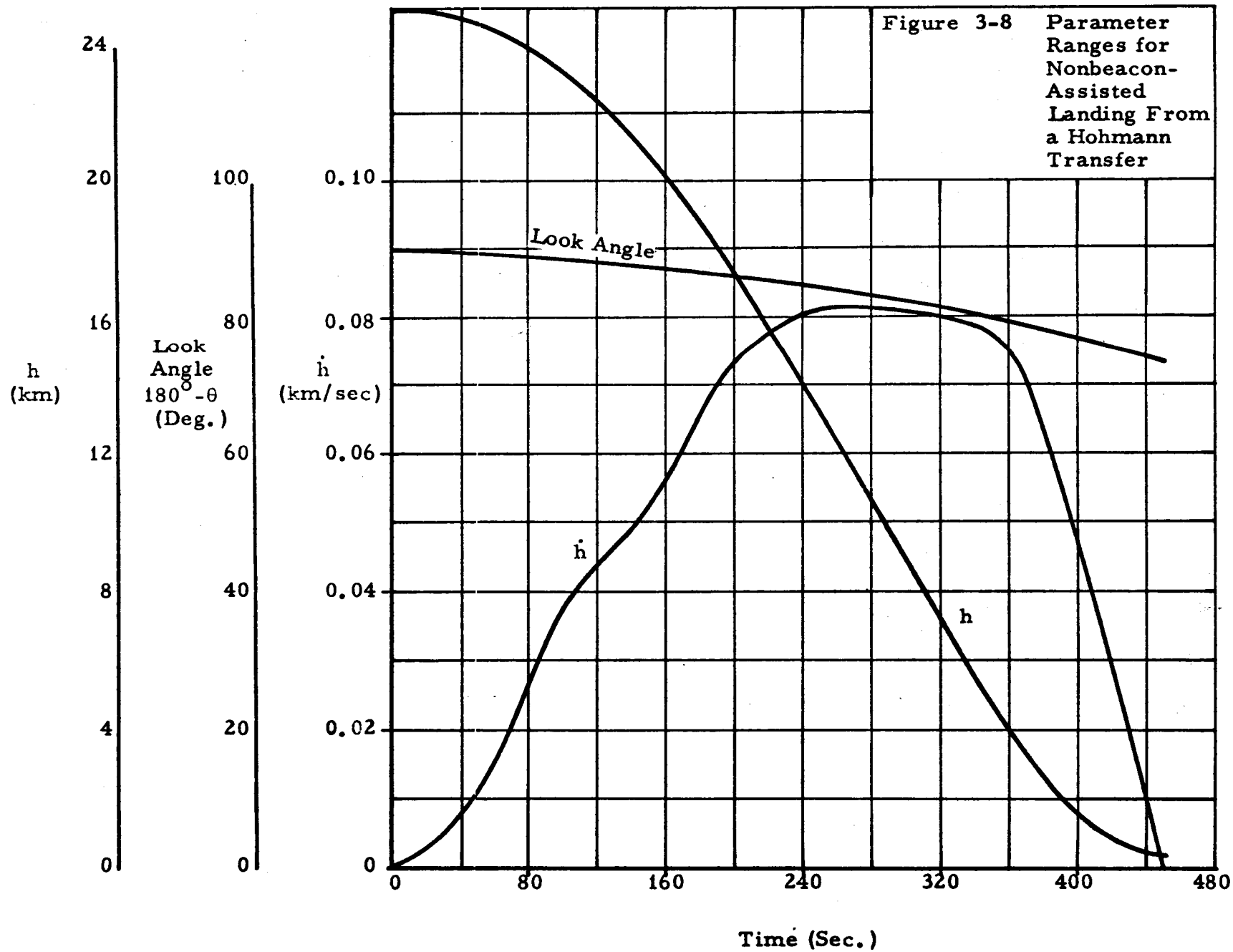

Figure 3-8 Parameter Ranges for Nonbeacon-Assisted Landing From a Hohmann Transfer

4. SYSTEM DESCRIPTION AND ANALYSIS

The discussion of lunar landing sensors, fulfilling the specifications of Section 3, is categorized according to function, for reasons of clarity, in this section of the report. The beacon tracker will be integral with the high altitude altimeter, as depicted in the Summary, Section 2.

A beacon tracker, with an antenna possessing the requisite LOS visibility and with appropriate beacon antenna coverage, can satisfy all the guidance sensor requirements for a soft lunar landing near an emplaced beacon. If large beacon offsets are employed, an altimeter for terrain avoidance assurance and a doppler velocity meter to prevent beacon tracker angular rate errors from generating excessive lateral rates and displacements are indicated. The STELATRAC beacon tracking radar is described in Section 4.1 and can fulfill all beacon tracker requirements.*

4.1 BEACON-ASSISTED DESCENT

STELATRAC is an all solid-state coherent CW beacon tracking radar system. It performs the functions of detection, angle sensing, angle and angle rate measurement, precision ranging, and range rate determination. The angle sensing antenna and radar transceiver are located on the incoming spacecraft, while the beacon is on the lunar surface. Both the radar transceiver and cooperative beacon contain phase tracking receivers; in addition, the radar transceiver contains the electronics required for angle error detection and range determination.

4.1.1 Selection of Operational Frequency

STELATRAC was originally designed to operate at frequencies near 10 gc (X-band) because of the need for accurate angle date from a limited-extent aperture and a desire for precise range rate information. The angular accuracy requirements of 0.3 degrees established in Section 3 would permit a

*A more detailed description of STELATRAC is presented in Interim Report No. 1, "CW X-Band Radar Development", 1 June 1961, and STELATRAC Project Report No. 2, 30 June 1962.

received frequency as low as 4.0 to 6.0 gc at the radar for a 0.6 m aperture. The frequency of the link from the radar to the beacon cannot be determined in an analogous manner, as it does not directly affect the angle performance at the radar for a properly designed dual frequency antenna. Doppler sensitivity requirements would also permit a lower frequency to be selected. However, the use of the radar during main braking suggests 6.0 to 10.0 gc as the frequency region that can safely be employed to preclude deleterious flame effects due to exhaust products at thrust levels in excess of 30,000 pounds. (Flame effects are discussed more fully in Section 4.1.10.)

However, if it were not required to provide sensor data during periods of high thrust, such as at main braking, and if favorable siting of the beacon antenna could be assured to avoid multipath signals, appreciable simplification of the transponder can be realized if the radar-to-transponder link is at a frequency below X-band, possibly as low as 300 mc. The reduction in components accures as the transponder receiver uses 1) an r-f amplifier (no X-band L.O. or microwave mixer required), 2) a low frequency injected reference (at the first i-f and directly derivable from an oscillator without subsequent high factor multiplication), 3) carrier acquisition circuitry can be significantly reduced or eliminated as the doppler and oscillator frequency uncertainty is negligible, and 4) receiver sensitivity is enhanced by the lower operational frequency. Conversely, the radar transmitter output may be in the watt regime at no increase in input primary power due to the lower operational frequency. The loss in radar transmit antenna gain is overcome by the increase in radar transmitted power, lower transponder noise figure, and narrower-bandwidth receiver tracking loops. As the transponder antenna gain is in the realm of +11 to +14 db, corresponding to an area of approximately λ^2 to $2\lambda^2$, it is feasible in some applications to increase the beacon antenna aperture as the frequency decreases to maintain a constant or only slightly reduced transmit antenna gain-receive aperture area product. (For this case, the range of operation can be extended or the transmitter output power decreased.)

In addition, multipath at the beacon site may become prohibitive if a low frequency is selected without maintaining sufficient directivity of the beacon antenna. Since two apertures are indicated to provide the requisite

coverage during direct and orbital descents, maintaining constant beacon antenna gain with decreasing frequency causes a significant sensor weight penalty.

In conclusion, operation at X-band is recommended and, as will be shown in Section 4.2, will reduce altitude terrain bias errors for the modulation envelope employed in the extended range altimeter which is to be integral with STELATRAC. The beacon transponder is discussed first, as it is conceptually simpler since no data readout circuitry is required.

4.1.2 Beacon Transponder

The beacon consists of a coherent transponder and a relatively small circularly polarized antenna. Figure 4-1 shows a functional block diagram of the transceiver, and Figure 4-2 is a photograph of a flight packaged STELATRAC transponder. Basically, the receiver is a phase tracking, double conversion superheterodyne, though unique because the reference (or second L.O. signal) for the second detector is additively combined with the received signal at r-f ahead of the first mixer, and then translated along with the signal to i-f.

The r-f injected reference is phase controlled to maintain a fixed frequency offset equal to the second i-f. Injected reference tracking is applied to a ranging sideband as well as to the carrier. At the beacon, both the transmitted signal and injected reference are modulated with the receiver processed ranging modulation signal. The carrier and a single sideband, with their accompanying injected reference counterparts, are separated at i-f. Receiver processing in two identical parallel channels follows, with the carrier channel output controlling a carrier VCO and the sideband channel output controlling the modulation signal frequency and phase. The controlled VCO signal is translated to three frequencies via parametric frequency multiplication. One of the signals is the r-f injected reference, one is the local oscillator for the first mixer after it is suitably sidestepped, and one (at power level of 100 mw) is transmitted. The ranging signal is impressed on the transmitted carrier by phase modulating the carrier signal as it is being processed by the varactor multiplier chain.

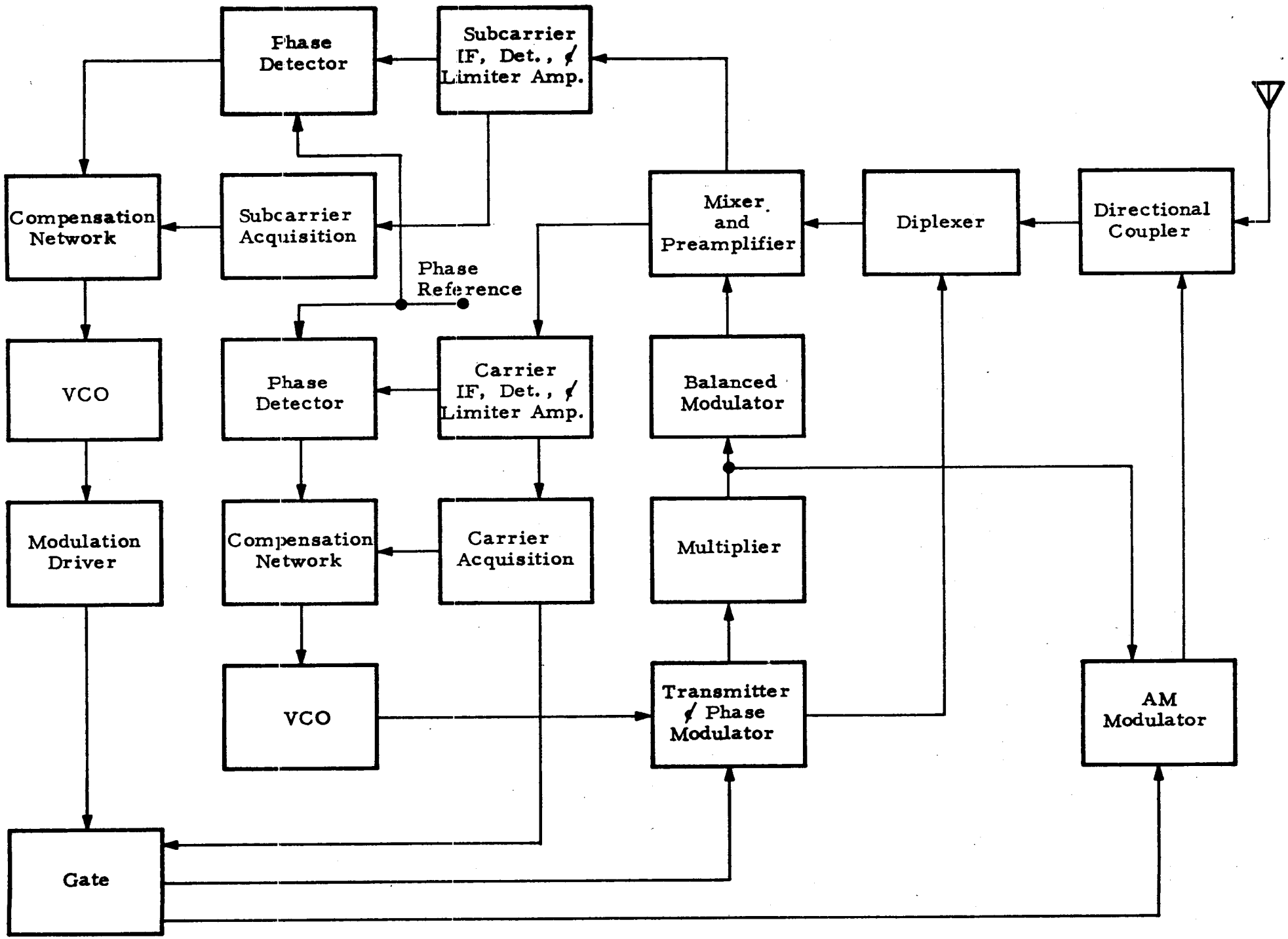

Figure 4-1 Functional Block Diagram of Beacon Transceiver

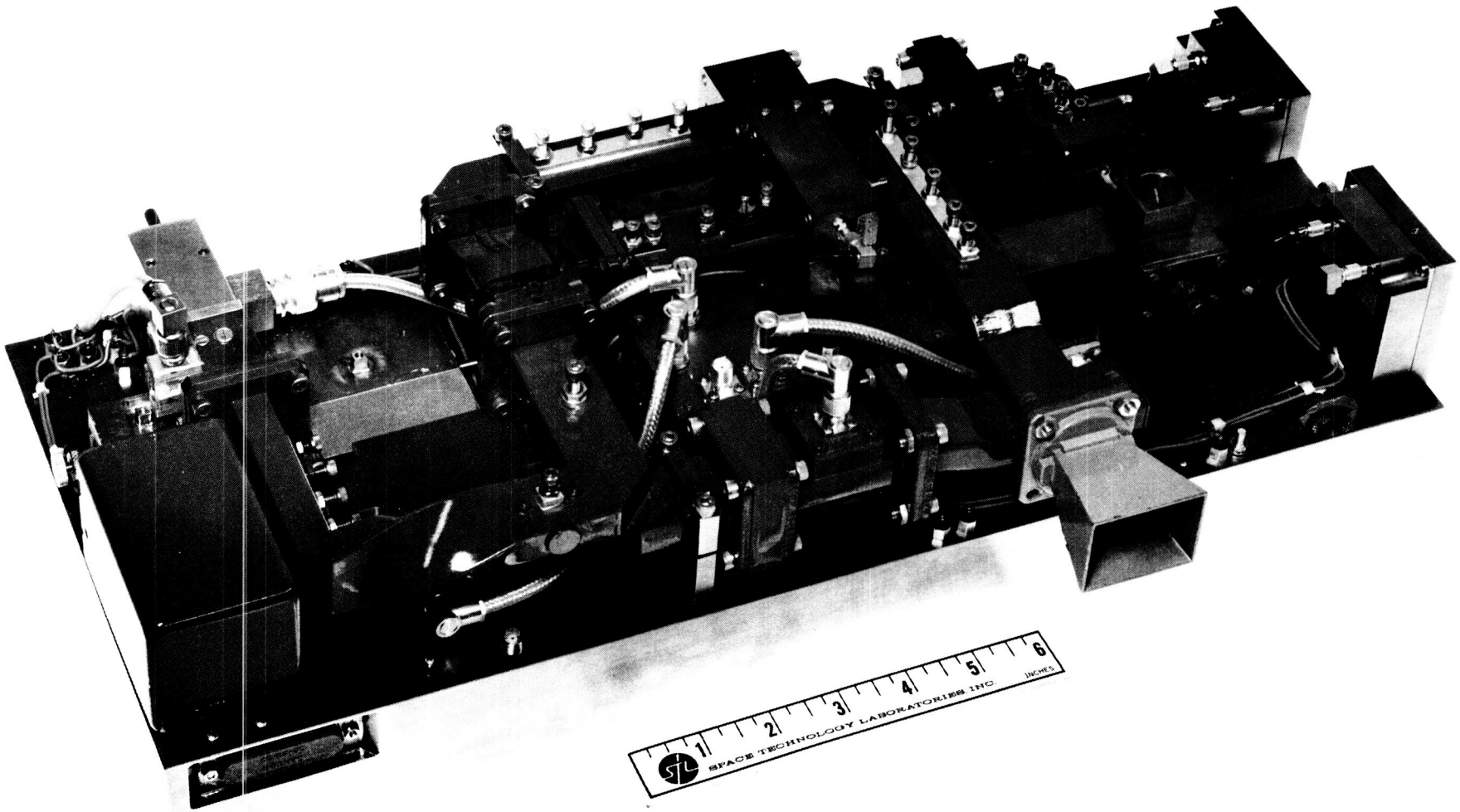

Figure 4-2 Flight Packaged STELATRAC Transponder

The injected reference technique is a means for stabilizing the receiver time delay, that is, circumventing the usual receiver delay variations due to temperature, component aging, and signal strength fluctuations. The modulation phase (ϕ_m) is carried through r-f and i-f sections of the receivers as the difference between differential phases of a carrier-injected reference signal pair and a sideband-injected reference pair. The carrier and a single sideband in the signal received at the antenna, which have phases

$$(\omega_c t + \theta) \text{ and } \left[(\omega_c + \omega_m) t + (\theta + \phi)\right] \tag{1}$$

respectively, are added linearly to a similar pair in a directional coupler. This similar pair constitutes the carrier and sideband injected references shifted in phase from their counterparts at the antenna terminal by

$$(\omega_r t + \phi_r) \text{ and } (\omega_r t + \phi_r + \phi_m) \tag{2}$$

respectively, where ω_r is an audio-frequency offset established by a reference oscillator and ϕ_m represents the difference between transmitted and received modulation phase. The carrier and its injected reference (as well as the sideband and its injected reference) incur nearly identical phase shifts in the receiver, since ω_r is small relative to the i-f bandwidth. Furthermore, the information of interest is

$$\phi_m = \left\{\left[(\omega_c + \omega_m) t + (\theta + \phi)\right] - \left[(\omega_c + \omega_m - \omega_r) t + (\theta + \phi - \phi_m - \phi_r)\right]\right\} - \left\{(\omega_c t + \theta) - \left[(\omega_c - \omega_r) t + (\theta - \phi_r)\right]\right\} \tag{3}$$

Letting $\Delta\theta_1$ and $\Delta\phi_1$ be the receiver induced phase errors on the carrier and its injected reference and $\Delta\theta_2$ and $\Delta\phi_2$ the corresponding sideband-injected reference pair phase errors, the error in ϕ_m will be

$$\epsilon_{\phi_m} = (\Delta\theta_2 - \Delta\phi_2) - (\Delta\theta_1 - \Delta\phi_1) \tag{4}$$

By choosing ω_r small compared to the i-f bandwidths and by approximately matching i-f phase characteristic slopes at carrier and sideband frequencies, receiver phase errors due to i-f phase characteristic variation are virtually eliminated. The modulation phase shift, ϕ_m, is recovered by isolating carrier-injected reference and sideband-injected reference pairs by i-f filtering,

envelope detecting in each channel, and phase comparing at the offset frequency, ω_r, which is the second intermediate frequency. Amplification and filtering of these signals is required before phase comparison. The amplification is provided in limiter-amplifiers and the filtering takes place in relatively phase stable audio frequency filters.

An important ancillary feature of the injected reference technique is that the receiver through the second detector behaves as a wide dynamic range linear receiver, although none of its components is subjected to a wide dynamic range signal. The requirement for linearity is that the injected reference signal level be fixed and significantly greater than that of the received signal. Thus, the signal level in the receiver is set by the injected reference and is essentially constant.

The beacon antenna must be designed 1) compatible with the two mission descent profiles, 2) to maximize antenna gain thereby minimizing primary power consumption, and 3) to discriminate against lunar multipath. The restriction of primary power indicates a beacon antenna radiating shaped beams that provide sufficient power density at the terminal phase and reduce the errors introduced by multipath propagation by angular discrimination. Needless to say, a beacon antenna with restricted radiation lobes must be placed accurately in an upright position with the correct azimuthal orientation.

For orbital tracking, two beams (nominal half-power beamwidth of 20 degrees) diametrically opposed* in the orbital plane and at nominal elevation angles of 20 degrees are indicated. The beams will be shaped so that there will be +13 db of gain at 10 degrees elevation angle and the gain in power density resulting from the decrease in range along the nominal braking trajectory will more than accommodate the loss in antenna gain as the elevation angle increases during the terminal portion of the descent. Orbital plane uncertainties for the landing spacecraft and rotation of the moon determine the antenna coverage in the plane normal to the orbit. For typical mission profiles, 15 degrees is adequate, but coverage for 30 degrees is recommended.

*Two beams oriented in this manner will permit descents from either direction.

The beams will be shaped in this plane to provide sufficient antenna coverage for landing trajectories which are out of plane as much as 30 km. In this case, contact would be maintained until the vehicle reached an angle of at least 45 degrees from the beacon site for typical descent trajectories. At that time, the antenna could be switched to the aperture normally used for a direct approach if further tracking is required.

For the direct approach, a broader beamwidth can be provided as multipath is not as serious due to the large elevation angles. Conical half-power beamwidths of 50 degrees can be considered and will provide ample gain, i.e., approximately +11 db.

Switching between the two antennas is recommended to reduce the possibility of interference nulls at elevation angles between 30 and 60 degrees. (Solid-state switching would be used.) However, both apertures could be excited simultaneously and still provide a net antenna gain of +8 db minimum in each beam.

4.1.3 Beacon Tracking Radar Transceiver

The receiver and transmitter portions of the beacon tracking radar are similar to the beacon transceiver, except that the transmitter and receiver frequencies are interchanged, the transmitter is independent of the carrier tracking receiver, and the ranging signal phase is measured but not tracked. Also, circuitry has been added for processing the angle signals to derive angle tracking errors. A block diagram of the receiver and transmitter portions is shown in Figure 4-3. This assembly would also contain the electronics required to process the raw receiver data, that is, range and range rate information.

The comparison of transmitted and received modulation phase is effected by modulating both transmitter and carrier injected reference with a common modulation reference as in the transponder. The range information, or phase shift of the modulation around the radar-transponder-radar path, is extracted by comparison of the two radar receiver channel outputs. Range rate information is extracted at the radar by means of X-band transmitter-injected reference frequency differencing. This is effected by a crystal inserted into the normally terminated arm of the directional coupler used to inject the

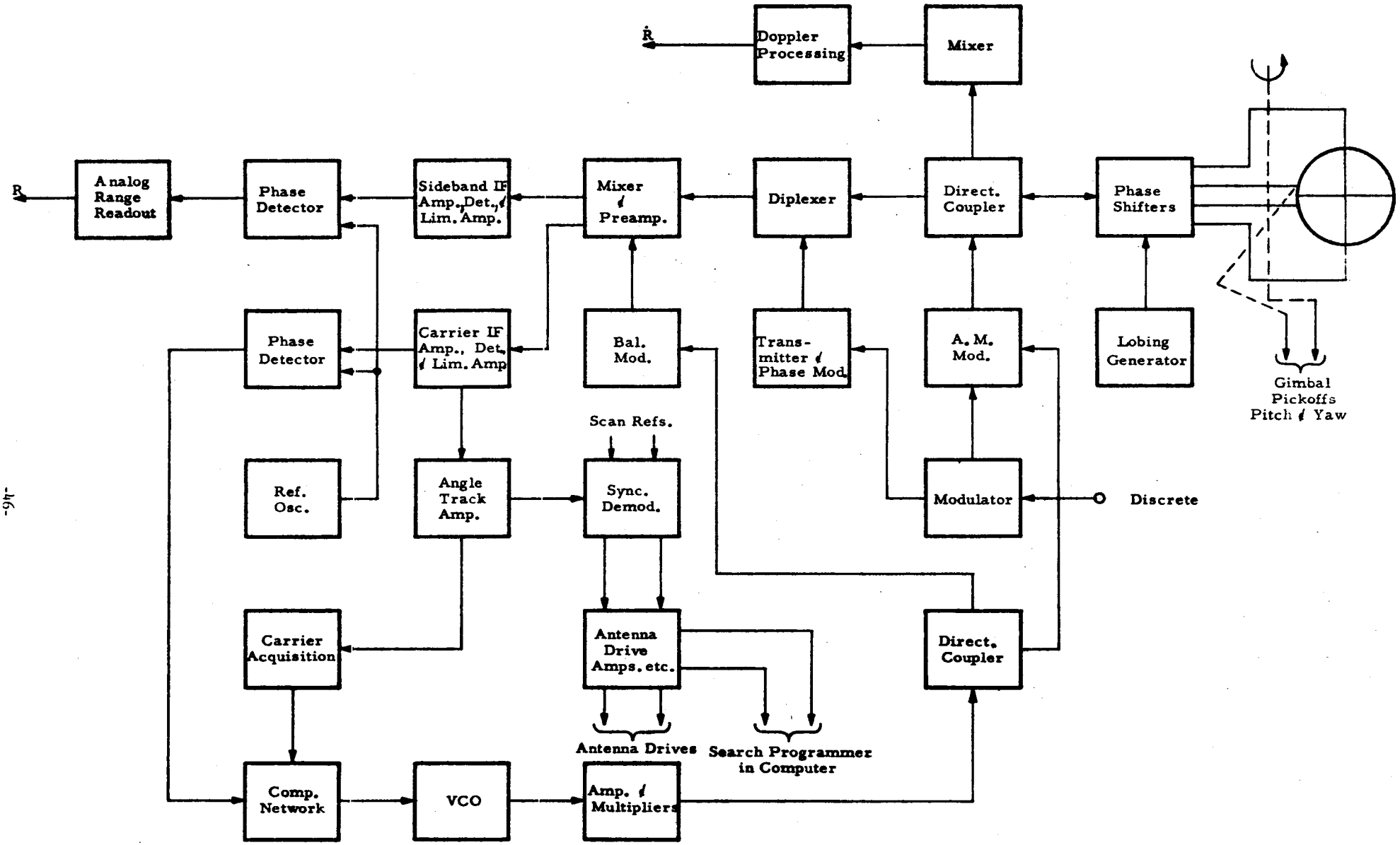

Figure 4-3 Functional Block Diagram of Radar Transceiver

reference signal into the receivers. The difference signal derived is further heterodyned with a low level signal bled from the transmitter chain to yield the doppler shift on an appropriate bias frequency (which may be changed as desired by changing injected reference offset frequencies).

Pitch and yaw information resides in the amplitude modulation on the received signal. It is processed by synchronously demodulating the amplitude-detected second i-f signal which is then fed to the antenna assembly for control purposes. The reference signal employed for demodulation is the same signal employed in the solid-state lober to impose the angle modulation. To obviate the need for r-f rotary joints, the received signals may be brought to the transceiver assembly at i-f via a cable wrap assembly, as less than 180-degree angle freedom is required.

4.1.4 Radar Antenna

4.1.4.1 Design Consideration

The radar antenna configuration selected depends upon the preferred angle sensing technique, angular coverage requirements during any one mission and from mission to mission, operational frequency, spacecraft attitude control philosophy, limitations of available spacecraft antenna locations, reliability potential, and impact upon sensor circuit complexity. The particulars of these characteristics as they pertain to the radar antenna are discussed in the succeeding paragraphs.

For cooperative applications, scintillation of the received signal is negligible except for lunar multipath and flame effects during periods of thrust. Since the operational frequency is in the microwave region where sufficient antenna directivity can be realized with practical aperture sizes, both of these possibilities can be made remote. With the specified ± 0.3 degree angular accuracy requirement and a 0.6 m antenna aperture, conical as well as simultaneous and interferometric lobing can be considered. The first minimizes the angle processing circuitry and can be all solid-state with the advent of ferromagnetic and semiconductor phase shifters for imposing conical lobing. The third technique can perform angle measurements off-boresight and hence may

not need to be gimbaled if angular coverage is restricted, whereas the others are null trackers.

There are significant differences in the antenna gain characteristics of each lobing method which must be evaluated before the angle sensing technique is chosen. With the interferometer, a wide field-of-view conflicts with the requirement for antenna gain. If the field-of-view is to be 20 degrees measured between the half-power points of the radiation pattern, the elemental antenna maximum gain is restricted to about 18.0 db, whereas 33.0 db can be achieved with a 0.6 m diameter aperture. The 15.0 db lower value of antenna gain necessitates higher transmitter power, an uneconomical tradeoff for solid-state operation at X-band.

Lastly, angle ambiguity resolving provisions are necessary for the interferometer. For example, for interferometer baselines of 10 wavelengths, the first ambiguity null occurs at $\pm$2.9 degrees and subsequent nulls at $\pm$8.6, $\pm$14.5, $\pm$20.5 degrees, etc. The resolving technique must be capable of operating over the anticipated range of angular ambiguities. Several antenna possibilities can be conceived which fulfill these requirements. For example, a sequential lober can perform the acquisition and track functions at large distances where it may be feasible to steer the vehicle to track on null. At shorter separations where signal levels are high, small elemental antennas disposed about the lober in an interferometric array can sense angle and the lober will be capable of resolving ambiguities. (Figure 4-4 is an illustration of this concept.)

The angular coverage specification in the pitch axis is 110 degrees and a form of gimbaling is indicated, assuming it is not practical to steer the spacecraft. Both discrete or continuous motion may be acceptable, depending upon the lobing technique employed. Electronic beam positioning and tracking over such an angular volume is not believed commensurate with spaceborne applications during the 1966 time era because of equipment complexity.

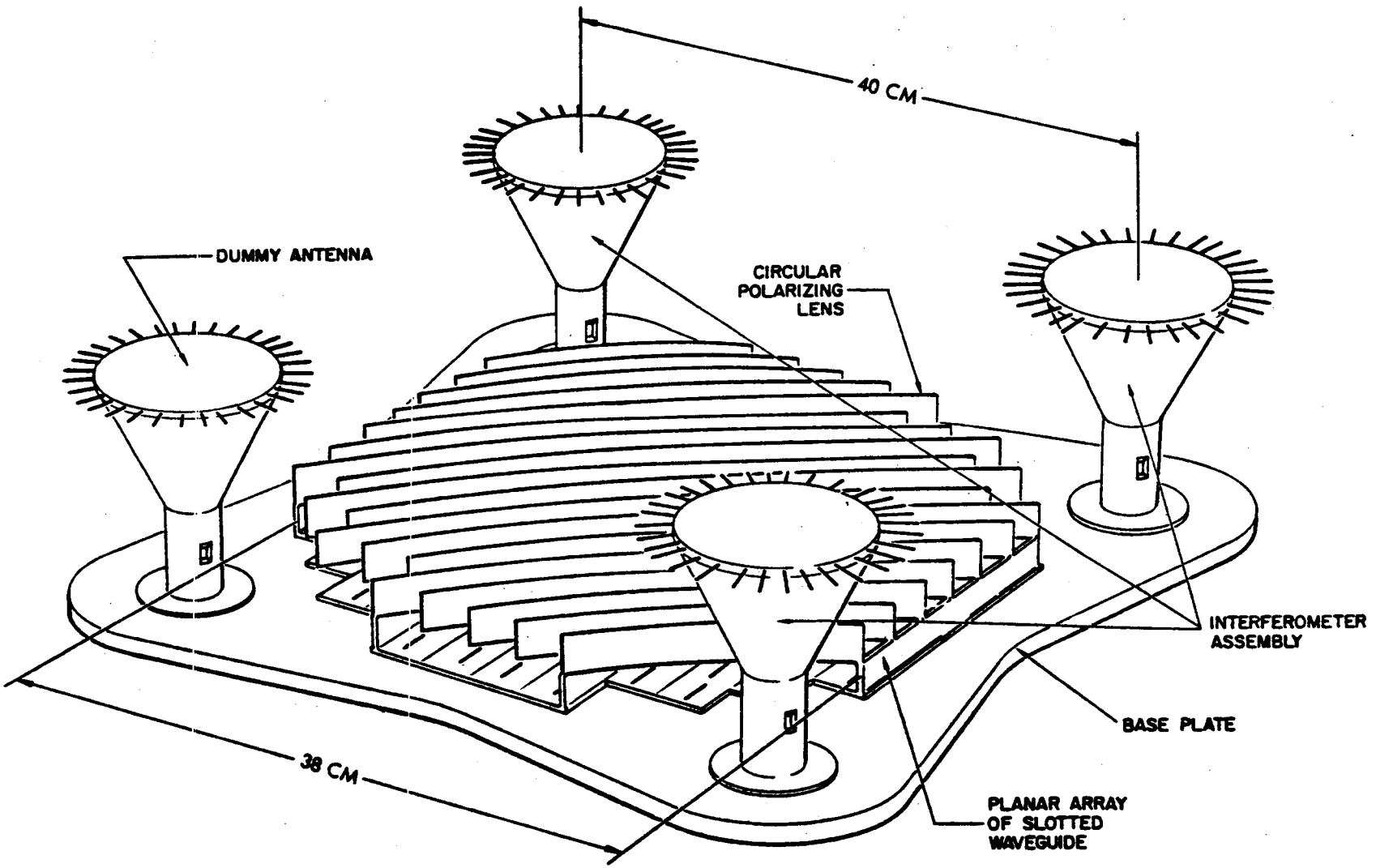

Figure 4-4 Radar Package Showing Interferometer Antenna Assembly and Conically Scanned Planar Array

Planar arrays operating in the microwave spectrum are preferred because they are efficient, can be designed for low sidelobes, are adaptable to simultaneous and sequential lobing methods, and are lightweight.

The guidance philosophy can have a direct impact upon the radar antenna design. For example, during some mission phases, fixed antennas are appropriate as the spacecraft attitude is controlled to maintain LOS visibility during nonthrusting periods. While in lunar orbit or during traversal of the descent ellipse, it would be feasible to orient the spacecraft to position the antenna beam. Similar conditions exist during portions of the direct approach trajectory. Secondly, the guidance law to be followed may dictate appreciable maneuvering of the spacecraft during thrust periods, necessitating extended angular coverage if sensor data is simultaneously required. During the terminal braking phase, appreciable coverage in the pitch plane is mandatory, especially for landing sites requiring beacon fly-over (coverage in the yaw plane may be minimal at this time). Lastly, stabilization and control malfunctions are in-line failures of the beacon tracker if vehicle positioning of the radiation beam is employed.

The antenna locations available on the spacecraft interface with the antenna design. If spacecraft multipath can be large, narrowbeam antennas afford discrimination, whereas fixed widebeam antennas do not. Conversely, more flexibility exists with respect to available sites for fixed antennas due to their lighter weight.

The reliability of the selected antenna configuration is especially significant in establishing overall sensor reliability. Due to its importance, a quantitative reliability discussion is presented in Section 8. Many studies have been conducted pertaining to positioning and drive mechanisms with extended lifetimes in a space environment. The OGO solar array drive assembly and the Mariner communication and radiometer antennas are examples of such technology. Some of the design facets of the latter are outlined below.

The Mariner II radiometer antenna was scanned in one dimension prior to and during Venus fly-by. The antenna was scanned ± 60 degrees at a rate of 1°/second until the thermal outline of Venus was intercepted. After thermal contact was made, the scan speed was reduced to 0.1°/second. (If Venus disappeared from the field-of-view, the speed would be stepped back up to 1°/second until reacquisition was completed.) In addition to the radiometer antenna drive, similar drives were used for the high gain command antenna. The latter drives operated continuously, that is, moved a small increment each day while the radiometer antenna was not exercised during the transit time from launch to Venus contact--a period of 109 days. The command antenna operated approximately 10 days after Venus fly-by, at which time contact with earth was lost.

Nonactive temperature control was employed on the drive housing. The portion of the drive housing exposed to direct sun impact was painted white. Other sides were polished aluminum for thermal radiation purposes.

A preliminary investigation has been made on a continuously positionable* antenna with a total operating lifetime in a ground environment of 100 hours and 50 hours in space with a nonoperating lifetime in space of 1 year. Each operating cycle was represented by 2 minutes search and 40 minutes tracking.

The antenna was to be gimbaled in the pitch plane for ± 60 degrees coverage and in the yaw plane for ± 30 degess. The short operating lifetime requirements can be satisfied by nearly any of the dynamic components which would be applicable to the antenna drive. Motors, bearings, gears, and seal enclosures have lifetimes appreciably above the values stated. In contrast, the nonoperating lifetime of 1 year in space requires careful selection of materials compatible with the radiation and low ambient pressure environment. Particular attention must be given to choice of lubricants and methods for their retention.

*The design of a discretely positionable antenna would present similar problems and the remarks made here are applicable in essence to it.

In the interest of weight and space economy and reliability enhancement, a minimum number of parts results by driving the antenna directly with a low speed d-c torque motor. A sealed bearing and position pick-off assembly for the pitch actuator is shown in Figure 4-5. The design of Figure 4-5 is not necessarily optimum for all spacecraft, but does provide a means for definitizing the discussion and exploring the problem areas. The general design philosophy applies equally to the yaw gimbal.

A. Drive Motor. Use of low speed motors is desirable wherever possible to keep frictional surface velocities down. D-C torque motors are ideally suited for variable speed operation and possess ample torque capacity for accelerating the inertia load of the antenna gimbals and overcoming the rubbing friction of the dynamic seals. STL has successfully operated d-c torque motors at 2×10^{-7} Torr vacuum for over 2,000,000 revolutions without failure. A similar application of the torque motor was used by the Ball Brothers in the OSO vehicle. Brushes were composed of a silver-graphite-molybdenum material (75%-20%-5%) and coated with a "Bardahl" oil derivative for the STL tests. Avoidance of gearing in the power train is of great significance, in view of the present lack of information on gear performance in space. Test programs to select the best gear materials and associated lubricants are quite time consuming and often inconclusive. The savings in weight plus improved reliability are strong arguments for the torque motor arrangement.

B. Bearings. Mounting all rotating shafts on anti-friction bearings equipped with shields is recommended. Angular contact bearings are indicated in order to maintain the proper alignment, rigidity, and preloading. Based upon available bearing literature and recent STL studies, stainless steel with impregnated phenolic retainer are the logical bearing materials. Bearing material should be 440C for corrosive resistance during handling. The reinforced phenolic retainer should be impregnated with a low vapor pressure and high radiation tolerance oil such as General Electric Versilube F50 oil where hermetic sealing is not feasible, or as in this case, not desirable. For instrument bearings which cannot be impregnated, a silicon grease such as G.E. G-300

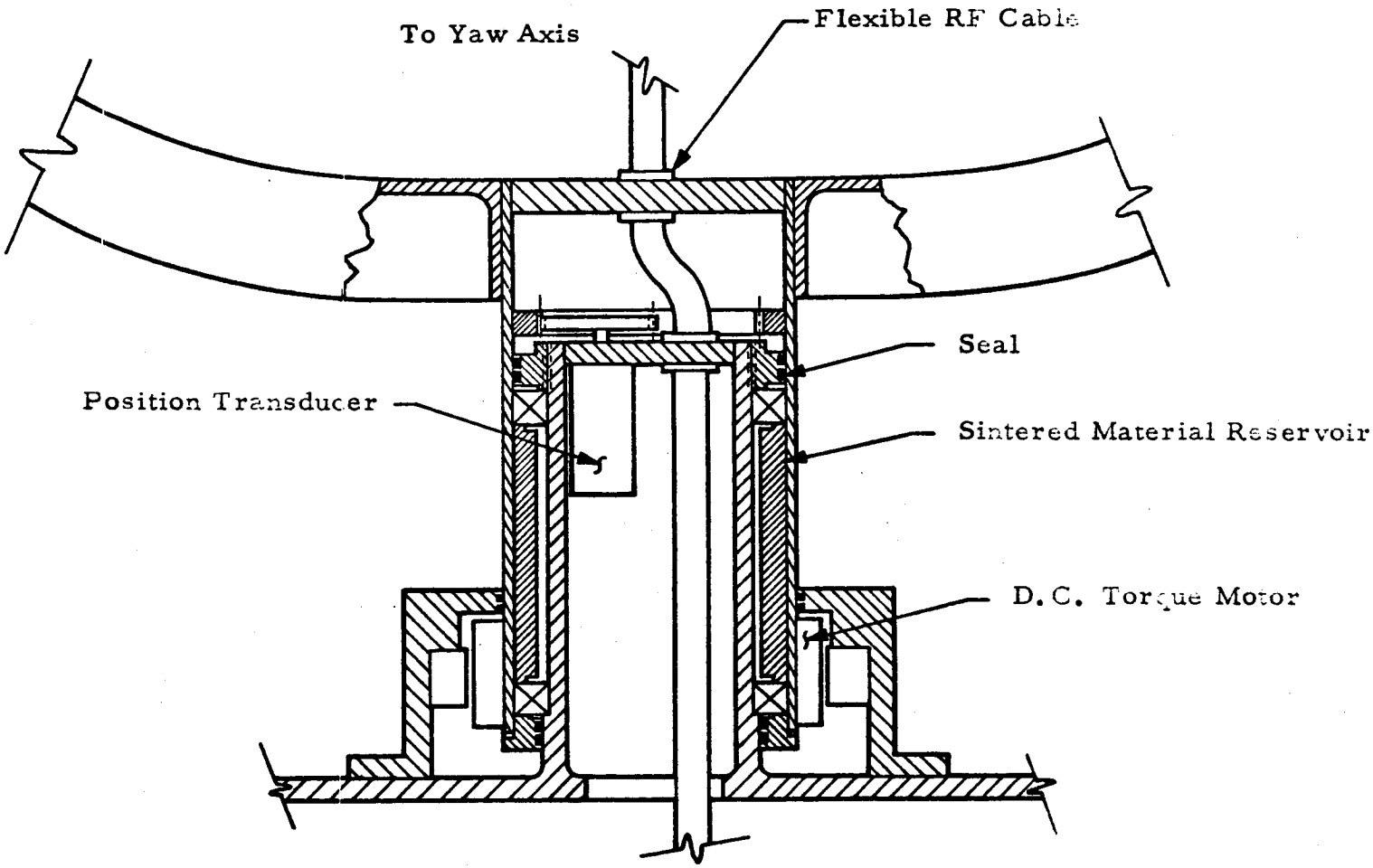

Figure 4-5 Pitch Actuator Arrangement

is recommended. In any event, bearing assemblies should be enclosed to retain their lubrication and reservoirs of impregnated sintered material should be adjacent to the bearing races.

C. Seals. Due to the short operating life of the antenna actuator, greased O-Ring seals can be considered to seal the bearing and torque motor assemblies. A double O-Ring seal with an oil reservoir between proved successful in the Mariner II antenna actuator. Seals should be of "Viton A" which has minimum outgassing and excellent resistance to deterioration. Particular attention must be given to the surface finish of the sealing surfaces.

D. Gears. Instrument gearing is recommended for position indication and would be enclosed within the lubricated bearing chamber. Gear materials will be 430 CRES for pinions and anodized aluminum for the followers. STL tests have shown these materials to suffer the least amount of degradation after over 8,000 hours of continuous running. Gear tooth surface speed would be minimized by appropriate selection of diametral pitch. Anti-backlash gearing is desirable for this application, but oversized face widths should be designed for conservative assurance of long wear life.

In addition to the mechanical design aspects of the antenna proper thermal control of the antenna is required to assure boresight stability. Both interferometer and gimbaled antennas were evaluated during the Study. Comments regarding the former are presented first.

A. Body-Mounted Antenna. The elemental interferometer antennas would probably be attached to a flat plate or a truss structure to maintain antenna spacing and alignment. Shadowing of any portion of the antenna assembly by the spacecraft or other portions of the antenna give rise to temperature gradients which cause boresight shift. To prevent this phenomenon, the rear of the antenna assembly may be covered with Mylar insulation such as NCR-2 at almost no weight penalty. It is desirable to shield the antenna structure from lunar radiation and prevent partial shading by the spacecraft itself, if the antenna is to be employed again after the initial descent. Reflections from other surfaces on the

spacecraft can generate hot spots. The possibility of such reflections being present can only be ascertained after the spacecraft outline has been determined and the antenna location established. Solar flares do not cause significant thermal perturbations near or in the vicinity of the moon.

B. Gimbaled Antenna. The gimbaled antenna was considered to consist of a pitch axis assembly, as shown in Figure 4-5, with a yoke structure going to the yaw axis. To prevent thermal distortion, the gimbal yoke may be covered with NCR-2 so that any thermal energy passing through the insulation can be readily conducted to the base of the yoke and then to the spacecraft structure itself. A temperature differential between the arms of the yoke of less than 100°F can be expected from a good thermal design. For a yoke assembly measuring 0.4 meters from pitch axis to yaw axis, the corresponding change in length is approximately 0.05 cm. The angular error induced by the 100°F thermal differential is approximately 0.05 degrees for a 0.6-meter spacing between yaw axis attachment points.

Lastly, the circuitry aspects of the lobing schemes are evaluated. A conical lober requires a single receiver channel for angle measurement and no ambiguity resolving circuitry. All data processing is easily accomplished by analog means. In implementation, it is the simplest and will fulfill the performance requirements.

In conclusion, a gimbaled conical lober is the recommended implementation to satisfy the beacon tracker requirements pertinent to this Study, because of its simplicity, ability to fulfill performance requirements, and can be integratable with the extended range altimeter. For reduced angular coverage, a body-mounted antenna would be preferred.

4.1.4.2 A Representative Antenna Assembly

A gimbaled planar array, conically scanned by electronic phase shifters, will fulfill all mission requirements. Gimbal freedom of $\pm 60 \times \pm 30$ degrees is sufficient for most guidance schemes. The array aperture is divided into four quadrants, with each quadrant excited through a solid-state phase shifter. Taylor's analysis of illumination for circular apertures[3]

(3) R. C. Hansen, "Tables of Taylor Distribution for Circular Aperture Antennas", IRE Transactions on Antennas and Propagation, January 1960, Page 23.

indicates a half-power beamwidth of 3.4 degrees and a sidelobe level of -30 db theoretically achieveable with a 0.6 meter diameter aperture, or even lower sidelobes at the expense of a slightly broader beam. Circular polarization can be obtained by crossed slots cut in the broad face of what are contiguous strips of reduced height dielectric filled waveguide, especially constructed to achieve high rigidity and lightness of weight. Lobing is accomplished by sinusoidally varying the excitation phase of each quadrant. For a 0.6-meter diameter aperture, a phase variation of approximately $\pm$70 degrees is required to yield one-way beam crossover at the half-power point.

Phase shifts in excess of $\pm$70 degrees have been obtained with temperature compensated ferrite phase shifters.(4) Balanced semiconductor phase shifters have been investigated at STL which can provide the requisite phase shift of 70 degress for a maximum insertion loss of 1.0 db. (See Figure 4-6 for an illustration of the phase shift characteristics of both units.)

Rotary joints can be eliminated by locating the r-f circuitry on the antenna. D-C power is supplied by cables and no slip rings are necessary.

Space stabilization of the antenna is indicated to decouple spacecraft maneuvers from the angle data. Figure 4-7 depicts a linearized rate integrating gyro implementation. The choice between rate and rate integrating gyros is not unique. Units of the latter type are currently under test and evaluation that require no heater power as they are thermally compensated from -55 to +100 degrees centigrade. Unit weight is 0.25 lbs.

In considering any physically realizable configuration, cognizance must be taken of the effects of bearing stiction, viscous friction, and structural compliance which give rise to a nonlinear relationship between input driving function and output response. However, no gear train stiction or backlash exists with a direct drive unit.

---

(4) "Ferrite Phase Shifters", May 1961, Rantec Corporation, Calabasas, California

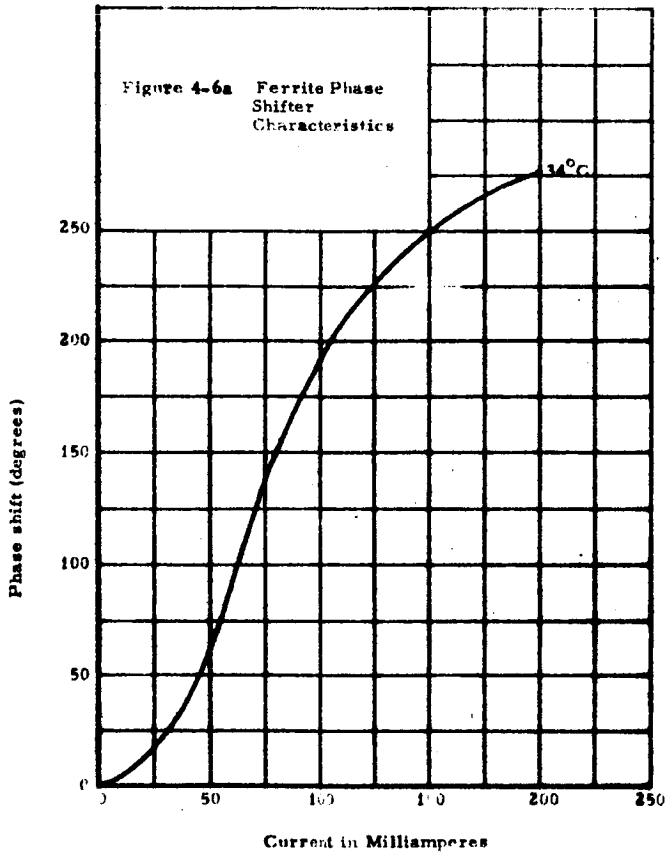

Figure 4-6a Ferrite Phase Shifter Characteristics

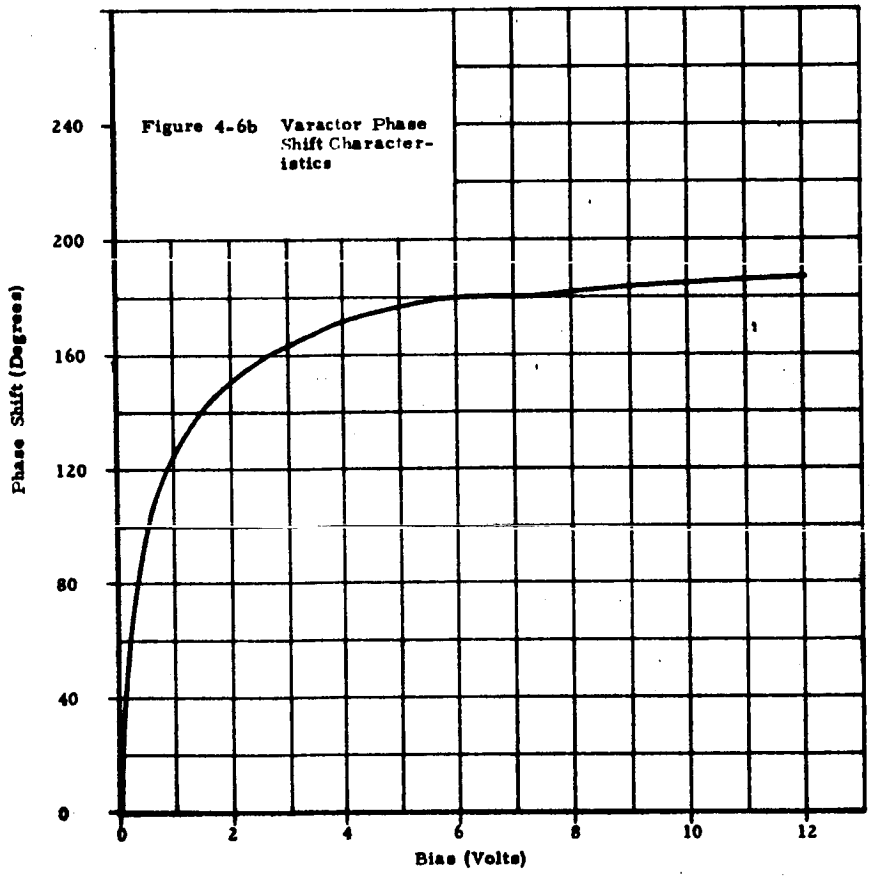

Figure 4-6b Varactor Phase Shift Characteristics

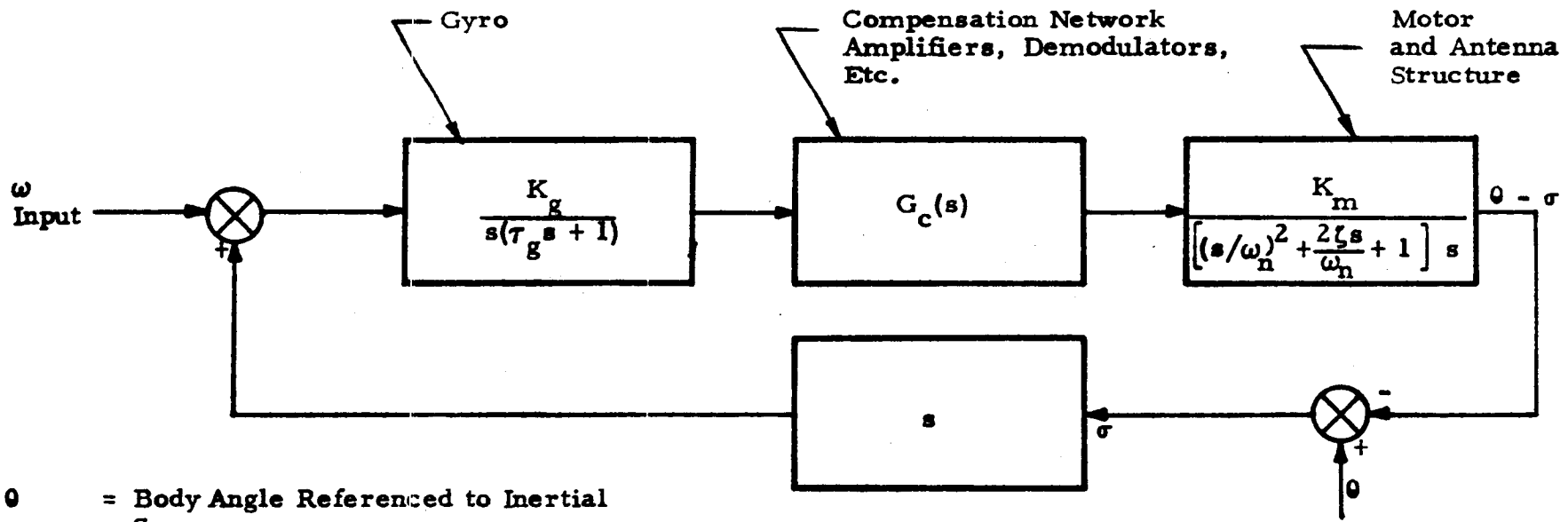

θ = Body Angle Referenced to Inertial Space.

σ = Antenna Angle Referenced to Inertial Space.

ω_{input} = Angular Rate Error Between Target LOS and Antenna Boresight Axis.

Figure 4-7 Linearized Block Diagram of Stabilization Loop

4.1.5 Acquisition

The sequence of operations performed during acquisition is described in the following paragraphs. The discussion pertains to either orbital or direct descents.

The beacon is first activated and transmits an unmodulated carrier signal, while the radar receiver is energized and its antenna is directed in a space search over a conical volume of 7-degree half angle* in a frame time of approximately 4 seconds, corresponding to a scan speed of 15^{o}/second. The highest amplitude received signal is retained in a peak detector and the angular coordinates of the antenna gimbals read into the on-board computer. After one such frame has been completed, the antenna is directed to the vicinity of the largest target return and angular lock-on consumated by disconnecting the scan programmer and closing the angle track loop. Phase lock of the carrier channel is performed simultaneously by a frequency discriminator whose output is employed to pull the VCO within the carrier phase-lock acquisition bandwidth. It is observed that the doppler uncertainty during acquisition corresponds to one-way doppler. Since the doppler uncertainty is of the order of 160 m/sec**(3σ)

*For example, a positional error of 18 km out of 180 km corresponds to 6 degrees and body attitude uncertainty may increase it to 7 degrees.

**For a direct approach trajectory, the total velocity variation between a 72-hour and 90-hour earth-moon transit time is approximately 330 m/sec. Normally, the nominal transit time is known prior to launch, but it is conceivable that low performance of the propulsion system could extend the transit time appreciably. The on-board computer would be cognizant of the variation, however, and could crudely adjust the voltage-controlled oscillator of the carrier tracking loop to center the frequency of the injected reference, thereby compensating for a fraction of the resulting doppler uncertainty. For an orbital descent, the variation in the expected doppler is due mainly to relative lateral positional error. For example, for a nominal orbital velocity of 1.8 km/sec and a 27 km lateral positional error at 360 km, the velocity uncertainty due to position alone is approximately 5 m/sec. The uncertainty in the magnitude of orbital velocity would also be small. To take a conservative approach, the acquisition bandwidth is determined by using a total doppler uncertainty of 160 m/sec.

the frequency uncertainty is given by

$$BW = 2\sqrt{|\Delta f|^2 + (3\sigma_1)^2 + (3\sigma_2)^2}$$

where

Δf = doppler uncertainty

σ_1^2 = variance in frequency of transponder crystal oscillator

σ_2^2 = variance in frequency of radar injected reference crystal oscillator

Using

$$\Delta f = 5.25 \text{ kc/s}$$

$$\sigma_1^2 = \sigma_2^2 = 1 \text{ kc/s}$$

the total acquisition bandwidth is 13 kc/s.

Next the radar transmitter, unmodulated, is energized and the carrier acquired in the transponder in a manner analogous to that utilized in the radar. The transponder transmitter is modulated with the ranging modulation and the modulation is detected at the radar, signifying carrier acquisition has been completed in the transponder. The radar transmitter is then modulated and the modulation loop acquired in the transponder, at which time a tone may be imposed on the carrier and observed at the radar, indicating acquisition is complete and data is acceptable for processing. Since no oscillator sweeping is necessary, phase acquisition is easily accomplished in less than one second.

4.1.6 Modulation Technique

The modulation objective consistent with the ranging principle used in STELATRAC is to generate two CW signals, coherently related and separated in frequency by the ranging subcarrier frequency of 4.0 to 4.15 mc. The desired distribution of power between these signals is governed by range measurement accuracy requirements and by the desire to distribute stresses on carrier and modulation phase-tracking loops so as to maximize the threshold range for tracking. Since the expected accuracy of STELATRAC ranging near threshold exceeds requirements, it seems reasonable that the choice of modulation technique should maximize the threshold range.

A comparison of alternative modulation techniques involves consideration of complexity, reliability, differential modulation phase shifts, modulator insertion loss, and power utilization for the various possible techniques. Power utilization, as used here, refers to a figure of merit (based on threshold range or range measurement accuracy) inherent in the technique and exclusive of the other factors which are practical ones. It involves, in addition to the manner in which modulation is impressed on the carrier, the technique by which the modulation is tracked in the receiver and bandwidths in which the various signal components are processed. The STELATRAC receivers are basically two-channel CW receivers and are readily adaptable to two-tracking configurations. These are:

1) A conventional phase-lock carrier tracking loop and a modulation phase-lock loop which tracks a signal derived by detecting and processing a single first-order modulation sideband. This is the technique used in the feasibility demonstration equipment.

2) A double sideband tracker in which both first-order sidebands are processed in the injected reference receiver. Both sidebands are tracked with the same offset and phase detected against a common reference. The carrier tracking error signal is obtained by summing the two phase detector outputs and the modulation tracking loop error signal is obtained by differencing them.

The relative advantages of the two techniques are critically dependent on the relative stresses (and hence relative bandwidths) of the carrier and modulation tracking loops. If the stress due to the range ambiguity resolution sweep of the modulation greatly exceeds the stress on the carrier loop due to accelerations along the line-of-sight, the carrier tracking loop bandwidth may be made small relative to the modulation loop bandwidth. In this case, the carrier channel contribution to modulation loop phase noise may be made small even though the carrier power may be considerably reduced relative to the sideband power. Phase modulation is inherently well suited to this situation, since a relatively large first-order sideband may be obtained along with a small residual carrier. The double sideband tracker

must accept equal phase noise contributions from each of the two receiver channels, but has several attractive features. These include:

1) The double sideband suppressed carrier signal generated by balanced squarewave modulation has greater first-order sideband power than any other peak power limited waveform.

2) The modulation tracking loop may be made independent of the carrier loop tracking error if the two channels are balanced.

3) The stress due to modulation sweeping may be equally distributed between two phase detectors if a balance is achieved between the two channels.

A useful criterion in comparing techniques is the signal-to-noise power ratio (per unit error) at the output of the modulation phase detector with the modulation loop open. This figure is a measure of the tracking error and, in the case of the transponder, may be interpreted as a measure of the range accuracy potential. This figure of merit has been determined for several modulation and tracking configurations. The results are presented in Table 4-1. The following definitions apply to symbols used in Table 4-1.

Λ_t = ratio of the square of sensitivity to variance for the output of the transponder modulation phase detector (the figure of merit referred to above).

Λ_r = ratio of the square of sensitivity to variance for the output of the ranging phase detector in the radar (transponder tracking both carrier and modulation).

Φ = phase noise power spectrum level in the carrier channel with carrier unmodulated (a convenient reference noise level).

B = bandwidth of ranging phase detector output filter (radar).

B_c = noise equivalent bandwidth of the carrier phase-tracking loop (transponder).

B_m = noise equivalent bandwidth of the modulation phase-tracking loop (transponder).

In determining the comparative figures of merit, a fixed peak transmitter power has been assumed, and the phase detector sensitivities have been normalized to unity.

In those cases involving phase modulation and carrier and single sideband tracking, the index of modulation has been chosen to maximize the figure of merit for the transponder, Ω_t. For the single sideband configuration, Ω_t is a good indication of relative threshold signal levels. It may be inferred that the combination of sinusoidal phase modulation and reduced carrier loop bandwidth ($B_c = B_m/5$) will track the modulation at a signal level 5.3 db below the threshold level of the current feasibility demonstration equipment. This inference is, of course, based on the assumption that narrowbanding the carrier loop does not introduce significant dynamic tracking errors in the modulation loop.

Table 4.1. Comparison of Figures of Merit for Alternative Modulation Techniques

	Ω_r	Ω_t	Relative Improvement in Ω_t
Squarewave On-Off Modulation $B_c \geq B_m$	$\frac{1}{27.6 \frac{S}{N_0 B}}$	$\frac{1}{13.8 \frac{S}{N_0 B_m}}$	---
Squarewave On-Off Modulation $B_c = B_m/5$	$\frac{1}{27.6 \frac{S}{N_0 B}}$	$\frac{1}{10.6 \frac{S}{N_0 B_m}}$	1.14 db
Sinusoidal Phase Modulation $B_c \geq B_m$	$\frac{1}{12.8 \frac{S}{N_0 B}}$	$\frac{1}{6.4 \frac{S}{N_0 B_m}}$	3.34 db
Sinusoidal Phase Modulation $B_c = B_m/5$	$\frac{1}{16.52 \frac{S}{N_0 B}}$	$\frac{1}{4.1 \frac{S}{N_0 B_m}}$	5.28 db
Sinusoidal Phase Modulation $B_c/B_m \longrightarrow o$	$\frac{1}{25.9 \frac{S}{N_0 B}}$	$\frac{1}{4.92 \frac{S}{N_0 B_m}}$	6.7 db
Squarewave Phase Modulation $B_c = B_m/5$	$\frac{1}{15.4 \frac{S}{N_0 B}}$	$\frac{1}{4.07 \frac{S}{N_0 B_m}}$	5.3 db
Balanced Squarewave Modulation (DSBSC Tracker)	$\frac{1}{9.84 \frac{S}{N_0 B}}$	$\frac{1}{4.92 \frac{S}{N_0 B_m}}$	4.5 db

Some caution must be used in comparing the figure of merit, Ω_t, computed for single sideband and double sideband tracking configurations. The difficulty is that the nonlinearity in the phase-tracking loops (which ultimately determines the hold-on capability) arises in different ways. Consider a single sideband configuration. The modulation phase detector characteristic has the form $\sin \theta$ where θ is the modulation phase error. In the double sideband tracker, the modulation frequency is halved (frequency separation between first-order sidebands is equivalent to carrier first-order sideband separation in a single sideband system) and the phase error, θ, is shared by the two phase detectors. The error characteristic obtained by summing phase detector outputs is then of the form $2 \sin \theta/2$. Whereas the two trackers have equivalent modulation phase detector sensitivities, the double sideband tracker phase detector has an extended range between phase error maxima. The resulting threshold improvement is expected to be significant, but has not been determined.

Table 4-1 indicates a figure of merit for a double sideband system with balanced modulation which closely approaches that for the single sideband system with phase modulation. Although the advantages of the former have not been quantitatively assessed, it appears to have a potential for further improved threshold performance. There are, however, inherent difficulties in instrumenting a double sideband tracker; summing and difference d-c amplifiers (with attendant drift problems) are required, and it has not been demonstrated that the optimum sideband level (squarewave balanced modulation) can be achieved with low modulator insertion loss. For purposes of assessing system performance, the more proven technique of phase modulation is used.

4.1.7 Range Measurement

The ranging technique is a variation of the conventional CW ranging technique commonly used in radio guidance systems, in which the roundtrip phase shifts of several modulation (subcarrier) waveforms impressed on a microwave carrier are measured. In the proposed system, a fine range measurement is obtained by a phase measurement on a relatively high frequency subcarrier (4 mc). Coarse range is obtained by sweeping the same subcarrier

over a known frequency range, measuring the subcarrier phase shift over a time interval encompassing the sweep, and comparing this phase shift against that predicted for the unswept subcarrier on the basis of a carrier doppler measurement. Thus, only two phase measurements are required: 1) subcarrier phase for fine ranging, and 2) carrier phase for range rate. Coarse range is determined from a comparison of the two measurements in conjunction with information about the subcarrier frequency modulation.

The range and range rate determination may be described analytically as follows:

Let ϕ_m and ϕ_c be the two-phase measurements performed by the radar receiver.

$$\left.\begin{aligned} \phi_m &= \omega_m \tau \\ \phi_c &= \omega_b \tau + \omega_c \tau \end{aligned}\right\} \qquad (5)$$

where

ω_m = subcarrier frequency, radian/sec
ω_c = carrier frequency, radian/sec
ω_b = a bias frequency on which the carrier doppler information is recovered
τ = round trip delay (2R/c)
R = range
c = velocity of propagation

The range rate is obtained by means of a cycle count of the waveform, the phase of which is given by ϕ_c over a time interval (t_a, t_b)

$$\dot{R} \approx \frac{R_b - R_a}{t_b - t_a} = \frac{\Delta R}{\Delta t} = \frac{c}{4\pi f_c} \left(\frac{\Delta \phi_c}{\Delta t} - \omega_b \right) \qquad (6)$$

Fine range is given by

$$r = R - n\lambda_m \qquad (7)$$

where n is the number of whole wavelengths of the modulation encompassed in range R, and λ_m is modulation wavelength.

$$\phi_m = \omega_m \tau = \frac{2\omega_m}{c} R = \frac{2\omega_m}{c} (r + n\lambda_m) = 4\pi \left(\frac{r}{\lambda_m} + n \right) \tag{8}$$

so that

$$r = \frac{\lambda_m \phi_m}{4\pi} - n\lambda_m \tag{9}$$

In order to examine coarse ranging, a time interval is considered in which the frequency of the modulation is swept linearly from f_o to $f_o + \Delta f$ and back to f_o as illustrated in Figure 4-8. The corresponding variation of ϕ_m between some arbitrary time, t_o, prior to initiation of sweep and a time, t, after the sweep transient has terminated is considered:

$$\phi_m(t_o) = \frac{4\pi}{c} f_o R_o \tag{10}$$

$$\phi_m(t) = \frac{4\pi}{c} (f_o + \Delta f)(R_o + \Delta R) \tag{11}$$

$$\Delta\phi_m = \frac{4\pi}{c} f_o \Delta R + \frac{4\pi}{c} R \Delta f \tag{12}$$

where

$$R = R_o + \Delta R = R(t) \tag{13}$$

Rearranging (7) yields

$$R = \frac{c}{4\pi\Delta f} \Delta\phi_m - \frac{f_o}{\Delta f} \Delta R \tag{14}$$

ΔR is available in terms of the carrier phase change.

$$\Delta\phi_c = \frac{4\pi f_c}{c} \Delta R \tag{15}$$

Thus

$$R = \frac{c}{4\pi\Delta f} \Delta\phi_m - \frac{c f_o}{4\pi\Delta f\, f_c} \Delta\phi_c \tag{16}$$

The measurements may, in principle, be taken over a sweep in either direction and the range determination is in no way dependent on the manner in which range varies during the measurement interval.

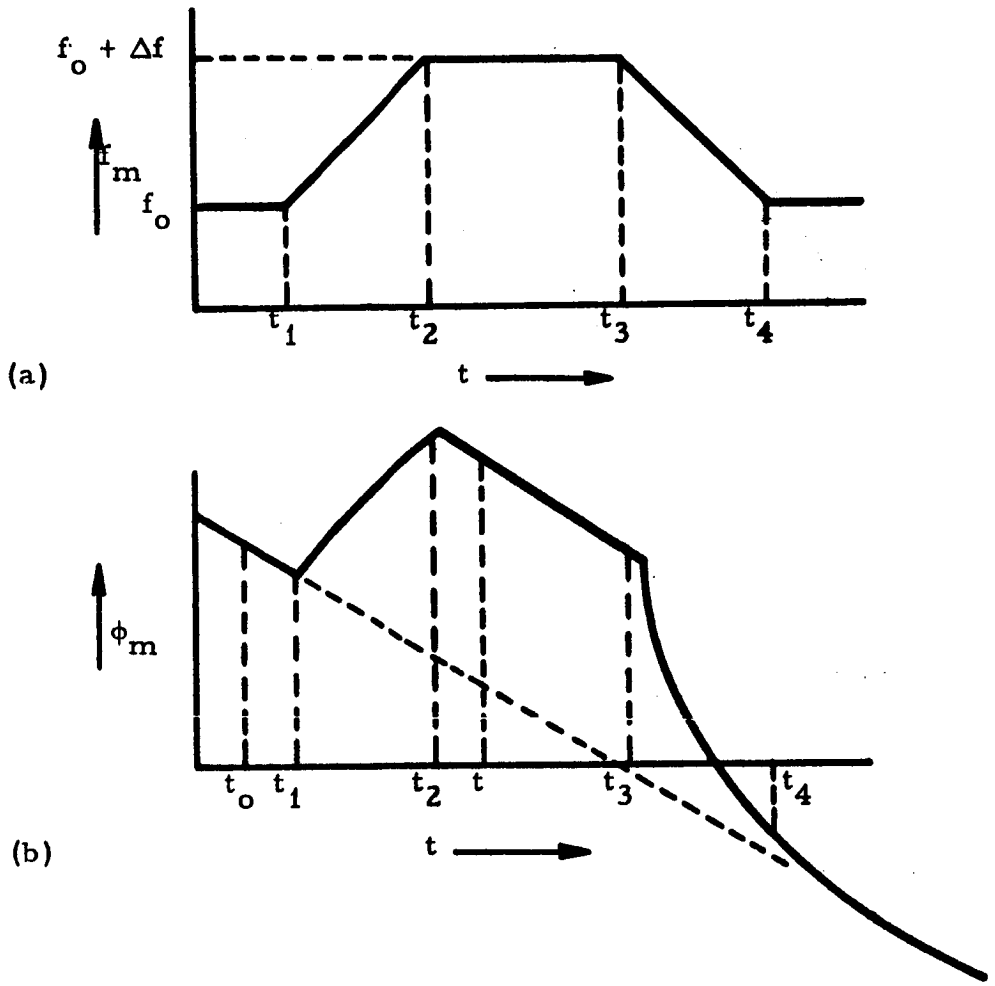

Figure 4-8 Subcarrier Frequency Sweep and Resulting Modulation Phase Change

Digital zero counting instrumentation is used to measure $\Delta \phi_o$ and $\Delta \phi_m$ and to solve equations (15) and (16) for range. The phase $\Delta \phi_m$ may change very slowly. In the interest of measuring $\Delta\phi_m$ with a zero crossing instrumentation, a bias is introduced by phase detecting carrier and subcarrier signals against references offset from each other by a convenient bias frequency. The biased version of $\Delta\phi_m$ may be supplied to a digital data processor for translation to a binary digital format for subsequent computer usage.

4.1.8 Doppler Data Extraction

Since the radar receiver tracks the received carrier, X-band doppler information appears in the receiver as a difference between injected reference and transmitted carrier frequencies. For the purpose of illustrating the method of doppler extraction, system frequencies are tabulated below. (The 4 mc subcarrier modulation is disregarded.) All frequencies are referenced to f_1 = 646.7 mc (the transmit-receive frequency offset).

Table 4-2. System Frequencies

Radar transmitter frequency	$16f_1$
Transponder received frequency	$16f_1 - 16f_1\dot{R}/c$
Transponder injected reference	$16f_1 - 16f_1\dot{R}/c - f_t$
Transponder transmitter frequency	$15f_1 - 15f_1\dot{R}/c - (15/16)f_t$
Radar received frequency	$15f_1 - 15f_1 2\dot{R}/c - (15/16)f_t$
Radar injected reference	$15f_1 - 15f_1 2\dot{R}/c - (15/16)f_t - f_r$

In the preceding table, f_t and f_r are the transponder and radar reference offset frequencies, respectively. The difference between radar transmitter and injected reference frequencies is obtained from a diode mixer on the terminated arm of the directional coupler (see Figure 4-3). Placement of the diplexer in the receiver tracking loop assures sufficient transmitter power reflection into the terminated arm of the directional coupler and, in

addition, provides the injected reference compensation for modulation phase errors introduced by the diplexer receiver arm filter. The selected output frequency of the diode mixer is

$$f_1 + 15f_1 \frac{2\dot{R}}{c} + \frac{15}{16} f_t + f_r \qquad (17)$$

A further heterodyning with a signal of frequency f_1 obtained from the transmitter frequency multiplier chain followed by filtering to remove the 4 mc subcarrier modulation (not shown in the expressions for frequency above) produces the X-band doppler frequency on a bias frequency

$$f_r + (15/16)\, f_t$$

The doppler signals are available for data processing.

4.1.9 Receiver Signal-to-Noise Ratios

The ability of the beacon tracking radar to perform the various tasks of acquisition, ranging, angle tracking, etc., is measured in terms of certain receiver signal-to-noise ratios. For purposes of generalization, the beacon equation is written as

$$P_T G_R G_T \lambda^2 = P_R (4\pi)^2 R^2 L \qquad (18)$$

where

P_T = total available power
G_T = beacon antenna gain
G_R = radar antenna gain
λ = wavelength of radiation
L = system loss factor
R = range

The terms on the right of equation (18) are considered fixed by operational and performance considerations whereas only the product on the left is deterministic in general.* However, as shown earlier, G_T should be as large

*The variation of L with frequency is neglected for purposes of this discussion.

as possible to minimize multipath while still providing adequate angular coverage. A wavelength near 3 cm will minimize flame effects in all instances and terrain bias errors in the altimeter mode. With the selection of these parameters, equation (18) can be solved for $P_T G_R$, given a minimum acceptable received signal level and an estimate of the losses, L. The STELATRAC receivers maintain solid phase-lock down to signal-to-noise ratios of +6 db in the tracking bandwidth, which corresponds to an even higher ratio in an actual implementation due to the tracking loop bandwidth reduction attributable to signal suppression in the limiter-amplifiers at low signal-to-noise ratios. The carrier tracking loop bandwidth is 200 cps and the subcarrier 1000 cps--the latter wider to track the sweeping modulation which corresponds to an acceleration term. The STELATRAC receiver effective noise figure is 11 db* and there is a 1 db foldover loss in second detection. Thus P_R, for a +6 db S/N, is -133 dbm in the carrier and -126 dbm in the subcarrier channels, respectively. The losses are summarized as follows:

Phase shifters and power divider	1.5
Circulator	0.5
Diplexer	1.25
Waveguide	0.5
VSWR	0.75
Polarization ellipticity	0.5
Field degradation allowance	5.0
Total losses	10.0 db

The transmitted power-radar antenna gain product at R = 700 km, with the carrier modulated, can be determined from:

*For angle tracking considerations, the 1 db contribution to the noise figure assignable to the operation of the bandpass limiter-amplifier does not apply, giving a 10 db NF.

	+	-
$(4\pi)^2$	22	--
R^2	116.9	--
L	10	--
G_T		11
λ^2	30.5	--
	179.4	11

$$\frac{P_T G_R}{P_R} = 168.4 \text{ db}$$

The largest $P_T G_R$ product occurs in the subcarrier channel and is +47.4 dbm as the subcarrier is suppressed 5 db below the unmodulated carrier.* The antenna gains corresponding to antenna apertures of 0.6, 0.46, and 0.3 meters operating at 0.6 efficiency and where tracking is performed at the half-power point are 30.7, 28.4, and 24.7 db, necessitating total available powers of +16.7, +19, and +22.7 dbm. During the acquisition sequence, the S/N ratio in the carrier channel is +18 db.

It is noted that if $G_R G_T \lambda^2 \sim G_R A_T$ of the radar-to-transponder link is maintained constant by proportionately increasing A_T, the transponder antenna aperture area, P_T required does not vary as the frequency decreases. With solid-state sources, the conversion efficiency increases as the output frequency is lowered and hence a favorable tradeoff exists from this consideration alone. The factors setting a lower limit on the frequency of the radar-to-transponder link are flame effects and size of the transponder antenna. The frequency of the return link is determined mainly by the specified angle tracking performance.

4.1.10 Effect of Engine Exhaust Plume on Sensor Operation

The radar sensors will be required to operate continuously throughout the landing phase of the mission. The exhaust plume of the Multimission Module landing engines can impair the operation of a radar if the radar frequency is too low. Possible effects of the plume on the radar signal are refraction, reflection, and attenuation.

*The S/N of the carrier channel is correspondingly +8 db.

In this section, an upper limit for the attenuation of an X-band signal by the plume is determined. The attenuation of the wave is shown to be negligibly small. The effects of reflection and refraction would be insignificant, as evidenced by the small attenuation, and thus have not been computed.

The Multimission Module has been assumed to have two Pratt and Whitney RL10 engines placed with their centers 1.07 meters apart, aimed parallel to the axis of the vehicle. The antenna was assumed to be 0.63 meters from the outer circumference (i.e., 2.67 meters from the centerline) of the Multimission Module.

The determination of the attenuation induced by the plume consisted of three separate computations. The concentrations of the exhaust products of the engines were determined from the fuel used, the impurity concentrations in the fuel, and the combustion chamber conditions. Assuming no electron-positive ion recombination in the plume, the electron density and water vapor density were found throughout the plume. From the particle densities, the attenuation was found using the results of earlier studies at STL.

A computer program was used to determine the exhaust products of the RL10 engine. The engine was assumed to operate at a chamber pressure of 300 psia with an oxidizer-to-fuel weight mixture ratio of 5. The fuel was assumed to be 100 percent liquid hydrogen at 20 degrees, while the oxidizer (liquid oxygen at 90°k) was assumed to contain the maximum of 0.5 percent nitrogen, as an impurity, permitted by MIL Spec. MIL-P-25508.

The gas parameters and densities in the combustion chamber, nozzle throat and nozzle exit plane, based on equilibrium flow, are shown in Table 4-3.

The electron density and temperature throughout the exhaust plume were found using a digital computer. It was assumed, very conservatively, that no electron-positive ion recombination would occur beyond the nozzle throat. This assumption was necessary because the actual recombination rates cannot be determined accurately. The attenuation calculated by this technique would be a vast upper bound for the actual attenuation.

Table 4 - 3

Equilibrium Flow Calculations for the RL10 Engine

	Chamber	Throat	Exit Plane
Pressure, psia	300.0	172.4	.5718
Temperature, $^{\circ}$R	5755	5406	2014
Density, lb/ft^3	5.67×10^{-2}	3.50×10^{-2}	3.19×10^{-4}
Velocity, ft/sec	0	5.12×10^{3}	1.40×10^{4}
MW (Molecular Weight)	11.679	11.794	12.074
C*, ft/sec	-	7745	-
Isp (opt), sec	-	159.1	436.5
Isp (vac), sec	-	297.5	454.8
C_F (opt)	-	.6612	1.8135
C_F (vac)	-	1.2359	1.8897

Gas Composition - Mole (or Volume) Fractions

Specie	x_i	x_i	x_i
H	.03675	.02783	10^{-7}
H_2	.35728	.35973	.37848
H_2O	.57798	.59344	.62572
N_2	.00164	.00170	.00179
NO	.0018	.00011	10^{-13}
O	.00143	.00074	10^{-16}
OH	.02380	.01595	10^{-9}
O_2	.00093	.00049	10^{-16}
H^+	1.11×10^{-11}	2.41×10^{-12}	1.55×10^{-33}
N^+	1.32×10^{-15}	1.66×10^{-16}	$< 10^{-38}$
O^+	3.86×10^{-13}	1.60×10^{-14}	$< 10^{-38}$
e^-	1.15×10^{-11}	2.47×10^{-12}	1.55×10^{-33}

The plume electron density and temperature were calculated for rays emanating from three points on the Multimission Module (as shown in Figure 4-9) and propagating parallel to the vehicle axis. The gas density encountered by each of the three rays specified is shown in Figure 4-10.

The radar can interact with the exhaust plume in a variety of ways. The wave can be absorbed by the lossy mechanisms in the plume. It can be refracted, i.e., bent, and emerge at an angle different from the angle at which it entered, or be reflected by the plume. The wave may also be diffused by the plume and emerge over a range of angles. The attenuation has been calculated for a straight path parallel to the vehicle axis and emanating from point C. The attenuation is very small, indicating that even for a longer curved path, where the refraction is taken into account, the attenuation will not be appreciable. It remains to analytically describe the radar-plume interaction.

The electrical conductivity of a medium is defined by

$$J = \sigma E \tag{19}$$

where

J is the current density

σ is the conductivity

E is the electric field

The current density may also be described by

$$J = Ne\,V \tag{20}$$

where

N is the particle density

e is the charge of each particle

V is the average particle velocity

The average velocity, V, of a particular particle specie is inversely proportional to the mass of the ion. For this reason, electrons will account for the vase preponderance of the current density, and hence will determine the conductivity of the medium.

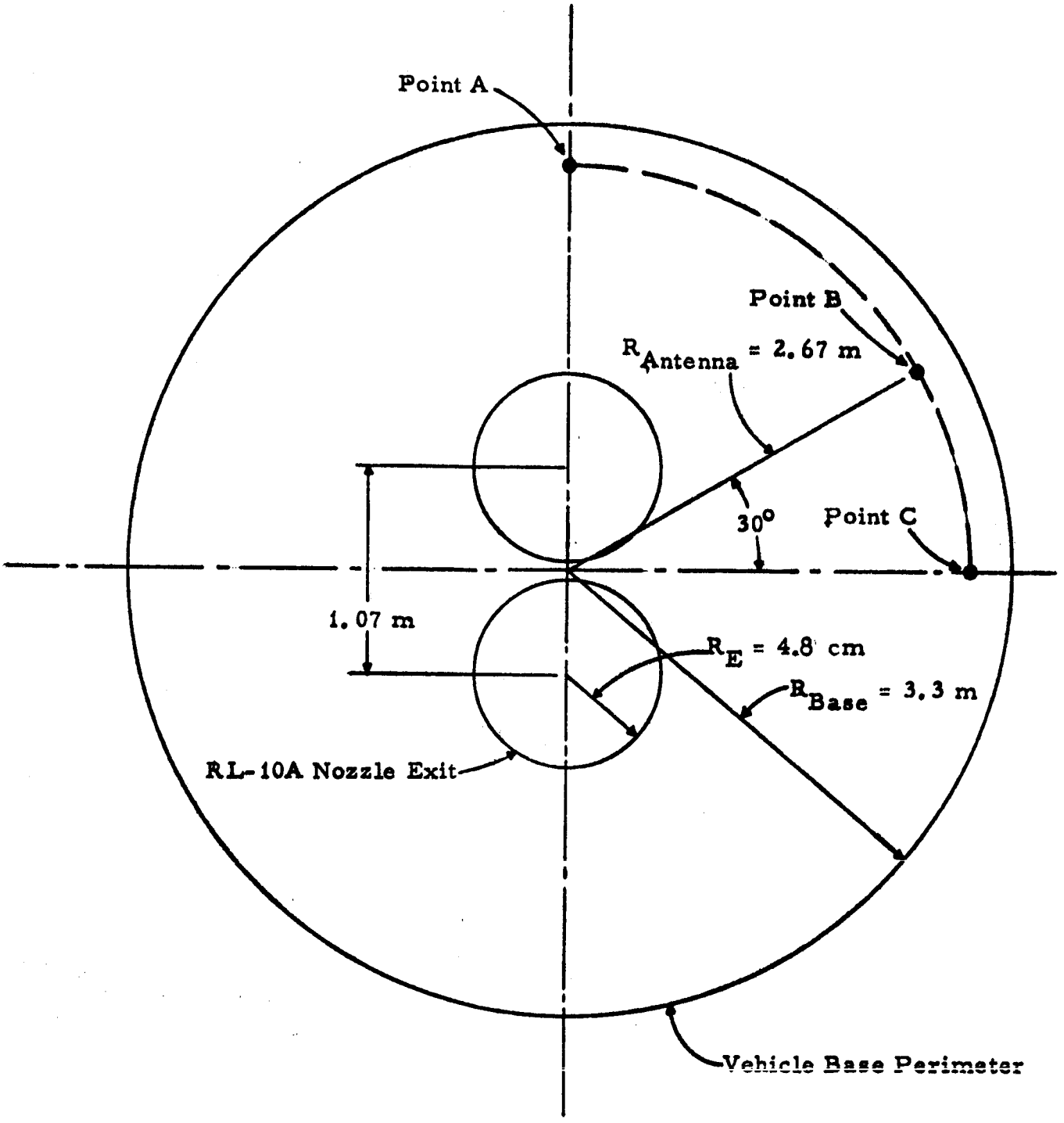

Figure 4-9 View of Vehicle Base With Two RL-10A Engine Nozzles

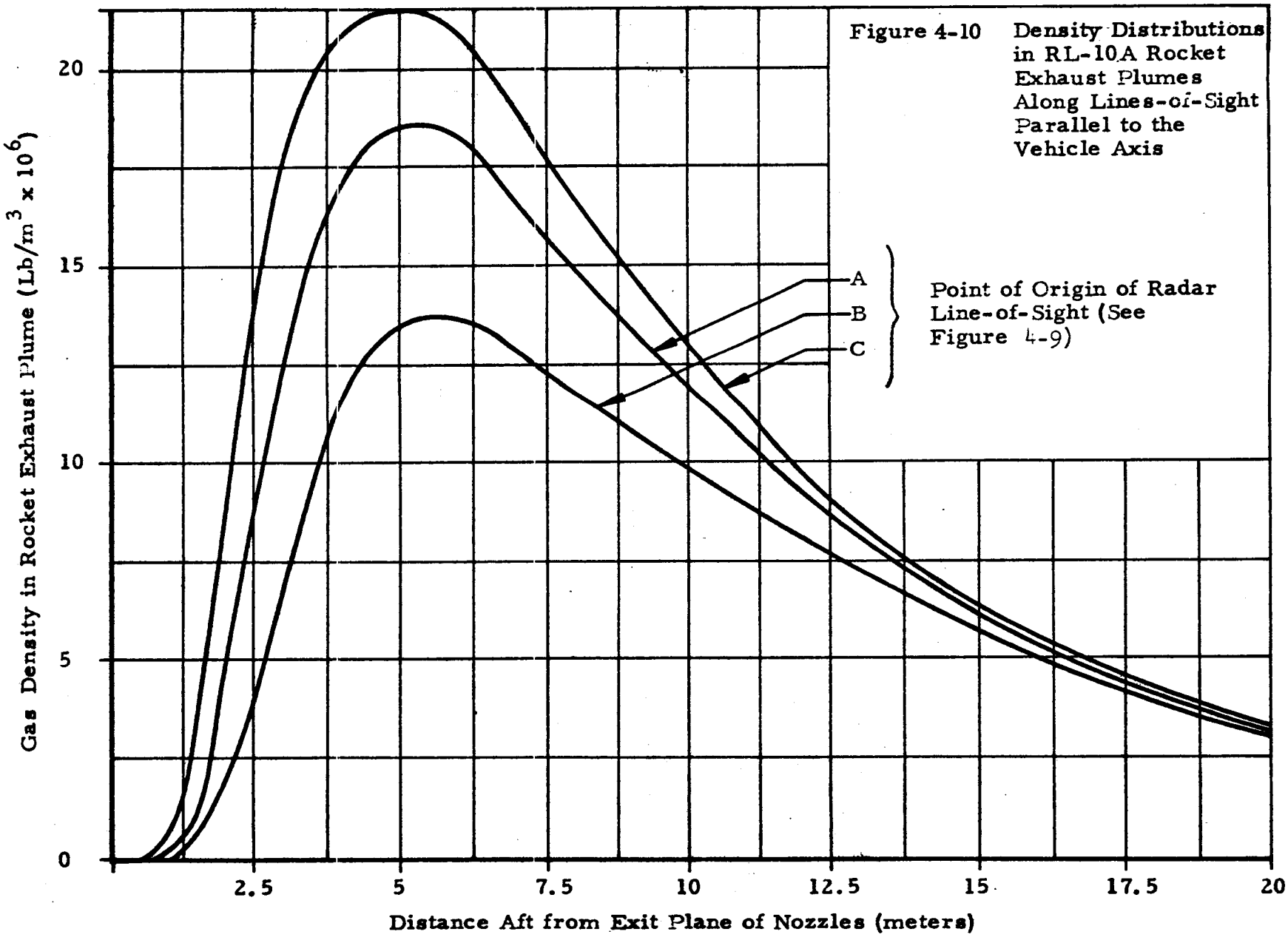

Figure 4-10 Density Distributions in RL-10A Rocket Exhaust Plumes Along Lines-of-Sight Parallel to the Vehicle Axis

The theory of conductivity for the case of free electrons undergoing arbitrary elastic collisions with neutral particles has been established by Margenau[5]. From his work:

$$V = \frac{eE}{m} (B \cos \omega t + D \sin \omega t) \qquad (21)$$

B and D, for the weak field case[2], may be written as

$$B = \frac{8\pi}{3} \beta \left(\frac{\beta}{\pi}\right)^{3/2} \int_0^\infty \frac{\phi(V)\, V^4}{\left[\phi(V)\right]^2 + \omega^2} e^{-\beta V^2} dv \qquad (22)$$

and

$$D = \frac{8\pi}{3} \beta \left(\frac{\beta}{\pi}\right)^{3/2} \int_0^\infty \frac{\omega V^4}{\left[\phi(V)\right]^2 + \omega^2} e^{-\beta V^2} dv \qquad (23)$$

where $\beta = (m/2kT)$, k being the Boltzman constant and T the temperature of the gas. $\phi(V)$ is equal to the product of the neutral particle density times a function of V, the functional form being dependent on the nature of the collisions made between the electrons and the neutral particles.

It is to be expected that, because of the high water vapor content of the exhaust gases, inelastic collisions will play an important role in conductivity theory. Electrons can induce transitions readily in the rotational states of the water molecules through interaction with their permanent dipole moments.[6] Therefore, $\phi(V)$ in equations (22) and (23) will not, in general, be the collision frequency, but an effective collision frequency.

---

(5) Margenau, H., Physical Review, "Conduction and Dispersion of Ionized Gasses at High Frequencies", Vol. 69, 1946. Page 508.

[2] i.e., the energy gained by the electron from the field during a mean free time is less than the energy lost upon collision.

(6) Altshuler, S., Moe, M. M., and Molmud, P., "The Electronics of the Rocket Exhaust". Space Technology Laboratories, Inc., Internal Memo GM-TR-0165-00397. 15 June 1958.

Studies by Altshuler[7] have shown that the cross section for momentum transfer, $Q(V)$, for electron impact on water molecules obeys the relationship

$$QV^2 = 5.9 \text{ (C.G.S. units)} \tag{24}$$

The form of $\phi(V)$ is given by

$$\phi(V) = \rho \; Q(V) \; V \tag{25}$$

where

ρ is the neutral particle density

Substituting equations (24) and (25) in equations (22) and (23) yields

$$\omega B = \frac{4}{3\sqrt{\pi}} \; x^{1/2} \left[1 - x - x^2 \, e^x \, E_i(-x)\right] \tag{26}$$

$$\omega D = \left[1 - \frac{2}{3} x + \frac{4}{3} x^2 - \frac{4}{3} \sqrt{\pi} \, x^{5/2} \, e^x \, (1 - \phi \sqrt{x}\,)\right] \tag{27}$$

where

$$x = \frac{\pi}{4} \frac{\nu^2}{\omega^2}$$

$$E_i(-x) = - \int_x^\infty \frac{e^{-t}}{t} \, dt \text{ (the exponential integral)} \tag{28}$$

$$\phi(z) = \frac{2}{\sqrt{\pi}} \int_0^\infty \exp(-t^2) \, dt \text{ (the error integral)} \tag{29}$$

The solutions for ωB and ωD are available in Reference 6. There they have been shown in graphical form as a function of (ν/ω), the collision frequency divided by the radar frequency.

The average collision frequency for electrons colliding with water molecules is given by

$$\nu = 2QV^2 \; \rho \left(\frac{m}{2\pi kT}\right)^{1/2} \tag{30}$$

(7) Altshuler, S., Physical Review, "Variational Principles for Wave Function in Scattering Theory", Vol. 107, July 1, 1957, Page 114.

where

ν is the average collision frequency

Q is the collision cross section of the water molecule

ρ is the density of water molecules

m is the mass of an electron

k is the Boltzman constant

T is the gas temperature

Combining equations (19)and (20)

$$\sigma = \frac{NeV}{E} \tag{31}$$

using equation (21)

$$\sigma = \frac{Ne^2}{m}(B - jD) \tag{32}$$

The wave equation in the C.G.S. coordinate system is

$$\nabla^2 E + \nabla\left(E \cdot \frac{\nabla\epsilon}{\epsilon}\right) + \frac{\omega^2 \epsilon E}{c^2} = 0 \tag{33}$$

where

$$\epsilon = \epsilon' + \frac{4\pi\sigma}{j\omega} \tag{34}$$

ϵ being the complex dielectric constant

ϵ' being the real dielectric constant

The solution to (33) for a plane wave yields a propagation constant given by

$$K = \alpha + j\beta = \frac{\omega}{c}\sqrt{\epsilon} \tag{35}$$

where

α is the phase shift (in radians) per unit length

β is the attenuation (in nepers) per unit length

Combining equations (32) and (33)

$$\beta\lambda = \sqrt{2\pi}\left\{\left[1 - \frac{\omega_c^2}{\omega^2}\right]\omega D\left[\left(1 + \left(\frac{\omega_c}{\omega}\right)^4 \frac{(\omega B)^2}{\left(1 - \frac{\omega_c^2}{\omega^2}\omega D\right)^2}\right)^{1/2} - 1\right]\right\}^{1/2} \tag{36}$$

where

ϵ' has been assumed to be 1; B and D are as defined by equations (26) and (27),

and

$$\omega_c^2 \equiv 4\pi N \frac{e^2}{m}$$

For the case $(\omega_c/\omega)^2 << 1$ equation (34) reduces to

$$\beta\lambda = \frac{\pi\omega_c^2 (\omega B)}{\omega^2} \qquad (37)$$

A plot of equation (37) evaluated along the ray path C of Figure 4-10 is shown in Figure 4-11. A graphical integration of Figure 4-11 yields a total X-band attenuation of 3×10^{-4} db. It is evident that an X-band radar could operate anywhere on the periphery of the Multimission Module and be essentially unaffected by the engine exhausts.

The plasma frequency is near or less than 200 mc. Hence the frequency dependence of the attenuation above 400 mc is as $(\text{frequency})^{-2}$. At S-band (10 cm), the attenuation would be 3×10^{-3} db, and at L-band (30 cm) 0.03 db. The attenuation is now becoming significant and can not be completely ignored. To permit the employment of thrust levels above 30,000 pounds without incurring degradation in sensor performance, the operational frequency should be above L-band and X-band was selected as a conservative approach in this regard.

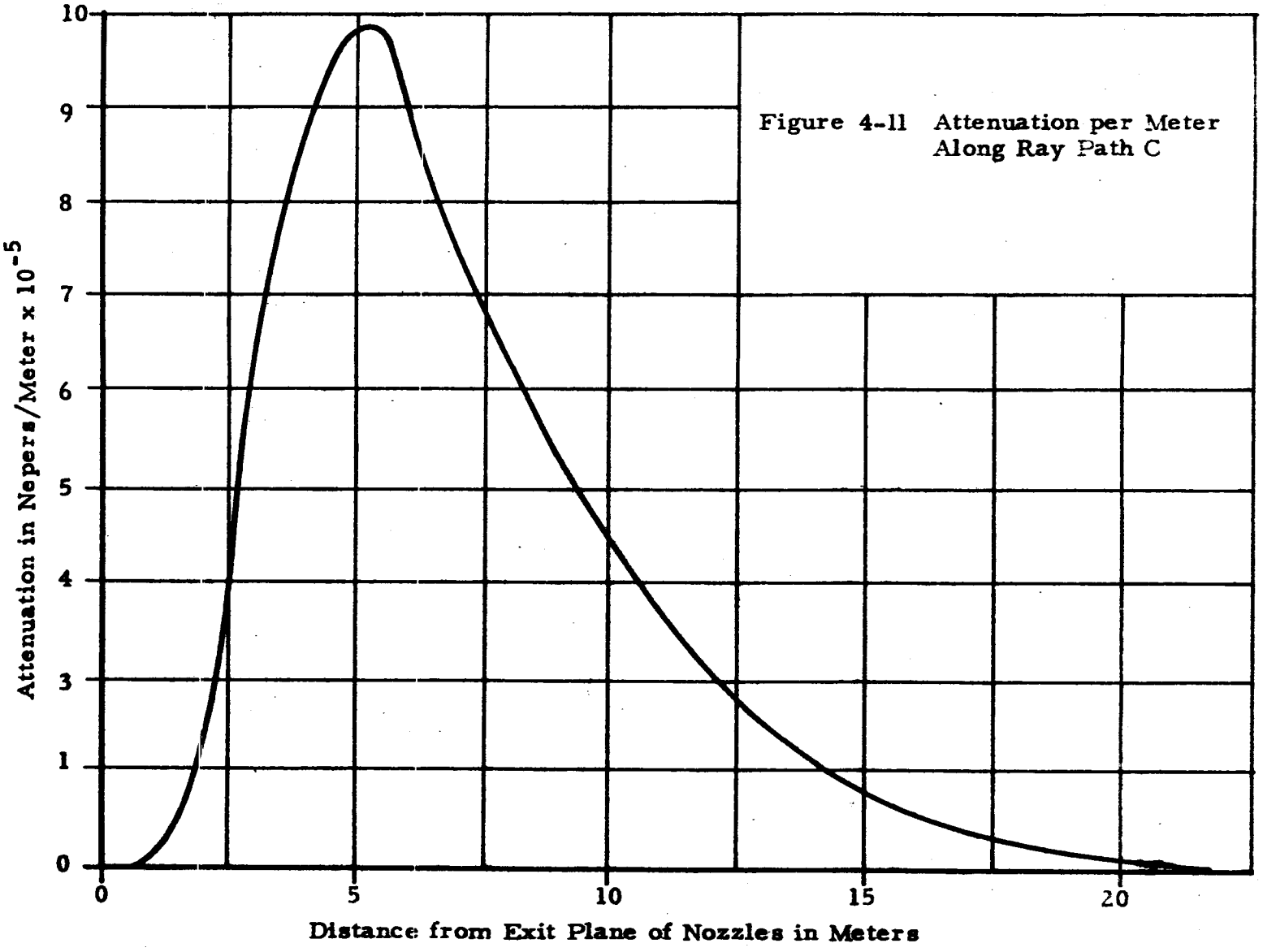

Figure 4-11 Attenuation per Meter Along Ray Path C

4.2 EXTENDED RANGE ALTIMETER

4.2.1 Introduction

The lunar descent guidance requirements down to slant ranges where a velocity meter is required can be satisfied by an altimeter functioning in the interval of 1.8 to 220 km* with a measurement accuracy of 0.5 percent. This operating range and accuracy combined pose very demanding requirements on the electronic design to achieve a system that will function with the transmitter power available from solid-state sources as the reliability constraints for the lunar landing application necessitate an all solid-state design approach. Recognition of the stringent design requirements has led to a careful evaluation of the known techniques of implementing a ranging system. In a limited peak power application, the 50 percent duty cycle or ICW method with pulse repetition frequency (PRF) tracking, some of the conventional FM techniques, and a frequency shifting technique to track altitude similar to that of the ICW method have been found to have potentiality. Of these, the PRF tracking technique with 50 percent duty factor modulation was both most promising and directly integrable with STELATRAC--one of the Study objectives.

The high altitude altimeter configuration selected for laboratory evaluation and analysis is illustrated by the simplified block diagram of Figure 4-12. Portions of two trackers have been added to the basic STELATRAC instrumentation. One of these is a frequency tracking circuit which replaces sections of the STELATRAC phase-locked carrier tracking loop and performs a similar function, i.e., to the extent of wiping off the doppler shift from the signal processed at second i-f. Frequency tracking is substituted for phase tracking because superior performance is achieved in the thermal noise region while tracking a spread spectrum signal. The frequency tracking loop output

*For the Multimission Module, if the altimeter is used to time the ignition of the first stage, an altitude capability of 700 km is desirable. For this case, an additional 10 db of gain is required. Several alternatives are available and included among these are a lower operational frequency and larger antenna aperture. The former exhibits more promise. For example, by lowering the operational frequency to the 2 gc region, an output power in excess of 1 watt can readily be provided, compensating for the 10 db increase in range attenuation. With the change in frequency, a modified antenna assembly is required as it can no longer be compatible with the X-band planar antenna of the beacon tracker. Further study in this area is indicated.

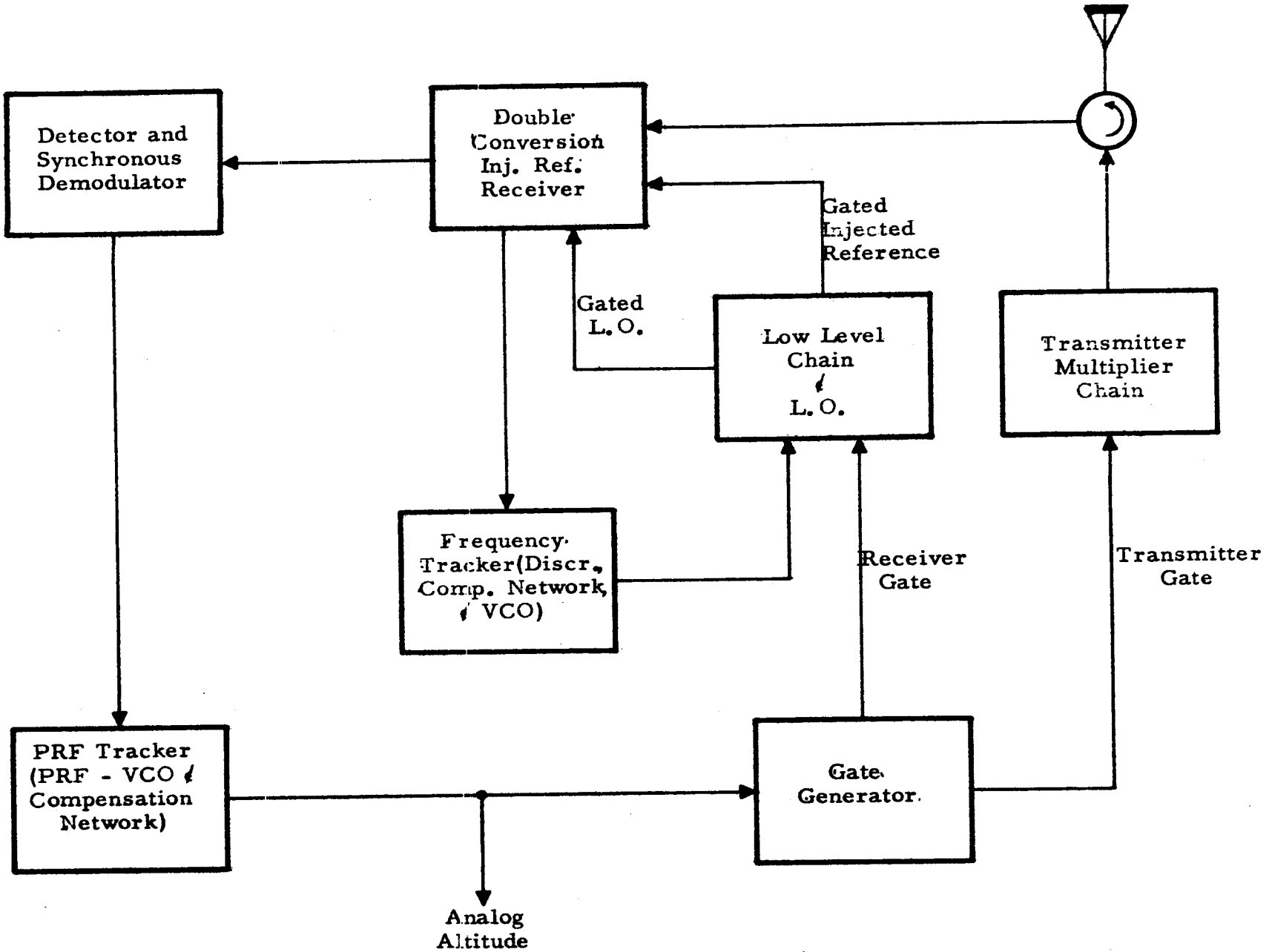

Figure 4-12 Simplified Block Diagram
Solid-State, Extended Range Altimeter

provides the injected reference signal supplied to the STELATRAC receiver. The second is the altitude tracker, which is an all electronic servo that regulates the PRF to be an inverse function of altitude. The PRF tracker provides an analog indication of altitude, and the same signal is converted to transmitter and receiver gates, which 100 percent amplitude-modulate the transmitted signal, injected reference, and local oscillator , respectively, as part of the closed loop action. Further discussion of the operating details can be found in the next section. A presentation of some of the considerations and problems involved in implementing this altimeter follows.

A difficulty common to virtually all CW techniques is that of providing sufficient transmitter-receiver isolation; in this application, approximately 160 db of isolation is required at maximum altitude. The ICW method with PRF tracking offers the most effective solution to this problem if the transmitter can be turned OFF completely. Fortuitously, one of the virtues of a solid-state multiplier chain transmitter is that ON-OFF modulation is easily and effectively provided by switching the varactor bias voltage in the final multiplier stage or stages. Also, the OFF-ON and ON-OFF transitions can be achieved in less than 20 nanoseconds, so that a very wideband signal can be transmitted to enhance the accuracy potential of the PRF tracking technique.

The signal-to-noise ratio in the signal spectrum region will be on the order of -40 db at maximum altitude. Thus considerable care must be exercised in the receiver design and in particular in the implementation of an altitude tracking error detection scheme so as to make use of the range resolution information contained in the high frequency sidebands of the transmitted signal. Essentially coherent processing of the signal is necessary at all points in the receiver to extract the error information needed to operate the electronic servo which regulates the transmitted PRF and provides analog altitude. However, the spread spectrum of the signal reflected from the lunar terrain severely limits the achievements to be realized from coherent type processing.

If necessary, the resolution capability of the basic ranging technique can be improved, at the expense of additional circuit complexity, by serrating the transmitted pulse, i.e., by placing more of the transmitted power in the

higher frequency sidebands, or similarly by tracking a multiple of the PRF once the range ambiguity is resolved. The study conducted to date has indicated that these refinements will probably not be necessary to meet the desired accuracy.

The solution to the isolation problem afforded by PRF tracking is not a complete panacea in that an adaptive servo must be built to accommodate the 120:1 variation in altitude. The need for an adaptive servo stems from two facts: 1) the error detection slope is a direct function of the time delay in the path, and 2) the dynamic requirements to track the altitude profile vary widely with altitude. Design of the PRF servo also entails the usual problems of loop disturbances such as amplifier and detector drifts, VCO drifts, and self-noise and receiver noise. Also, the tracking error is derived from the spread spectrum signal which fluctuates widely in amplitude and frequency and represents an essentially uncontrollable random disturbance to the tracking loop. Further discussion and analysis of these problems is presented in succeeding sections.

4.2.2 Functional Description and Analysis

Figure 4-13 shows a more complete block diagram of the all solid-state altimeter illustrated earlier in Figure 4-12. As indicated in the prior discussion, the altimeter functions in the ICW mode with PRF tracking and approximately 50 percent duty factor modulation.

The nominal conditions satisfied by the electronic servo which regulates the PRF is that

$$f_r = c/4h \qquad (38)$$

where f_r is the pulse repetition frequency, c is the velocity of light, and h the altitude. Altitude error sensing is performed by perturbing (dithering) the pulse repetition frequency about its nominal tracked value. The dither rate exceeds the tracking capability of the altitude tracker so that this error signal is not removed by normal loop action. The dither, in general, results in eclipsing of the received signal at the mixer as the local oscillator signal is gated precisely out of phase with the transmitter, and the relative phase shift of the two signals is 180 degrees at only one frequency for a prescribed altitude.

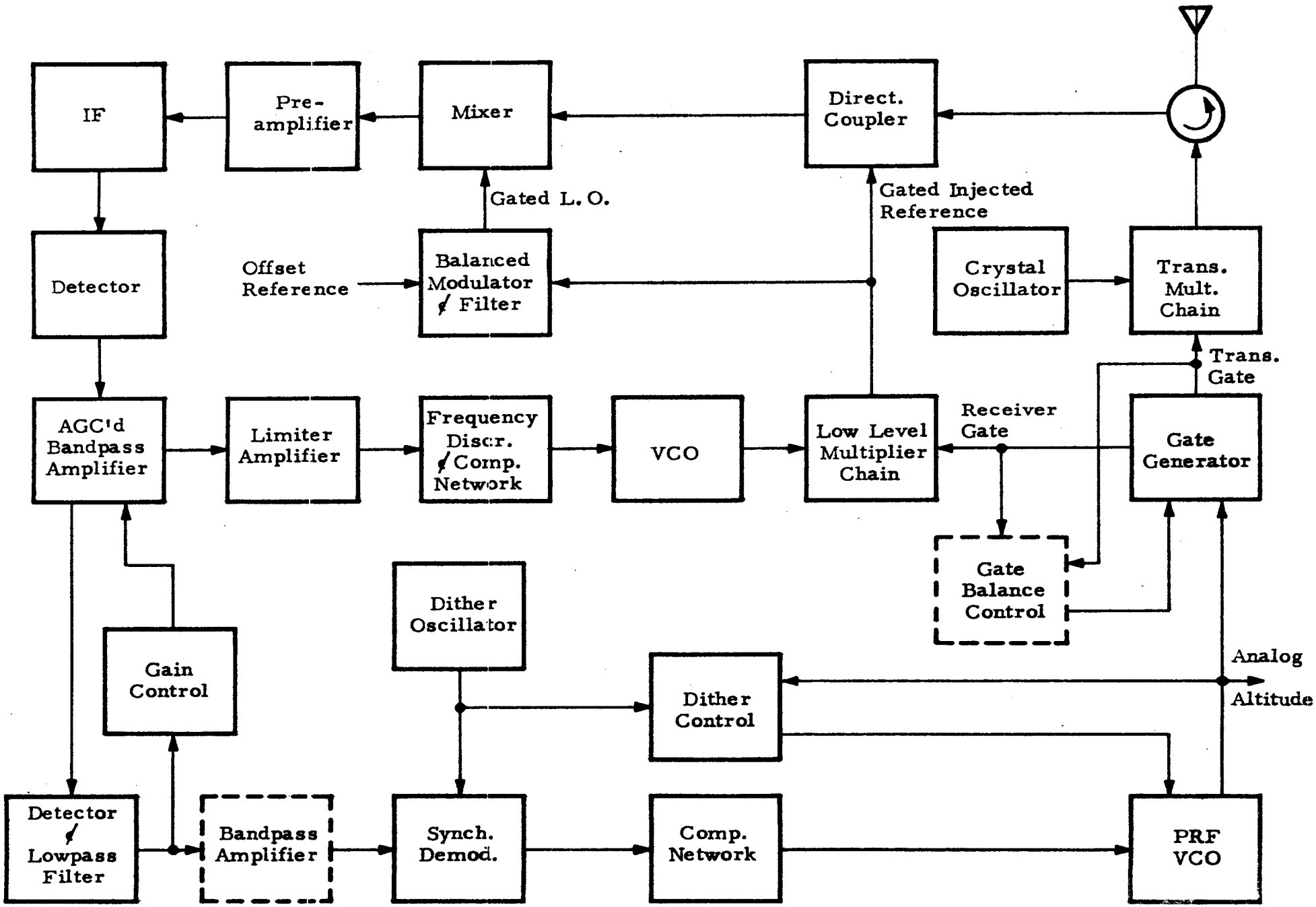

Figure 4-13 Solid-State, Extended Range Altimeter

Subsequent to the first mixer error magnitude information resides in the variation of signal level, which is amplitude-detected at the output of the second i-f. An AGC circuit will maintain the average power output of the narrowband second i-f constant to aid in gain stabilization of the closed loop. The sense of the tracking error is supplied by the synchronous demodulator which alternately multiplies the eclipsing variation by ± 1 in phase with the pulse repetition frequency dither. The signal output from the synchronous demodulator is proportional, over certain limits, to the altitude error. This error signal is processed by the compensation network and applied to the PRF VCO, the output of which is used to gate the transmitted and received signals.

The technique of detecting altitude error information at the first mixer merits more discussion. The signal power received at the altimeter for 100 mw peak transmitted power and a worst-case estimate of the scattering coefficient near vertical incidence for the beam-limited case is given by:

$$P_r = \frac{P_t \, \sigma_o \, A_r L}{4\pi \, h^2} \tag{39}$$

in which

P_t	= (peak transmitted power)	+20 dbm	
L	= (transmit-receive losses)*		-8 db
σ_o	= (scattering coefficient)		-10 db
4π			-11 db
h^2	= (2.22×10^5 meters)		-107 db
A_r	= (receiving aperture 0.6 meters, 60% eff.)		-7.8
		+20 dbm	-143.7
			20.0
P_r	= (received power, peak)		-123.7 dbm

The receiver noise density on the basis of an 11 db noise figure receiver and a 1 db foldover loss at second detection (mixing of injected reference and signal at the i-f of 65 mc) is -162 dbm/cps. The transmitted signal will be confined

*The insertion loss of the phase shifters used for lobing in the beacon tracker mode is reduced because they are set for zero phase shift. In addition, a smaller allowance for field degradation is appropriate as the beacon has been unattended for an indeterminate time period, whereas the altimeter has been checked out on the launch pad.

to approximately a 100-mc bandwidth due to the 20 nanosecond rise and decay times. Thus in the transmitted signal spectrum region, the signal-to-noise ratio at the receiver will be on the order of -40 db. In order to provide amplitude detection of the received pulse, the receiver would have to be narrowbanded to a bandwidth on the order of twice the fundamental of the PRF, corresponding to the maximum altitude of 220 km:

$$f_{r_{min}} = \frac{c}{4h_{max}} = 347 \text{ cps} \qquad (40)$$

To include only the PRF first order sidebands in the receiver bandpass at the minimum altitude of 1.8 km, where the PRF is

$$f_{r_{max}} = \frac{c}{4h_{min}} = 41.6 \text{ kc}, \qquad (41)$$

and would require a bandwidth of about 100 kc, and thus a fixed bandwidth receiver would yield prohibitive detection losses at the maximum altitude. Conventional video detection and split gate tracking is impossible at the maximum altitude with the available power, antenna aperture and noise figure. Gating at i-f or r-f then appears to represent the only remaining solution for detecting the altitude error. Narrow gates which match rise and decay times of the received or transmitted signal cannot be used to extract error information because noise and signal become highly correlated and subsequent narrowbanding in the tracker does not significantly reduce the thermal noise error. Thus wide pulse gating appears to be the only workable technique. Gating at r-f is preferable with the STELATRAC receiver for two reasons: 1) the i-f has a bandwidth limited to about 1.5 mc and thus some altitude resolution information would be lost if gates at i-f were used, and 2) the first mixer is necessarily gated to provide transmitter-receiver isolation and additional gating circuit complexity can be avoided if the altitude error detection scheme can be devised around single gate. Because of this reasoning, a dither process is suggested. It is believed that this technique represents the most accurate, efficient, and simple means for detecting altitude errors in this application. Narrowbanding following first mixer gating is now permissible, since error information due to the high frequency content of the signal is already reduced to amplitude information of the

carrier, or in the case of the spread spectrum, to amplitude variations on the signal components in the vicinity of the virtual carrier.

A frequency tracker is employed to center the doppler-shifted spread spectrum in the narrowband filter in the second i-f preceeding the detector and synchronous demodulator. The frequency tracker employs a bang-bang frequency discriminator with a crystal reference. The advantages of the nonlinear detector in this tracking loop is that it eliminates a d-c amplifier and is simpler than devices commonly used in this application. Experimental confirmation of the practicality of this device in the presence of the spread spectrum signal is necessary, however. The output of the frequency tracker VCO is multiplied to X-band in a low level multiplier chain. After modulation by the receiver gate, the signal from this chain is used for the injected reference; it is processed in the receiver along with the signal up to the output of the second i-f signal. Also, the low level chain output is offset to produce the gated local oscillator signal supplied to the first mixer.

Two gain-stabilizing devices are required to encompass mission dynamics in the altitude tracker. The first will maintain the percentage dither of the pulse repetition frequency constant, i.e., the dither magnitude must vary inversely with altitude to maintain constant linearity or fixed saturation limits for the altitude error characteristic. The second will provide compensation for the loop gain change of 120:1 due to altitude variation. Simultaneously, this adaptive device may program, along with the altitude gain compensation, additional changes in tracking loop characteristics required to accommodate the variations in equipment dynamics. Present estimates indicate a need for a bandwidth change with altitude. A computer simulation of the tracking behavior for the altitude profiles to be encountered will be necessary to firmly establish the necessity of such a requirement. It appears that this adaptive feature of the tracker may be handled by discrete switching steps rather than on a continuous basis, again a computer simulation will be required to verify this conjecture.

Figure 4-13 shows two circuits dotted in the block diagram which deserve mention. One of these is a very narrowband amplifier preceeding the synchronous demodulator. Introduction of this amplifier will be required

only if environmental tests of the synchronous demodulator show that drifts are excessive. The second is a gate balance control which may be required if adequate open loop balance (equal time duration) of the transmitter and receiver gate cannot be maintained. The effect of gate unbalance can become detrimental when the differential widths represent an appreciable fraction of the dither percentage measured in terms of phase variation of the gates at the first mixer. The unbalance appears as an increase in the dead zone width (or hysteresis area) and thus the gain of the altitude servo can be affected when the unbalance becomes large.

4.2.2.1 PRF Tracking Loop Analysis

The PRF tracking loop model, including the error detector characteristic for static time delay, can be constructed directly from a phase analog. Alternatively, the error detector characteristic may be derived as follows: For a fixed PRF, the transmitter gate is a squarewave whose Fourier expansion about t = 0 yields

$$G(t,\omega_r) = \frac{1}{2} + \sum_{k=o}^{\infty} \frac{2}{\pi(2k+1)} \sin (2k+1)\,\omega_r t \qquad (42)$$

where $\omega_r = 2\pi f_r$. To represent the dithered gate for a constant PRF, the Fourier expansion becomes

$$G\left[t,\omega(t)\right] = \frac{1}{2} + \sum_{k=o}^{\infty} \frac{2}{\pi(2k+1)} \sin \left\{ (2k+1) \left[\omega_r t + \theta_d(t)\right] \right\} \qquad (43)$$

where

$$\omega(t) = \omega_r + \dot{\theta}_d(t) \qquad (44)$$

and $\dot{\theta}_d(t)$ is the dither function which for the case of a squarewave is

$$\dot{\theta}_d(t) = \sum_{\ell=o}^{\infty} \frac{2\Delta\omega}{\pi(2\ell+1)} \sin (2\ell+1)\,\omega_d t, \qquad (45)$$

ω_d being the fundamental of the dither frequency and $\Delta\omega$ the dither deviation.

The received signal, R(t), is proportional to the transmitted signal and delayed by

$$\tau(t) = \frac{2h(t)}{c} \qquad (46)$$

Thus, neglecting proportionality factors,

$$R(t) = G\left(t - \tau, \omega(t - \tau)\right) \cos\left[\omega_o(t - \tau)\right] \tag{47}$$

The injected reference is

$$\rho_i(t) = G\left(t - \frac{T_r}{2}, \omega(t)\right) \cos \omega_c t \tag{48}$$

while the gated local oscillator signal is

$$\rho_o(t) = G\left(t - \frac{T_r}{2}, \omega t\right) \cos \omega_c' t \tag{49}$$

The output of the mixer is the difference frequency term obtained from an expansion of

$$D_1(t) = 2\left[\rho_o(t) \int R(t) + \rho_i(t)\right] \tag{50}$$

$$= G\left(t - \frac{T_r}{2}, \omega(t)\right) G\left(t - \tau, \omega(t - \tau)\right) \cos\left[(\omega_o - \omega_c') t - \omega_o \tau\right]$$

$$+ G\left(t - \frac{T_r}{2}, \omega(t)\right) \cos\left[(\omega_c - \omega_c') t\right]$$

Both signals are passed by the preamplifier and i-f. At the second detector, these signals intermodulate to produce

$$D_2(t) = A_\tau(t) \cos\left[(\omega_c - \omega_o) t + \omega_o \tau\right] \tag{51}$$

where $A_\tau(t)$ is the amplitude of second i-f signal and

$$A_\tau(t) = G\left(t - \frac{T_r}{2}, \omega(t)\right) G\left(t - \tau, \omega(t - \tau)\right) \tag{52}$$

The output of detector preceeding the synchronous demodulator is essentially the content of $A_\tau(t)$ at ω_d. Substituting (43) into (52) and expanding, we have

$$A_\tau(t) = \frac{1}{4} + \frac{1}{2} \sum_{k=0}^{\infty} \frac{2}{\pi(2k+1)} \sin\left\{(2k+1)\left[\omega_r\left(t - \frac{T_r}{2}\right) + \theta_d(t)\right]\right\}$$

$$+ \frac{1}{2} \sum_{k=0}^{\infty} \frac{2}{\pi(2\ell+1)} \sin\left[(2k+1)\left[\omega_r(t - \tau) + \theta_d(t - \tau)\right]\right.$$

$$+ \sum_{k=0}^{\infty} \sum_{k=0}^{\infty} \frac{4}{\pi^2(2k+1)(2\ell+1)} \sin\left[(2k+1)\left[\omega_r\left(t - \frac{T_r}{2}\right) + \theta_d(t)\right]\right\}$$

$$\sin\left\{(2\ell+1)\left[\omega_r(t - \tau) + \theta_d(t - \tau)\right]\right\} \tag{53}$$

Only terms from the double summation contribute to the error signal about ω_d and only for indices $\ell = k$. Thus the low frequency content of the third detector output is

$$D_3(t) = \frac{1}{4} - \frac{2}{\pi^2} \sum_{k=0}^{\infty} \frac{1}{(2k+1)^2} \cos (2k+1) \left[\omega_r \tau + \theta_d(t) - \theta_d(t-\tau) \right] \tag{54}$$

To find the amplitude of the term at ω_d, it is necessary to evaluate

$$C_1 = \frac{1}{T_d} \int_0^{T_d} D_3(t) \exp(-i\omega_d t)\, dt \tag{55}$$

Approximating $\theta_d(t) - \theta_d(t-\tau)$ by $\tau \dot{\theta}_d(t)$, recognizing that

$$\dot{\theta}_1(t) = \begin{cases} +\Delta\omega, & \text{for } 0 < t < \frac{T_d}{2} \\ -\Delta\omega, & \text{for } \frac{T_d}{2} < t < T_d \end{cases} \tag{56}$$

and evaluating (55) we find

$$C_1(t) = -\frac{1}{T_d} \left(\frac{2}{i\omega_d} \right) \frac{2}{\pi^2} \left[S\left\{ \frac{(\omega_r + \Delta\omega)\tau}{\pi} \right\} - S\left\{ \frac{(\omega_r - \Delta\omega)\tau}{\pi} \right\} \right] \tag{57}$$

where

$$S(x) = \sum_{k=0}^{\infty} \frac{1}{(2k+1)^2} \cos \left[(2k+1)\pi x \right] \tag{58}$$

Now the signal into the synchronous demodulator is d(t) and can be written as

$$d(t) = \alpha_1(t) \cos \omega_d t + \beta_1(t) \sin \omega_d t \tag{59}$$

and α_1 and β_1 are related to C_1 by

$$C_1(t) = \frac{\alpha_1(t) + i\beta_1(t)}{2} \tag{60}$$

Thus we find $\alpha_1 = 0$, and

$$\beta_1 = -\frac{4}{\pi^3} \left[S\left\{ \frac{(\omega_r + \Delta\omega)\tau}{\pi} \right\} - S\left\{ \frac{(\omega_r - \Delta\omega)\tau}{\pi} \right\} \right] \tag{61}$$

The output of the synchronous demodulator around d-c is the altitude servo error signal E(t) where, within a constant,

$$E(t) = \beta_1(t) \tag{62}$$

To evaluate the sums in β_1, it is noted that $\omega_r\tau$ stays close to π, while $\Delta\omega$ is on the order of 10 percent of ω_r, thus

$$S\left\{\frac{(\omega_r + \Delta\omega)\tau}{\pi}\right\} = \frac{\pi^2}{4}\left\{\frac{(\omega_r + \Delta\omega)\tau}{\pi} - \frac{3}{2}\right\} \tag{63}$$

and

$$S\left\{\frac{(\omega_r - \Delta\omega)\tau}{\pi}\right\} = \frac{\pi^2}{4}\left\{\frac{1}{2} - \frac{(\omega_r - \Delta\omega)\tau}{\pi}\right\} \tag{64}$$

Substituting into (62), and neglecting scale factors which have been disregarded throughout, we have

$$E(t) = (\pi - \omega_r\tau) \tag{65}$$

This same result can be realized, as mentioned at the start of the analysis, by inspecting a phase analog of the tracker and by observing that the phase shift of the PRF is $\omega_r\tau$ and the action of the servo is to maintain the receiver and transmitter gates out of phase.

Figure 4-14 shows a model of the altitude tracker consistent with the error characteristic derived above; definitions of loop parameters are presented with the figure. Included in the model, which is strictly valid only for the static case (τ fixed), is a disturbance ω_i which is used (as will be explained later) for the purpose of estimating the loop parameters required to track the altitude profile. When τ is treated as a variable, ω_i may be taken as zero, since it does not represent an actual disturbance. Since the time delay is quite small relative to the response time of the tracker, it is valid to use the representation of Figure 4-14 for variable τ to investigate the tracking behavior. Omitting the effects of drifts and receiver noise, the tracker response may be written as

$$\omega_r(t) = \psi(t) - \frac{K_v}{\tau}\int_0^t \omega_r(x)\,\tau(x)\,g_c(t-x)\,dx \tag{66}$$

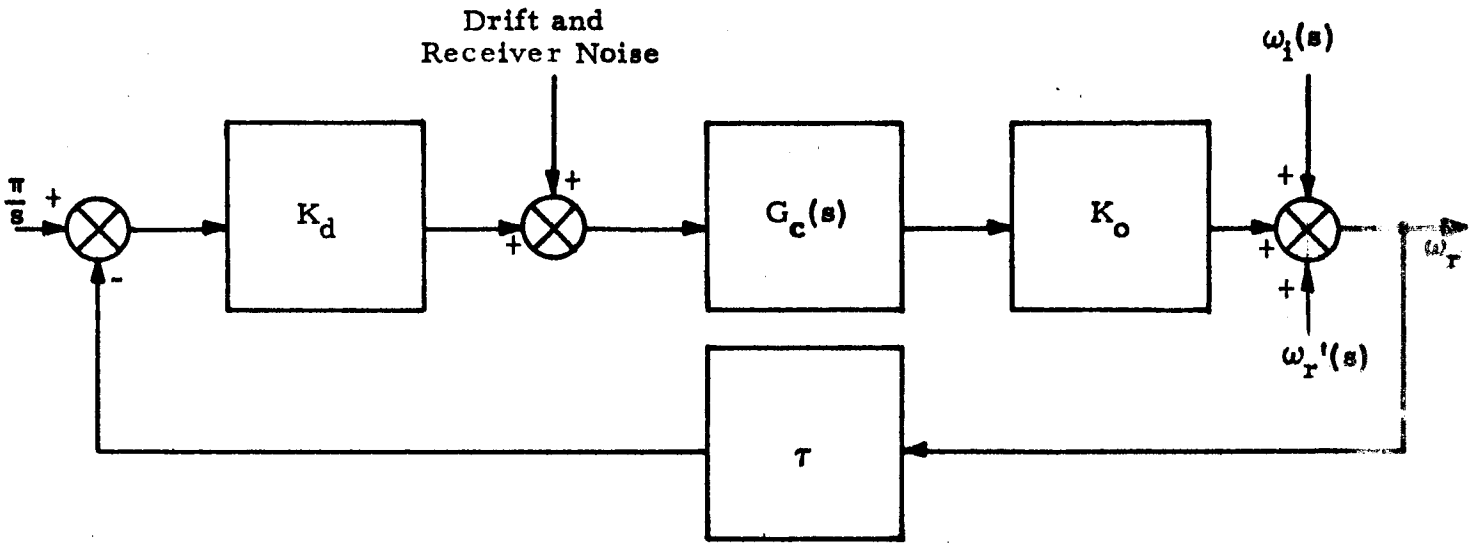

Figure 4-14 Altitude Tracker Model and Parameters

K_d = error detector constant (volt/rad)

$G_c(s) = \frac{K_c(T_2 s + 1)}{(T_3 s + 1)(K_c T_1 s + 1)}$, compensation network

K_c = DC gain of integrating amplifier

T_2 = lead time constant

T_3, $K_c T_1$ = integration time constants of compensator

K_o = scale factor of PRF VCO (rad/sec/volt)

τ = time delay in propagation path ($\tau = \frac{2h_o}{c}$ for disturbance analysis)

$$\omega_i(t) = \frac{2\pi c}{4h_o}\left\{1 - \frac{\dot{h}_o}{h_o}t + \left[\left(\frac{\dot{h}_o}{h_o}\right)^2 - \frac{\ddot{h}_o}{2h_o}\right]t^2\right\} - \omega_r'$$

ω_r' = rest frequency of PRF VCO

$$\frac{\omega_r(s)}{\omega_i(s)} = \frac{\omega_n^2}{K_v}\,\frac{(T_3 s + 1)(T_1 s + 1)}{s^2 + 2\zeta\omega_n s + \omega_n^2}$$

$K_v = K_d K_c K_o \tau$ = open loop gain

ω_n = natural resonant frequency of the tracker

ω_r = altitude tracker output (PRF)

where

$$\psi(t) = \omega_r' + \pi \frac{K_v}{\tau} \int_0^t g_c(x)\, dx \qquad (67)$$

and $g_c(t)$ is the normalized impulse response of G_c. For τ bounded, it is known from the theory of integral equations that equation (66) possesses a unique solution. A polynominal expansion for τ is inappropriate for investigating the solution of (66) for large values of time. The general solution for a polynominal expansion of τ involves at least a second order differential equation in the Laplace transform of ω_r, followed by an inversion of that solution to obtain the time response. Such a solution appears extremely difficult to say the least. Another possibility is to fit the time delay with two decaying exponentials and match coefficients in their series expansions to the polynominal approximation of τ up to the acceleration term. This form of approximation for τ leads to a first order difference equation in the Laplace transform of ω_r. The solution of this equation was beyond the scope of the present study.

Lack of a direct solution for the response of the altitude tracker at this time lead to the use of a linearized perturbation technique in order to arrive at numerical estimates of the characteristics and performance capabilities of the altimeter. At present, there has been no analytical confirmation of the goodness of the estimates derived with this technique. The required tracking loop parameters are evaluated by introducing a disturbance ω_i (shown in Figure 4-14) into the tracker which is the difference between the VCO rest frequency and the polynominal expansion of the PRF function to be generated in tracking the altitude profile in the vicinity of nominal altitude. Successive solutions at various altitudes lead to the requirements over the entire altitude profile. The dependence of ω_i on altitude and higher altitude derivatives is shown in Figure 4-14. Since the delay, τ, is held fixed at the nominal value for which the polynominal expansion is made, any departure of ω_r from $\omega_r = \pi/\tau$ represents error. The closed loop compensation parameters are selected to keep the static and dynamic errors small relative to 0.5 percent of ω_r for each of the terms in ω_i.

Inverting the transfer function of $\omega_r(s)$ for the disturbance $\omega_i(s)$ shown in Figure 4-14, the static error term for large t is

$$\epsilon_c(t) = \frac{1}{K_v}\left[\frac{c}{4h_o} - \frac{1}{2\tau}\right] \quad (\text{cps}) \tag{68}$$

The error due to the velocity term in ω_i for $t >> 1/\zeta\,\omega_n$ is

$$\epsilon_v(t) = -\frac{\dot{h}_o}{h_o}\,\frac{c}{4h_o}\left[\frac{t}{K_v} + \frac{2\zeta}{K_v\omega_n} - \frac{1}{\omega_n^2}\left(\frac{1}{K_c T_1} + \frac{1}{T_3}\right)\right] \tag{69}$$

The error due to the acceleration term in ω_i for $t >> 1/\zeta\,\omega_n$ is

$$\epsilon_a(t) = 2\left[\left(\frac{\dot{h}_o}{h_o}\right)^2 - \frac{\ddot{h}_o}{2h_o}\right]\frac{c}{4h_o}\left\{\frac{t^2}{2K_v} + \frac{2\zeta}{K_v\omega_n}\,t - \frac{t}{\omega_n^2}\left(\frac{1}{K_c T_1} + \frac{1}{T_3}\right) + \frac{\sqrt{a_R^2 + a_I^2}}{K_v\omega_n^2\sqrt{1-\zeta^2}}\left(\zeta\cos\psi + \sqrt{1-\zeta^2}\sin\psi\right)\cdot \exp\left(-\psi\frac{\zeta}{\sqrt{1-\zeta^2}}\right)\right\} \tag{70}$$

where

$$a_R = T_3K_cT_1\omega_n^2\,(2\zeta^2 - 1) - \zeta\omega_n(K_cT_1 + T_3) + 1, \tag{71}$$

$$a_I = -2\zeta\sqrt{1-\zeta^2}\,\omega_n^2T_3K_cT_1 + \sqrt{1-\zeta^2}\,\omega_n(K_cT_1 + T_3),$$

and

$$\psi = \tan^{-1}\frac{a_I}{a_R} - \tan^{-1}\left(\frac{\zeta}{\sqrt{1-\zeta^2}}\right) + \tan^{-1}\frac{\sqrt{1-\zeta^2}}{\zeta}\,. \tag{72}$$

The complexity of the acceleration error term suggests that for a preliminary estimate of the tracking loop, ω_n, one consider the loop compensation to be approximated by

$$G_c(s) = \frac{K_c(T_2s + 1)}{s^2} \tag{73}$$

In this case, the acceleration error for large t is

$$\epsilon_a'(t) = 2\left[\left(\frac{\dot{h}_o}{h_o}\right)^2 - \frac{\ddot{h}_o}{2h_o}\right]\frac{c}{4h_o}\frac{1}{\omega_n^2} \tag{74}$$

The choice of loop parameters will be made on the basis of .05 percent maximum error from each source, a conservative approach. Higher accelerations and velocities can be accommodated without incurring excessive errors or loss of lock. Using (68) and allowing the PRF offset to be 40 kc minimum, the loop gain K_v will be required to be about 2.2×10^5. This gain varies directly with τ and thus, ideally, gain compensation in the range of 120:1 will be necessary. The maximum magnitude of the acceleration coefficient for $\dot{h}_o/h_o = 0.01$ and $\ddot{h}_o/h_o = 4.1 \times 10^{-5}$ at the maximum altitude of 220 km is

$$\frac{c}{4h_o}\left[\left(\frac{\dot{h}_o}{h_o}\right)^2 - \frac{\ddot{h}_o}{2h_o}\right] = 0.028\ \frac{\text{cps}}{\text{sec}} \tag{75}$$

and at the minimum altitude of 1.85 km for $\dot{h}_o/h_o = 0.01$, and $\ddot{h}_o/h_o = 4.94 \times 10^{-3}$, is

$$\frac{c}{4h_o}\left[\left(\frac{\dot{h}_o}{h_o}\right)^2 - \frac{\ddot{h}_o}{2h_o}\right] = -98.5\ \frac{\text{cps}}{\text{sec}} \tag{76}$$

The natural resonant frequencies required for the tracker using (74) and the 0.05 percent error criteria mentioned earlier are

Maximum Altitude

$$\omega_n = 0.56\ \text{rad/sec} \tag{77}$$

Minimum Altitude

$$\omega_n = 3.1\ \text{rad/sec} \tag{78}$$

It should be noted that the variation in loop gain due to the decrease of τ would cause the bandwidth of the tracker, or ω_n, to decrease rather than increase, as required. The eventual choice of tracker bandwidth will stem from thermal and terrain noise considerations, both as to allowable unsmoothed noise output

from the tracker and the design limitation that the PRF error shall exceed the linear region of the altitude error characteristic with only small probability. Choice of the widest bandwidth required over the whole altitude profile would, of course, be desirable to avoid an adaptive mechanization.

Using the above estimates of the ω_n required for the tracker at maximum altitude, the time constant $K_c T_1$ and T_3 can be determined using (69) and the 0.05 percent error criteria. Appropriate values for these constants on this basis are

$$K_c T_1 = 8680 \text{ sec}, \tag{79}$$

$$T_3 = 78.6 \text{ sec}.$$

Now

$$T_2 \cong \frac{2\zeta}{\omega_n} \tag{80}$$

which yields $T_2 = 2.51$ sec for $\zeta = 0.707$. A check of these results in (70) indicated that the choice of ω_n from (74) yields a satisfactory error due to the acceleration term with the actual compensator.

The gains in the PRF tracker are determined as follows. Calculation of the altitude error detector slope is easily accomplished by determining the percentage modulation per percent error in PRF after the first mixer. This factor can be established by noting that PRF phase change at the mixer is

$$\Delta\phi = \frac{\delta f_r}{f_r}\pi \tag{81}$$

and thereby determining the peak-to-peak fluctuation for a dither just equal in magnitude to δf_r. Alternately, this may be calculated analytically by determining the ratio of dither fundamental to d-c at the detector preceeding the synchronous demodulator. The d-c output in terms of the previous notation is

$$C_o = \frac{1}{T_d} \int_o^{T_d} D_3(t)\ dt$$

$$= \frac{1}{4} - \frac{1}{\pi^2}\left[S\left\{\frac{(\omega_r + \Delta\omega)\tau}{\pi}\right\} + S\left\{\frac{(\omega_r - \Delta\omega)\tau}{\pi}\right\}\right]$$

$$= \frac{1}{2}\left(1 - \frac{\Delta\omega\tau}{\pi}\right) \qquad (82)$$

The percentage modulation m using (61), (63), and (64) is

$$m = \frac{4}{\pi^2}\left[\pi - \omega_r\tau\right] \qquad (83)$$

which is noted to vanish when $\omega_r \tau = \pi$, as expected. Now the percentage modulation per percent error in PRF is easily shown to be

$$\eta = m \Big/ \frac{\delta f_r}{f_r} = \frac{4}{\pi} \qquad (84)$$

If η is evaluated for a square dither waveform and substantially all harmonics of ω_d are processed by the synchronous demodulator, then $\eta = 1$. The actual slope of the altitude error characteristic is dependent on AGC'd signal level at the second i-f detector. For 5 volts peak, the altitude error slope will be

$$K_d = 1.7 \text{ volts/rad.}, \qquad (85)$$

for squarewave dither and a squarewave error signal fed to the synchronous demodulator. K_d will be slightly less if the detector output is narrowbanded to pass only the fundamental of the dither frequency. Addition of the bandpass amplifier ahead of the synchronous demodulator, shown in Figure 4-13, will result in an increase of K_d proportional to the gain of that amplifier. The altitude error characteristic is shown in Figure 4-15.

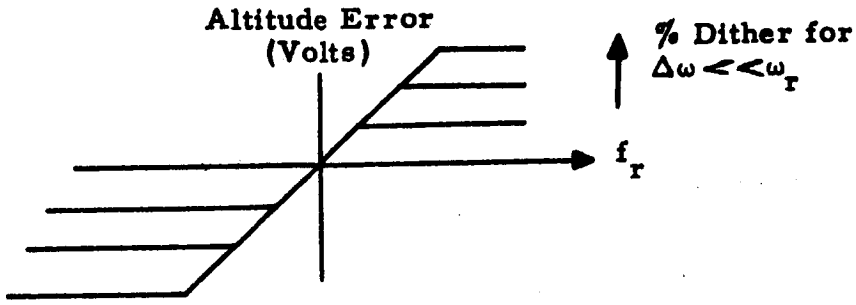

Figure 4-15 Altitude Error Characteristic

It is worthwhile noting here that K_d is independent of dither percentage and the choice of this quantity depends on the peak tracking error anticipated, the dead zone width due to the time separation of transmit and receive gates and the gate width unbalance. Present estimates indicate that 5 percent to 10 percent dither is adequate. One desires to keep this as low as possible, since the larger the dither the less the average received power. Returning to establishing the tracker gains, it has been specified (and achieved in the laboratory) that the PRF VCO should have a scale factor of 20,000 cps/volt. Thus the remaining gain is that of the integrating amplifier which at maximum altitude is

$$K_c = \frac{K_v}{K_o K_d} > \frac{2.2 \times 10^5}{2\pi(2 \times 10^4)(1.7)(1.44 \times 10^{-3})} = 716 \qquad (86)$$

K_c can be chosen greater than 716, since the bandwidth of the loop is independent of this factor. Note if a-c gain is added ahead of the synchronous demodulator, the gain required in the integrating amplifier is reduced by the same factor. The decrease in gain due to the variation in τ can be removed by increasing the gain of the integrating amplifier, but only by simultaneously changing the time constants in an appropriate manner.

For the purpose of calculating the effects of thermal noise on the PRF tracker, the effective bandwidth will be determined. The one-sided bandwidth is given by

$$B_n = \frac{1}{2} \frac{\frac{1}{2\pi i} \int_{-\infty}^{\infty} H(s)\, ds}{H(o)} \tag{87}$$

where

$$H(s) = \left| \frac{K_o G_c(s)}{1 + \frac{K_v}{K_d} G_c(s)} \right|^2 \tag{88}$$

Evaluating this integral, we find

$$B_n \cong \omega_n \frac{4\zeta^2 + 1}{8\zeta} \tag{89}$$

Substituting the minimum value of ω_n derived for the maximum altitude case and $\zeta = 0.707$, we have

$$B_n = 0.3 \text{ cps} \tag{90}$$

The following table summarizes the above estimates of the PRF tracker parameters:

Table 4-1. PRF Tracker Parameters for Maximum Altitude Condition

K_d	=	1.7 volts/rad
$K_c T_1$	=	8680 sec
T_3	=	78.6 sec
T_2	=	2.51 sec
K_c	>	716
τ	=	1440 μsec
K_o	=	1.256×10^5 rad/sec/volt
ζ	=	0.707
K_v	=	2.2×10^5
ω_n	=	0.56 rad/sec
B_n	=	0.3 cps

The performance of the PRF tracker in the presence of thermal noise can be established by calculating the noise level and spectrum shape at the output of the synchronous demodulator for given signal conditions. Then by introducing this equivalent noise at the point shown in the model of Figure 4-14, one can determine the frequency noise at the tracker output. An alternate way is to determine the error sensitivity of the PRF tracker at the first mixer, calculate the equivalent thermal noise level at the same point, taking into account all process losses, and then simply scale the thermal noise in the closed loop tracker bandwidth to frequency error. For the purposes of this estimate, the latter method is selected. Using the percentage modulation given by (84) for the case of squarewave dither and a squarewave error signal at the synchronous demodulator input, the error power per percent PRF error is 37 db below the average received signal. Assuming the received signal to be a chopped sine wave for this purpose, the average carrier power is 6 db below the peak signal power or approximately -130 dbm at maximum altitude. The receiver noise level referenced to the first mixer has been shown,following equation (39), to be -162 dbm/cps. Taking into account the chopped injected reference, the equivalent average noise density at second i-f is -165 dbm/cps. The detection loss of a linear detector is negligible if the signal-to-noise ratio is in excess of 5 db, which would exist in a 1 kc/s bandwidth. While in lunar orbit, preparatory to initiating an orbital descent, the return spectrum exceeds 1 kc/s, being of the order of 5 kc/s within the half-power points of the two-way beamwidth. However, the antenna can be readily directed to within 2 degrees of local vertical by vehicle positioning, thereby enhancing the scattering coefficient in relation to the -10 db assumed in quantifying (39). Reference to the estimated curve of lunar scattering coefficient versus incidence angle illustrated in Section 4.4.2 indicates a scattering coefficient of +3 db can be anticipated within 2 degrees of vertical. Thus, for the mission phase where a large spread spectrum is anticipated, the signal level will be such as to incur negligible detection losses. The signal-to-noise spectrum level is preserved in the synchronous demodulator when the noise peaks are small relative to the switching reference level of the synchronous demodulator. Careful design, including narrowbanding of the error signal at the dither frequency,

if necessary, will assure this condition. The average noise power density referenced to the mixer can then be taken as -165 dbm/cps. The effective bandwidth of the PRF tracker is 0.3 cps in accordance with equation (90). Therefore, the noise power which relates to tracking error is -170.2 dbm. The variance of the PRF error due to thermal noise at maximum altitude is then -3.2 db below 1 percent, or 0.7 percent rms.

Tracking errors due to drift arise from two sources, namely, the synchronous demodulator and integrating amplifier in the compensation network. The drift error for a constant disturbance V_d at the point shown in Figure 4-14 is

$$\epsilon_d = \frac{1}{2\pi} \frac{V_d}{K_d} \text{ cps} \tag{91}$$

or expressed as percent error

$$\frac{\epsilon_d}{f_r} = \frac{V_d}{\pi K_d} \times 100\% \tag{92}$$

It is observed that if the altitude error detector slope, K_d, is increased, the effects of drift are reduced. As mentioned earlier, a bandpass amplifier introduced ahead of the synchronous demodulator will keep the drift errors in tolerance. Noise saturation of the amplifier and the unbalance effects of over-driving the synchronous demodulator with noise are the difficulties associated with the provision of large gains.

4.2.2.2 Frequency Tracker Analysis

The purpose of the frequency tracker in the altimeter is to enable narrowbanding of the second i-f so as to avoid detection loss in extracting the altitude error signal. A block diagram of the frequency tracker is shown in Figure 4-13 and its model is shown in Figure 4-16.

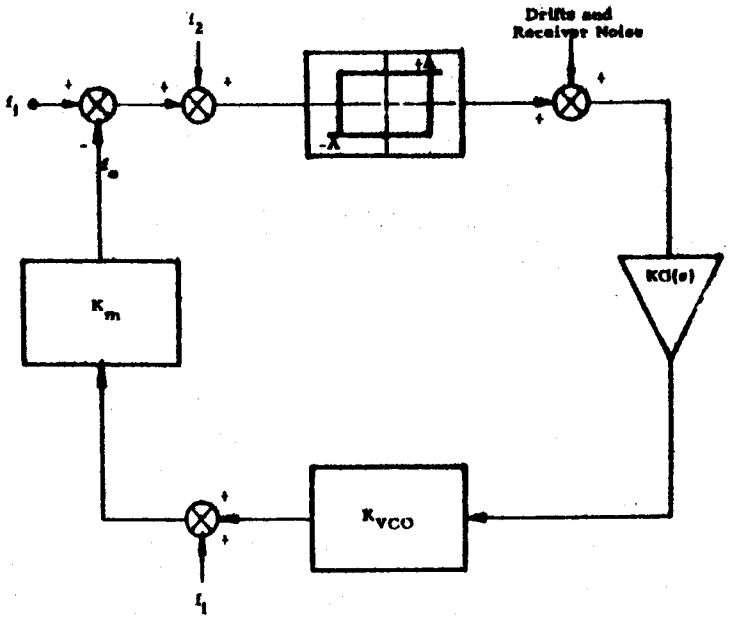

Figure 4-16 Frequency Tracker Model

K = D-C gain of compensator

K_{VCO} = VCO scale factor (850 cps/volt)

K_m = frequency multiplication factor (2304)

$KG(s) = \frac{K}{Ts + 1}$, loop compensation

f_i = center of received spectrum

f_1 = rest frequency of VCO

f_2 = discriminator reference frequency

f_o = output frequency

Based upon the specification determined in Section 3, the tracker will be required to track a maximum doppler shift of

$$f_d = \frac{2f_x \dot{R}}{c} = 167 \text{ kc} \tag{93}$$

and should possess a maximum acceleration capability of

$$\dot{f}_d = \frac{2f_x \ddot{R}}{c} = 600 \text{ cps/sec.} \tag{94}$$

The frequency error in the tracker is detected by a discriminator which exhibits a hysteresis form of nonlinearity. Choice of this particular discriminator was predicated on frequency stability and circuit simplicity, both in the discriminator itself and the tracker compensator. The discriminator employs a crystal oscillator as a frequency reference and stability is thus independent of bandwidth which is not the case in the conventional device. The discriminator bandwidth is set by a single bandpass filter centered on the reference frequency. Except for its nonlinearity, this discriminator is equivalent to the sine-cosine error detector commonly used in this application. Actually, the nonlinearity can be removed if desired at the expense of circuit complexity. Complete evaluation, including laboratory testing, will be required to justify the choice of the nonlinear mechanization. Analytical appraisal of its performance and optimum design in the presence of the spread spectrum signal and thermal noise will be difficult because of the nonlinearity.

The simplest network which can be selected for compensation of the frequency tracker is shown in Figure 4-16. The following discussion establishes that this simple filter is sufficient for signal tracking, and from it, preliminary choices of T and K are made. The step function response of the compensation filter is

$$K \left[1 - \exp(-t/T) \right] \cong Kt/T \qquad (95)$$

for small t. Hence, for a step of amplitude, A, at its input, the VCO output frequency varies with time according to

$$f_o(t) = AK_f t/T \qquad (96)$$

for small t, where $K_f = K K_m K_{VCO}$. Let the frequency deadzone in the discriminator be D cps. Then, for f_i constant, only when f_o differs from $f_i + f_2$ by as much as $\frac{D}{2}$ cps will the discriminator output exhibit a change. When this differential equals $\frac{D}{2}$ cps, a step function of magnitude A is applied to G(s), causing $f_o(t)$ to reverse its direction. A continual oscillation thus persists in the steady state. From (96), the time needed for the VCO output to traverse the deadzone, D, is

$$t = \frac{TD}{AK_f} \qquad (97)$$

and hence the frequency of oscillation is

$$f_o' = \frac{1}{2t} = \frac{AK_f}{2DT} \quad \text{cps} \tag{98}$$

while the amplitude of the oscillation is evidently $\frac{D}{2}$ cps. This is shown in Figure 4-17. The frequency of oscillation changes when $f_1 + f_2$ is not at the VCO rest frequency $K_m f_1$; however, this variation in frequency is small for the constants chosen.

T cannot be too large, since it is necessary that the loop be able to tolerate vehicle accelerations. The maximum acceleration specified in Section 3 corresponds to a frequency ramp of 600 cps/sec, which requires that

$$\frac{AK_f}{T} \geq 600 \text{ cps/sec} \tag{99}$$

Combining (98) and (99) gives a lower limit on the oscillation frequency

$$f_o' \geq \frac{300}{D} \quad \text{cps} \tag{100}$$

A further constraint is attributable to the fact that while the altimeter is transmitting, the injected reference or loop output frequency must not change by a large amount. The change accrues due to the finite time constant T and depends on the charge on the filter capacitor at the time the gate was closed. This effect is most pronounced when $f_1 + f_2$ is furthest removed from the VCO rest frequency, so that a net d-c voltage is required at the VCO to maintain loop tracking. If the maximum voltage required is V_m, the frequency offset at the end of a time Δt is

$$f_{\Delta t} = \frac{V_m K_{VCO} K_m \Delta t}{T} \quad \text{cps} \tag{101}$$

If it is required that $f_{\Delta t} < D/2$, (98) gives

$$f_o' < \frac{1}{4\mu \Delta t} \text{ cps} \tag{102}$$

where

$$\mu = V_m/AK.$$

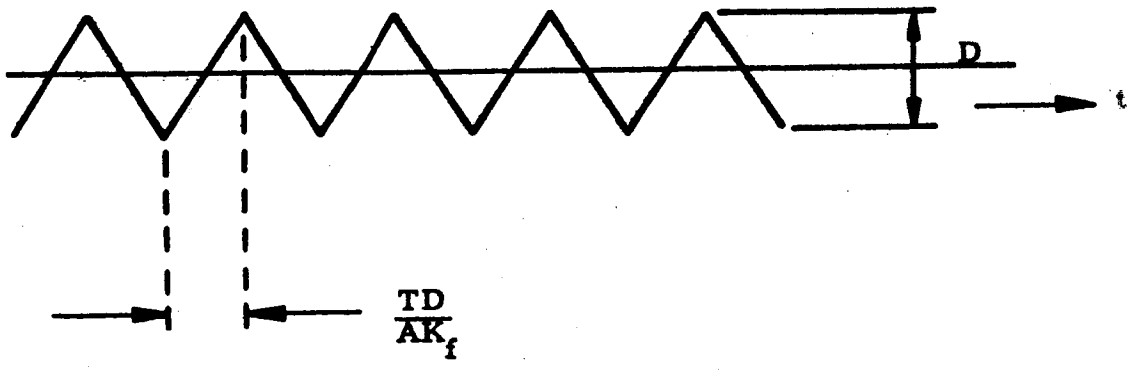

Figure 4-17 Steady-state Oscillation at VCO Output

(100) and (102) together bound the oscillation frequency. If these bounds are incompatible, the loop using G(s) of the form specified either is not able to track the specified frequency ramp adequately, or a larger error than D/2 at the end of the gate time must be tolerated. Here, Δt is the duration of the gate, and for the worst case in (102), the largest such Δt must be used. μ is the ratio of the maximum voltage required for the VCO to follow the frequency excursions to the maximum d-c voltage provided at the filter output and should be small from the standpoint of (102).

For the present discriminator, D is estimated to be on the order of 20 cps, while $\Delta t_{max} = 1.44 \times 10^{-3}$. For K = 1, (100) and (102) give

$$694 \text{ cps} > f_o' > 15 \text{ cps} \tag{103}$$

which says that a large range of f_o' is permissible using a simple RC filter for G(s). Using the circuit parameters A = 4 volts, $K_m K_{VCO} = 200$ kc/volt, and K = 1,

$$f_o' = \frac{2 \times 10^4}{T} \text{ cps.} \tag{104}$$

If f_o' is chosen to be 200 cps, which is in the range specified by (103), then

$$T = 100 \text{ sec.} \tag{105}$$

When f_i reaches its maximum differential from the VCO rest frequency, the oscillation becomes asymmetric; however, the frequency of oscillation will decrease to only 188 cps. This choice then represents a workable design with regard to signal tracking. In the altimeter application, further constraints may arise due to the desired performance in the presence of fluctuation and thermal noise. The tracker with the above parameters is anticipated to exhibit characteristics similar to that of a linear tracker having an effective bandwidth of 200 cps. One would expect that a smaller bandwidth, i.e., somewhat larger T, would be more desirable.

It is worthwhile to contrast certain features of the above nonlinear tracker design with certain features of those of an equivalent second order linear tracker. The error response of the linear tracker for a step of frequency f_d in the steady-state is known to be

$$\epsilon_s = \frac{f_d}{K_v} \tag{106}$$

when K_v is the loop gain. For the maximum doppler shift of 167 kc and a tracking error comparable to the peak error with the nonlinear tracker, i.e., about 0.005 percent, the loop gain K_v must be about 20,000. The linearized gain of the nonlinear tracker is 80,000 and there is an excess gain of 4. The time dependent error due to a ramp input in frequency is given by

$$\epsilon_r = \frac{\dot{f}_d}{\omega_n^2} t \tag{107}$$

where ω_n is the natural resonant frequency of the tracker. Now $\dot{f}_d t_{max}$ is 167 kc, thus ω_n must be about 130 rad/sec for a maximum tracking error comparable to the peak error in the nonlinear tracker. The one-sided noise bandwidth of this linear tracker would be about 75 cps, whereas the equivalent nonlinear tracker bandwidth is estimated to be 200 cps. Removal of some of the excess gain (a factor two reduction would be reasonable) would bring these effective bandwidths closer. Thus, when the hysteresis zone is sufficiently small, the nonlinear tracker may be regarded in its gross features

as a linear system. On this basis, it is satisfactory to estimate the thermal noise and fluctuation tracking error with a linear model of the tracker. Once again, the second order linear model will be used.

Thermal noise tracking error for the case where the signal-to-noise ratio is greater than unity is of interest. A singly-tuned filter somewhat wider in bandwidth than the widest spread spectrum will precede the discriminator. Here the signal-to-noise ratio must be kept above unity in order for a reasonable probability to exist that the discriminator will not threshold. In the case of exceptional noise balance of the discriminator, frequency trackers have been known to stay locked down to a signal-to-noise ratio of -6db, however, one is rarely interested in absolute threshold performance. Thus, the phase variance of the signal (assuming that for this purpose it is valid to take a sinusoid for the signal) produced by noise is given by

$$\sigma_o^2 = \frac{1}{2\Lambda} \tag{108}$$

where Λ is the signal-to-noise ratio. Further, the discriminator responds to $\dot{\theta}$ or phase rate. Taking the lowpass equivalent of the bandpass filter, a derivative term to account for the discriminator response, and the scaling of thermal noise to phase indicated by (108), the tracker output variance due to receiver noise is

$$\sigma_\omega^2 = \frac{\Phi_o}{2S}\left[\frac{1}{2\pi}\int_{-\infty}^{\infty}\left|\frac{s}{\frac{s}{2\pi\beta}+1}\,F(s)\right|^2_{s=i\omega}d\omega\right] \tag{109}$$

where

Φ_o = one-sided spectral density of receiver noise at the discriminator referred to the mixer

S = signal power at the mixer

β = half bandwidth of the filter in the second i-f preceding the discriminator

$F(s)$ = closed loop transfer function of the tracker

Note the integration in (109) from $-\infty$ to $+\infty$ accounts for the fact that the tracker is actually a bandpass element with regard to the noise spectrum and F(s) is the lowpass equivalent. Evaluating (109) for the case where

$$\frac{\omega_n}{2\pi\beta} \ll 1 \tag{110}$$

and

$$F(s) = \frac{\omega_n^2 \left| \frac{2\zeta}{\omega_n} s + 1 \right|}{s^2 + 2\zeta\omega_n s + \omega_n^2} \tag{111}$$

we have

$$\sigma_\omega = \sqrt{\pi\beta\omega_n^2 / \Lambda_o} \tag{112}$$

where $\Lambda_o = \frac{S}{N_o}$ is the signal-to-noise ratio per unit bandwidth. Expressing β in terms of the effective bandwidth at the discriminator input

$$\sigma_\omega = \frac{\omega_n}{\sqrt{\rho}} \text{ rad/sec} \tag{113}$$

where ρ is the signal-to-noise ratio into the discriminator.

Another method of determining the noise output of the frequency tracker is to compute the spectral density $W_f(\omega)$ of the frequency noise at the tracker input. Then

$$\sigma_\omega^2 = \frac{1}{2\pi} \int_0^\infty W_f(\omega) \left| F(i\omega) \right|^2 d\omega \tag{114}$$

where F is the tracker characteristic given in (111). Rice* gives the spectral density of $\dot{\theta}$ for the case of a Gaussian filter. This quantity is given in closed form only for the case of high signal-to-noise ratios and is valid in the region of interest here. The expression is

$$W_f(\omega) = \frac{1}{\rho\,\sigma\sqrt{2\pi}}\,\omega^2 \exp\left(-\frac{\omega^2}{8\pi^2\sigma^2}\right) \frac{\text{rad/sec}^2}{\text{cps}} \tag{115}$$

* S. O. Rice, "Properties of a Sine Wave Plus Random Noise", Bell Telephone Systems Technical Publications, Monograph, B 1522.

where W_f is the one-sided density, σ is a measure of the spectrum width, and ρ is the signal-to-noise ratio as above. Substituting in (114), using the tracker characteristics given by (111) for F, and evaluating for small $\omega_n/2\pi\sigma$,

$$\sigma_\omega = \frac{\omega_n}{\sqrt{\rho}} \text{ rad/sec} \tag{116}$$

It is observed that (116) agrees with the previous result given by (113).

Fluctuation noise due to the spread spectrum signal can be calculated using (114) when W_f is evaluated for the case of zero signal. The spread spectrum is Gaussian in shape and thus the relations given by Rice for W_f are applicable. The signal spectrum is given by

$$W(f) = \frac{\psi_o}{\sigma\sqrt{2\pi}} \exp \left[- (f - f_o)^2/2\sigma^2 \right] \tag{117}$$

where ψ_o is the signal power and σ is related to the bandwidth of the signal (1.18σ is the 3 db bandwidth). For this spectrum shape

$$W_f(\omega) = 2\pi \left\{ 2\sigma\pi^{3/2} \sum_{k=1}^{\infty} k^{-3/2} \exp \left[- \omega^2/16\, k\pi^2 \sigma^2 \right] \right\} \tag{118}$$

Note that with the factor of 2π, the units of W_f are $(\text{rad/sec})^2/\text{cps}$. Now the tracker characteristic given by (111) can be written as

$$\left| F(i\omega) \right|^2 = \frac{1 + 4\zeta^2 \left(\frac{\omega}{\omega_n} \right)^2}{\left[\left(\frac{\omega}{\omega_n} \right)^2 + \xi^2 \right] \left[\left(\frac{\omega}{\omega_n} \right)^2 + \bar{\xi}^2 \right]} \tag{119}$$

where

$$\xi = \zeta + i\sqrt{1 - \zeta^2} \tag{120}$$

$$\bar{\xi} = \zeta - i\sqrt{1 - \zeta^2}$$

Separating into partial fractions,

$$\left|F(i\omega)\right|^2 = \frac{1}{(\xi^2 - \bar{\xi}^2)} \left[\frac{1 - 4\zeta^2 \bar{\xi}^2}{\left(\frac{\omega}{\omega_n}\right)^2 + \bar{\xi}^2} - \frac{1 - 4\zeta^2 \xi^2}{\left(\frac{\omega}{\omega_n}\right)^2 + \xi^2} \right] \qquad (121)$$

Substituting into the relation given by (114)

$$\sigma_\omega^2 = \frac{2\sigma\pi^{3/2}}{(\xi^2 - \bar{\xi}^2)} \sum_{k=1}^{\infty} k^{-3/2} \left\{ (1 - 4\zeta^2 \bar{\xi}^2) \int_0^\infty \frac{\exp(-\omega^2/16\, k\, \pi\sigma^2)}{\left[\left(\frac{\omega}{\omega_n}\right)^2 + \bar{\xi}^2\right]} d\omega \right.$$

$$\left. - (1 - 4\zeta^2 \xi^2) \int_0^\infty \frac{\exp(-\omega^2/16\, k\, \pi^2\sigma^2)}{\left[\left(\frac{\omega}{\omega_n}\right)^2 + \xi^2\right]} d\omega \right\} \qquad (122)$$

Evaluating the integrals,

$$\sigma_\omega^2 = \frac{2\sigma\pi^{3/2}}{(\xi^2 - \bar{\xi}^2)} \sum k^{-3/2}$$

$$\left\{ \frac{\omega_n}{\xi} (1 - 4\zeta^2 \bar{\xi}^2) \frac{\pi}{2} \exp\left(\frac{\bar{\xi}^2 \omega_n^2}{16\, k\, \pi^2 \sigma^2}\right) \left[1 - \operatorname{erf}\left(\frac{\xi\omega_n}{4\pi\sigma k^{1/2}}\right)\right] \right.$$

$$\left. - \frac{\omega_n}{\xi} (1 - 4\zeta^2 \xi^2) \frac{\pi}{2} \exp\left(\frac{\xi \omega_n^2}{16\, k\, \pi^2 \sigma^2}\right) \left[1 - \operatorname{erf}\left(\frac{\xi\, \omega_n}{4\pi\sigma k^{1/2}}\right)\right] \right. \qquad (123)$$

For small $\omega_n/2\pi\sigma$,

$$\sigma_\omega^2 \cong \frac{\omega_n \sigma\, \pi^{5/2}}{\xi + \bar{\xi}} \left(\frac{1}{|\xi|^2} + 4\zeta\right) \sum_{k=1}^{\infty} k^{-3/2} \qquad (124)$$

Rice gives the value of $\sum k^{-3/2}$ as 2.61237. Substituting for the remaining parameters, the variance of the fluctuation noise at the tracker output is

$$\sigma_\omega^2 = (2.61) \frac{\omega_n \sigma\, \pi^{5/2}}{2\zeta} (1 + 4\zeta^2) \quad (\text{rad/sec})^2 \qquad (125)$$

With $\zeta = 0.707$, and substituting for ω_n in terms of the one-sided noise bandwidth of the tracker, the fluctuation variance in $(\text{cps})^2$ is

$$\sigma_f^2 = 4.63\,\sigma^2 B_n \ (\text{cps})^2 \tag{126}$$

Now $1.18\,\sigma = \Delta f_d$, where Δf_d is defined to be the 3 db signal spectrum width; thus

$$\sigma_f \cong 2\sqrt{\Delta f_d\, B_n} \ (\text{cps}) \tag{127}$$

For vertical incidence and the velocity vector normal to the beam axis

$$\Delta f_d \cong \frac{2V}{\lambda}\,\theta_B \tag{128}$$

and in general

$$\Delta f_d \cong f_d\,\theta_B \tan\alpha \tag{129}$$

where in (128) and (129)

V = velocity vector
λ = transmitted wavelength
θ_B = two-way half-power beamwidth
α = angle between the velocity vector and the beam axis
f_d = doppler shift, $\frac{2V}{\lambda}\cos\alpha$, along the beam axis.

Substituting for the tracker's effective bandwidth

$$\bar{T} = \frac{1}{4B_n} \tag{130}$$

where $\bar{T}$ is the equivalent smoothing time of the tracker, the percentage fluctuation error in the general case, neglecting the skewness of the spectrum, is

$$\frac{\sigma_f}{f_d} \cong \frac{\sqrt{\lambda\theta_B \sin\alpha}}{\sqrt{2V\,\bar{T}\cos\alpha}} \times 100\% \tag{131}$$

For vertical incidence and horizontal velocity, the standard deviation of the fluctuation error is

$$\sigma_f = \sqrt{\frac{2V\,\Theta_B}{\lambda \bar{T}}} \quad \text{cps} \tag{132}$$

4.3 SLANT RANGE TRACKER—VELOCITY METER

4.3.1 Introduction

The vernier phase of lunar descent guidance per the specifications of Section 3 requires a slant range tracker and velocity meter to function in the altitude or slant range interval of 0 meters to 10 km.* A rate capability up to 550 m/sec in the slant range direction and to 120 m/sec in the lateral direction is required. Accuracy requirements in slant range are 1% $\pm$1 meter and in rate are 1% $\pm$0.5 m/sec. While the operating range of this sensor is markedly reduced compared with the extended range altimeter, many of the design problems are common to the two sensors. A configuration is proposed which incorporates the basic 50% duty factor technique with PRF tracking for the upper portion of the altitude range. For low altitudes, a solution is afforded by the application of the accurate ranging techniques devised for STELATRAC, and thus a separate sensor is not required in this region. Three velocity tracking channels are necessary to implement the velocity meter with one also being used to determine slant range.

Many of the modules in the slant range tracker-velocity meter are common to the beacon tracker-extended range altimeter. Included among these are the solid-state transmitter. In addition, many modules will be identical except for slight variations in circuit constants to accommodate particular requirements. In the antenna area, care will have to be exercised to avoid acquisition difficulties due to antenna sidelobes, and beam pointing inaccuracy due to misalignment.

Figure 4-18 shows a simplified block diagram of the slant range tracker-velocity meter. Three frequency tracking channels are used to extract the components of vehicle velocity along the three beam axis. The computation of lateral rates uses the difference of vehicle velocity along two pairs of beam axes and it has been found convenient to extract this data from the two beams which point 20° from the vehicle longitudinal axis

*A minimum altitude of 0 meters is referenced from the antenna aperture to the ground. Due to the landing structure height, the actual height of the altimeter above the ground would be several meters.

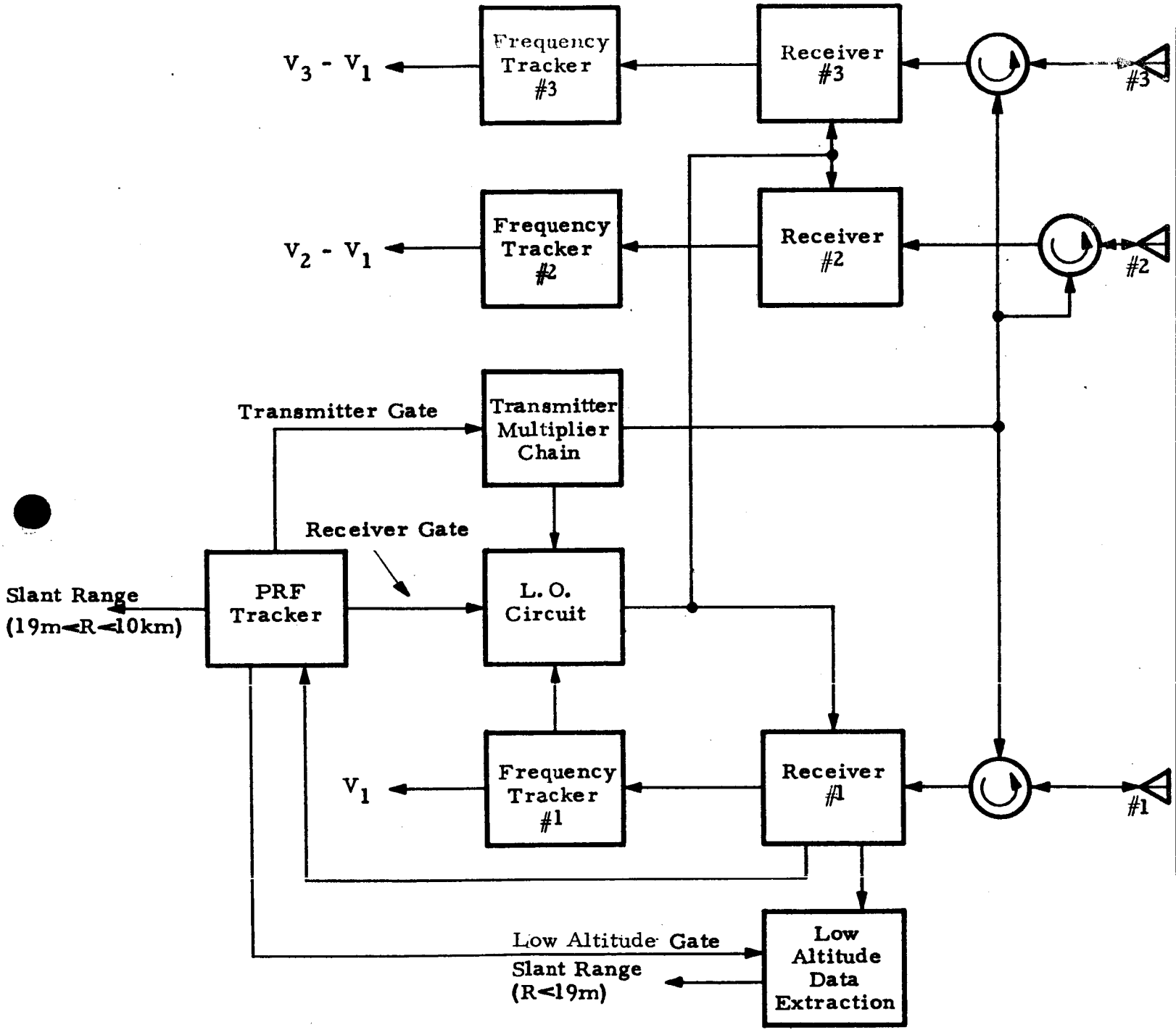

Figure 4-18 Simplified Block Diagram, Slant Range Tracker - Velocity Meter

and are directed in orthogonal planes containing this axis. The third beam is oriented along the longitudinal axis and is designated channel 1 in Figure 4-18. A PRF tracker in this channel regulates the period of the transmitted signal to be an inverse function of altitude in exactly the same manner described in Section 4.2 for the extended range altimeter. The frequency tracker in this channel provides the slant range rate associated with channel 1 as well as a doppler shifted local oscillator signal for all three channels. This local oscillator signal is used in channels 2 and 3 and serves to provide the desired velocity difference information mentioned above. The tracker local oscillator signal is necessary in channel 1 to enable narrowbanding of the first i-f so as to permit an appropriate choice of the second i-f frequency and the corresponding tracker elements. When the landing vehicle descends to a slant range or altitude of about 19.0 m, the PRF tracker ceases its tracking function and the PRF is held fixed at a frequency of 4 mc. A dual channel injected reference processor similar to that of the STELATRAC instrumentation accurately extracts the phase shift of the 4 mc PRF fundamental around the propagation path to provide unambiguous range data below 19.0 m.

4.3.2 Subsystem Description and Analysis

Figure 4-19 shows a more complete block diagram of the solid-state slant range tracker-velocity meter illustrated earlier in Figure 4.18. As mentioned above, this sensor operates in a 50% duty factor mode with PRF tracking to an altitude or slant range of 19.0 m. Measurements of range below 19.0 m is achieved by accurately extracting the phase shift of the PRF fundamental, held at 4 mc, using STELATRAC techniques. A frequency tracker is used in each channel to determine the center of the doppler shifted spread spectrum or the velocity of the spacecraft along each beam axis. The frequency tracker in the slant range channel also serves to narrowband the receivers of all three channels.

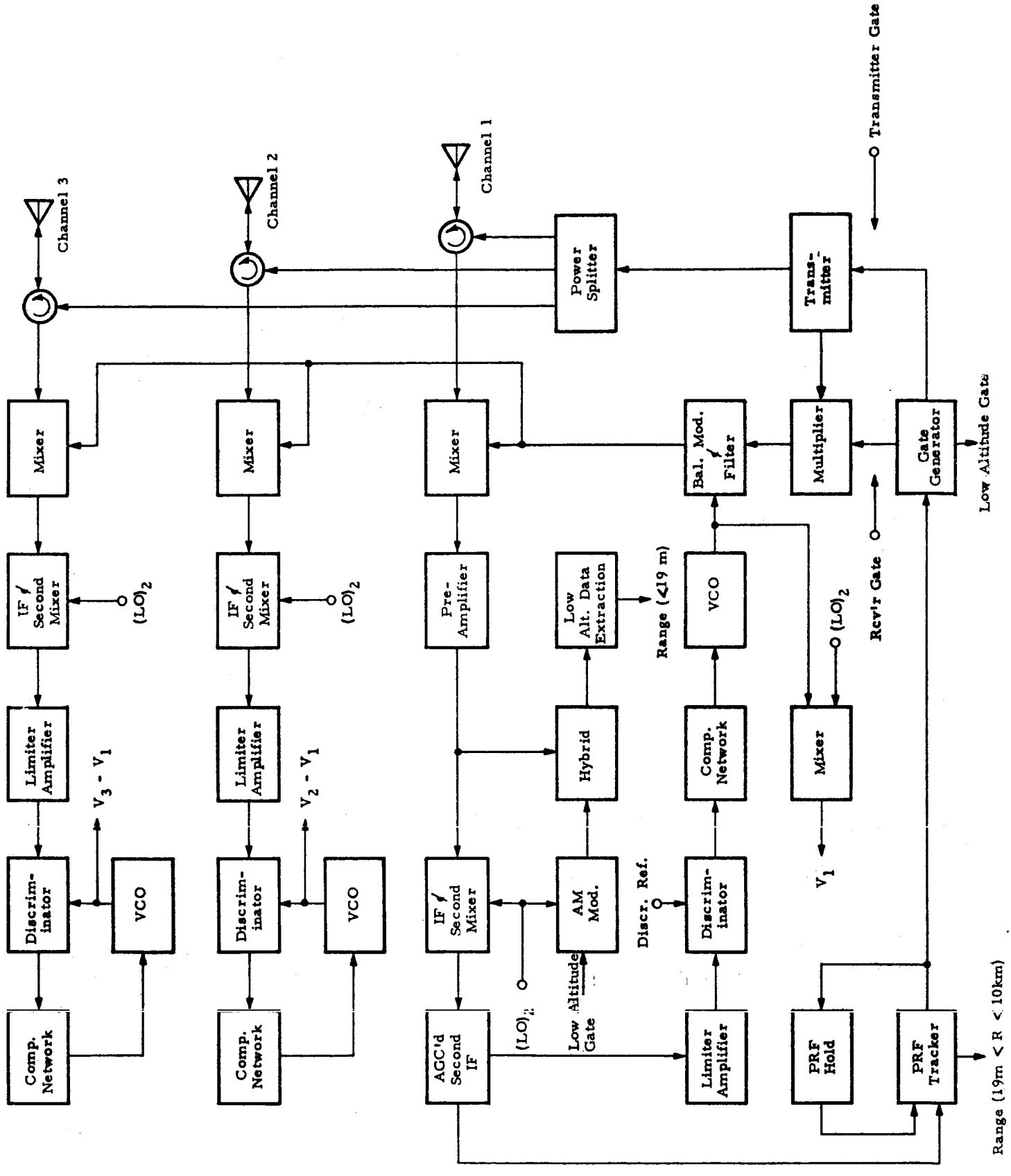
Channel 3
Channel 2
Channel 1
Power Splitter
Transmitter
Transmitter Gate
Mixer
Mixer
Mixer
Bal. Mod. / Filter
Multiplier
Gate Generator
Low Altitude Gate
IF / Second Mixer
IF / Second Mixer
Pre-Amplifier
Low Alt. Data Extraction
Range (<19 m)
VCO
Rcv'r Gate
$(LO)_2$
$(LO)_2$
$(LO)_2$
Limiter Amplifier
Limiter Amplifier
Hybrid
Comp. Network
Mixer
$V_3 - V_1$
$V_2 - V_1$
V_1
Discrim-inator
VCO
Discrim-inator
VCO
IF / Second Mixer
AM Mod.
Discr. Ref.
Discrim-inator
Comp. Network
Comp. Network
AGC'd Second IF
$(LO)_2$
Low Altitude Gate
Limiter Amplifier
PRF Hold
PRF Tracker
Range (19m < R < 10km)

The slant range channel, designated No. 1 in Figure 4-19, is basically the same as the extended range altimeter implementation discussed in Section 4.2; thus only the alterations required in this application are discussed here. The frequency tracker in this channel is somewhat different in detail although in its basic functional aspects it is identical. The primary difference is that the injected reference is eliminated due to the fact that the range of the PRF fundamental includes all useful injected reference offsets. A tracked L.O. is substituted for the tracked injected reference; it should be noted that this L.O. is ON-OFF modulated with the receiver gate as in the altimeter, however, it is not planned to correspondingly modulate the second L.O. The PRF tracker is implemented similar to that of the altimeter except that a higher and more convenient dither rate is selected; also, a lock-up circuit is added to hold the PRF at 4 mc for slant ranges of 19.0 m or less. Ranging below 19.0 m is achieved by adding a module to the PRF tracker similar to that used in STELATRAC; it operates as follows: In this module the second L.O. signal is chopped with the 4 mc low altitude gate and the resultant amplitude modulated signal is added to the eclipsed received signal as an injected reference at the preamplifier output. Then the carrier and sideband (fundamental of the 4 mc PRF) and the corresponding injected reference signals are each further amplified in separate i-f's. At each of these i-f outputs, the signal and injected reference outputs intermodulate at the detector to form a pair of second i-f signals at the injected reference offset frequency. These signals are further amplified in STELATRAC limiter-amplifiers. Subsequent phase comparison of the limiter-amplifier outputs yields the desired range information. This technique is used to insure the requisite calibration stability for 1 meter (3σ) accuracy. Laboratory evaluation of this technique with STELATRAC has shown that an accuracy of a few tenths of a meter is achievable.

The frequency trackers of channels 2 and 3 are simply implemented in the form of tracking filters at the respective receiver outputs. Essentially a STELATRAC receiver is used in each of the channels with

appropriate changes in the operating frequency and gains. The L.O. signal is provided by the slant range channel frequency tracker and the second L.O. is common to all three receivers. Since the first L.O. is derived in channel 1, the frequency trackers only track the doppler difference between beams. This enables the receiver and tracking loop to be narrowbanded, particularly the tracker, so as to make up for the generally reduced signal level and added noise in these channels.

Approximately 30 mw (peak) is the power transmitted in each of the three channels; orientation of the three beam axes in spacecraft coordinates is shown in Figure 4.20. The minimum power received (slant range axis at 45° incidence), using equation (39) in Section 4.2, and the same aperture and losses, is -112 dbm in the slant range channel and -116 dbm in either of the other channels. Receiver noise is estimated to be the same in each channel as in the altimeter except that the foldover loss is eliminated and channel 1 noise in the tracker bandwidth couples to channels 2 and 3 via the first L.O.

The analyses carried out in Section 4.2 for the extended range altimeter apply in general to the frequency trackers and to the slant range tracker in the PRF tracking mode and thus are not duplicated here. Operation of the ranging system in the low altitude mode can be understood from observing the phase shift dependence of the gating fundamental on the eclipsed pulse width W in the Fourier representation of the received signal:

$$f(t) = C_o + \sum_{1}^{\infty} \frac{2A}{\pi n} \left\{ \left[\sin \frac{\pi n W}{T} \right] \cos \left(\frac{2\pi n t}{T} - \phi_n \right) \right\} \qquad (133)$$

where

$$\phi_n = \frac{\pi n W}{T}$$

Performance in the low altitude mode can be assessed using STELATRAC results to which terrain scattering effects must be added. Terrain bias effects due to non-vertical incidence viewing for both the frequency tracker and the

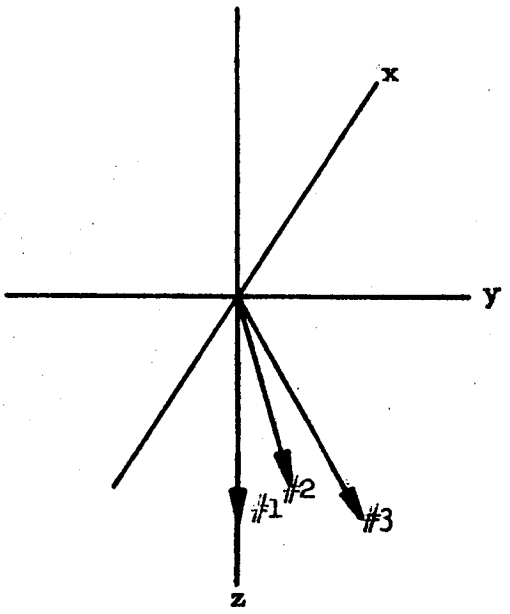

A) Beam Angles

Azimuth

$\beta_1 = \beta_2 = O,\ \beta_3 = 90^o$

Depression

$\gamma_1 = O,\ \gamma_2 = \gamma_3 = \gamma = 20^o$

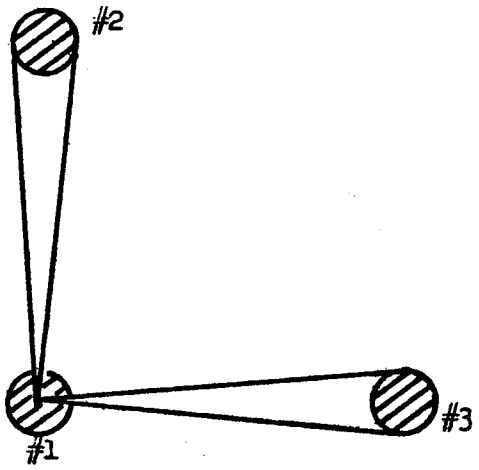

B) Plan View Showing Illuminated Areas

Figure 4-20 Beam Configuration, Slant Range Tracker and Velocity Meter

slant range tracker are covered in Sections 4.4.4 and 4.4.5.

The relations between the measurements of the velocity meter and the velocity components in vehicle coordinates are now derived. Let V_1, V_2, and V_3 be the measured vehicle velocities along the corresponding beam axis shown in Figure 4-20. These are related to the x, y, and z components of vehicle velocity according to

$$\begin{aligned} V_1 &= V_x \cos\beta_1 \sin\gamma_1 + V_y \sin\beta_1 \sin\gamma_1 + V_z \cos\gamma_1 \\ V_2 &= V_x \cos\beta_2 \sin\gamma_2 + V_y \sin\beta_2 \sin\gamma_2 + V_z \cos\gamma_2 \\ V_3 &= V_x \cos\beta_3 \sin\gamma_3 + V_y \sin\beta_3 \sin\gamma_3 + V_z \cos\gamma_3 \end{aligned} \tag{134}$$

Substituting for the angles listed in Figure 4-20, and solving for the x, y, z components of vehicle velocity in terms of the measured quantities, we have

$$\begin{aligned} V_x &= \frac{(V_2 - V_1) + V_1 (1 - \cos\gamma)}{\sin\gamma} \\ V_y &= \frac{(V_3 - V_1) + V_1 (1 - \cos\gamma)}{\sin\gamma} \\ V_z &= V_1 \end{aligned} \tag{135}$$

Consider now the propagation of system errors. For independent random errors in each of the measured velocities

$$\sigma^2_{V_\mu} = \sum_{k=1,2,3} \left(\frac{\partial V_\mu}{\partial V_k} \sigma_{V_k} \right)^2 \tag{136}$$

where μ = x, y, and z. Likewise, the variance of the errors in measured velocities due to the independent random errors in the various beam

pointing angles is given by

$$\sigma^2_{V_k} = \sum_{i=1,2,3} \left(\frac{\partial V_k}{\partial \beta_i} \sigma_{\beta_i} \right)^2 + \sum_{j=1,2,3} \left(\frac{\partial V_k}{\partial \gamma_j} \sigma_{\gamma_j} \right)^2 \tag{137}$$

Random errors in electronic measurements of the velocities along the beams combine in an RSS manner with respect to those given by (136). Evaluating the various partial derivatives needed in (136) and (137) and substituting, we have for the variances of the errors in velocities along the beam axis

$$\begin{aligned}
\sigma^2_{V_1} &= (V_x \sigma_{\gamma_1})^2 \\
\sigma^2_{V_2} &= (V_y \sin\gamma \sigma_{\beta_2})^2 + \left[(V_x \cos\gamma - V_z \sin\gamma) \sigma_{\gamma_2} \right]^2 \\
\sigma^2_{V_3} &= (V_x \sin\gamma \sigma_{\beta_3})^2 + \left[(V_y \cos\gamma - V_z \sin\gamma) \sigma_{\gamma_3} \right]^2
\end{aligned} \tag{138}$$

and for the variances of the velocity errors in vehicle coordinates,

$$\begin{aligned}
\sigma^2_{V_x} &= (\mathrm{ctn}\,\gamma \sigma_{V_1})^2 + (\csc\gamma \sigma_{V_2})^2 \\
\sigma^2_{V_y} &= (\mathrm{ctn}\,\gamma \sigma_{V_1})^2 + (\csc\gamma \sigma_{V_3})^2 \\
\sigma^2_{V_z} &= (\sigma_{V_1})^2
\end{aligned} \tag{139}$$

In order to provide numerical estimates of the performance capabilities of the various trackers in the velocity meter and ranging equipment, it is necessary to establish certain circuit and system parameters. Only those quantities needed in estimating errors are listed. Using the appropriate relations derived in Section 4.2 and the performance

requirements of 9 meters/sec^2 maximum vehicle acceleration, 550 meter/sec maximum velocity along the slant range axis, and 120 meters/sec maximum velocity in the lateral direction, these parameters are:

Slant Range Tracker	
Tracker natural resonant frequency	0.9 rad/sec
Effective bandwidth (one-sided) at maximum range of 10 km	0.48 cps
Error detector constant	1.7 volt/rad
Frequency Tracker, Slant Range Channel (1)	
Tracker natural resonant frequency	42 rad/sec
Effective bandwidth (one-sided)	22.3 cps
Loop gain	$\geq$10,000
Discriminator constant	$>$25 mv/cps
Frequency Trackers, Channel (2) and (3)	
Tracker natural resonant frequency	10 rad/sec
Effective bandwidth (one-sided)	5.3 cps
Loop gain	$\geq$1000
Discriminator constant	$>$25 mv/cps

For the purposes of estimating errors, it will be assumed that the angle between the velocity vector and any beam axis never exceeds 45°. In practice, the longitudinal axis will probably be held to within 10° of the direction of the velocity vector. Additional smoothing of the velocity meter data prior to use in the guidance computations is indicated. Smoothing times between 0.5 and 2 seconds are typical.

4.4 SLANT RANGE AND VELOCITY ERRORS DUE TO FINITE ANTENNA BEAMWIDTH

4.4.1 Introduction

When ranging or measuring the closing velocity to a point on the lunar surface, the finite beamwidth of the antenna will limit the measurement accuracy. Each point on the illuminated portion of the surface will have a distinct range and closing velocity to the vehicle. Due to the variation of scattering coefficient and range within the illuminated area, the amplitude returns will not be symmetrical about the center of the beam. The resultant non-symmetry of the amplitude vs. range distribution and the doppler velocity spectrum will cause errors in the measurements.

In this section of the report, the scattering properties of the lunar surface will be assessed and the effect of the variation in scattering coefficient will then be related to the specific geometry and the method of information extraction employed in the equipment.

4.4.2 Reflection Coefficient of the Lunar Surface at X-band

Because the lunar topology varies widely, from rugged mountain ranges to relatively flat crater floors and maria, mathematical expressions for the scattering coefficient of the surface will have to be assigned to a particular terrain or advanced as an average characteristic for a large area.

An average scattering coefficient at 8350 mc has been derived from the lunar scattering measurements made by J. V. Evans, with a portion of the West Ford Communications System. The scattering coefficient stemming from these measurements may be assumed to pertain to high altitude measurements where the area illuminated consists of several hundred square kilometers of varied terrain.*

A lunar landing will probably be made on either the maria or a large crater floor, therefore, a description of this type terrain is also necessary. Because presently available lunar reflection data cannot be resolved to the point where a reflection can be attributed to a specific small area of the moon, earth terrain measurements must be consulted as a guide to the scattering coefficient of specific surfaces and will be appropriate to this study.

*Needless to say, this is not typical for the sensors under study here as the diameter of the illuminated area does not exceed 1 km. However, it is included for completeness.

Scattering data is available for many types of earth terrain, including cultivated fields, pasture land, wooded areas, and deserts. Desert terrain was chosen as the closest approximation to the maria and crater floors of the moon. The available desert scattering data has been combined in this report to furnish a representative scattering coefficient.

The "scattering coefficient" or more precisely the "radar cross section per unit area" should be used in conjunction with the illuminated area as a radar cross section, i.e.:

$$\left|E_r\right|^2 = \frac{\sigma_{o(ave)} \cdot A \cdot \left|E_i\right|^2}{4\pi R^2} \qquad (140)$$

where

E_r	=	the electric field strength scattered by the surface and measured at the receiving antenna
$\sigma_{o\ (ave)}$	=	an average "scattering coefficient" for the surface illuminated
A	=	the area illuminated
E_i	=	the electric field strength incident on the surface
R	=	the distance from the radar antenna to the illuminated portion of the surface

A more explicit expression for the power returned to the radar by a differential surface area will be derived in a later section.

The most current lunar echo measurements have been made by J. V. Evans of Lincoln Laboratories. Evans made echo observations of the moon at 440 mc with the Millstone radar system and at 8350 mc with a portion of the West Ford Communication System located in Pleasanton, California.[8][9]

At optical frequencies, the moon appears uniformly bright, indicating the scattering is independent of incidence angle. At microwave frequencies, the moon has a bright spot at the moon's center. Evans found that the center appeared brighter at the lower frequency, 440 mc, indicating the surface becomes less diffusive as the frequency of observation is reduced. Only the 8350 mc data will be presented here consistent with our interest

(8)Evans,J.V.,"Radio Echo Observations of the Moon at 3.6-cm.Wavelength", Tech. Rpt. No. 256, Lincoln Lab., MIT, 19 Feb. 1962, ASTIA 274669.
(9) Evans,J.V.,"Radio Echo Observations of the Moon at 68-cm. Wavelength", Tech. Rpt. No. 272, Lincoln Lab., MIT, 22 June 1962.

in the X-band scattering characteristics appropriate to the sensors considered herein.

Evans' objective was to determine the scattering dependence on incidence angle and not the scattering coefficient as such. For our purpose, the data had to be graphically integrated and an absolute magnitude assigned. This magnitude was inherently less accurate due to the difficulty of system calibration.

The scattering coefficient obtained from Evans' data at 8350 mc is shown in Figure 4-21. The pulse to pulse fading observed was quite marked. The data was average over several thousand pulses to obtain a representative value for each data point. The pulse length of 30 micro-seconds was longer than would generally be used for altimetry and had the effect of reducing the peak of the curve, i.e., the scattering coefficient near normal incidence. Although the shape of the curve of scattering co-efficient vs. incidence angle is quite accurate, the absolute magnitude must be considered to have an accuracy of +400% and -50%.

The emperical expression for the scattering coefficient, $\sigma_o = .25 \exp(-5.2 \tan \theta) + .006 \cos \theta$, closely fits the experimental curve. It should represent the high altitude scattering coefficient, when the illuminated area consists of several hundred square kilometers of varied terrain.

If the illuminated area is exclusively a mare or crater floor, the scattering coefficient would be less diffusive than that for the lunar surface as a whole.

As mentioned earlier, desert terrain is considered the closest model for the maria and crater floors. Scattering data for desert terrain was available from two sources, the University of New Mexico and Goodyear Aircraft Corporation.

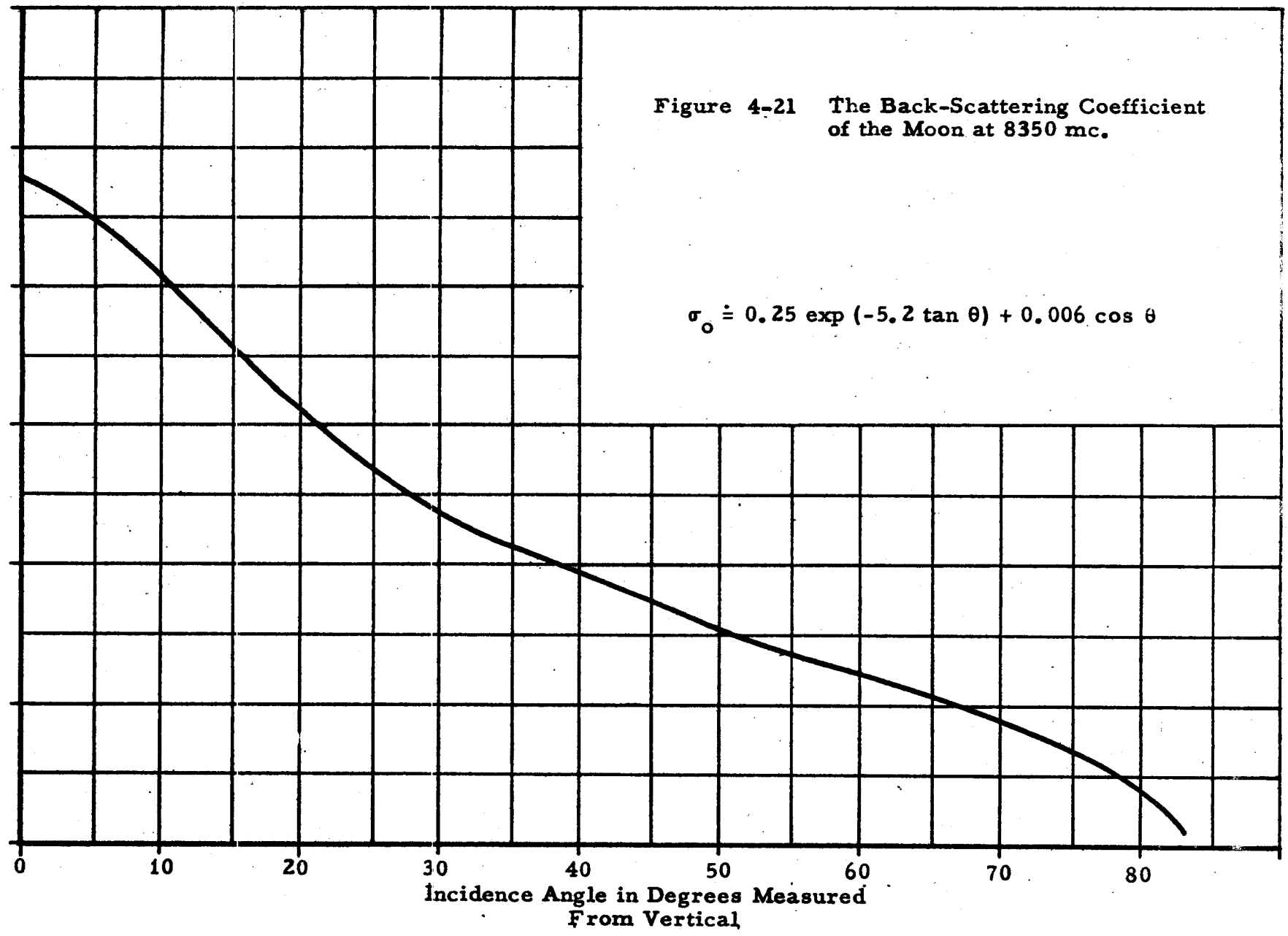

Figure 4-21 The Back-Scattering Coefficient of the Moon at 8350 mc.

The University of New Mexico made scattering measurements on various types of terrain at 415 and 3800 mc.[10][11] A short pulse, wide beam radar was used so that scattering characteristics could be measured for a wide range of incidence angles with a single pulse. The area scattering at any instant of time was an annular ring centered directly under the measuring aircraft. The polarity of the field incident on the terrain was a function of the azimuth angle and varied over the illuminated area from vertical to horizontal. The pulse to pulse fading was severe, with 90 percent of the returns falling in an 18 db range.

Data obtained for incidence angles between 10 and 20 degrees from vertical at 3800 mc is presented in Figure 4-22 as diamonds. The data at 3800 mc may be referenced to X-band (about 10,000 mc) if it is recognized that the data would apply to a surface with a physical roughness smaller than the roughness of the measured surface by the ratio of the reference wavelength to the measuring wavelength.

The Goodyear Aircraft Corporation made measurements of two desert areas at a frequency of 9375 mc.[12] A horizontally polarized 4-degree beamwidth antenna was used. One of the areas, located near Yuma, Arizona, was barren--almost devoid of vegetation, with low sandy hills. The other area near Amboy, California, was flat, with 10 to 15 percent vegetation coverage. The Yuma data appears in Figure 4-22 as circles, the Amboy data as crosses.

The emperical expression for the scattering coefficient, $\sigma_o = 2.2 \exp(-15\,\theta^2) + .01 \cos\theta$, best fits the experimental data. This should represent the scattering coefficient of the lunar surface when the illuminated area is exclusively a maria or crater floor.

---

(10)Edison, A.R., Moore,R.K., Warner,B.D.,"Radar Return at Near Vertical Incidence", Technical Report EE-24, University of New Mexico.

(11)Edison,A.R., Moore,R.K., Warner,B.D.,"Radar Return at Near Vertical Incidence", IRE Transactions on Antennas and Propagation, Vol. AP-8, No.3, May 1960.

(12)Goodyear Aircraft Corporation, "Radar Terrain Return Study". Report No. NOas 59-6186-C, 30 September 1959.

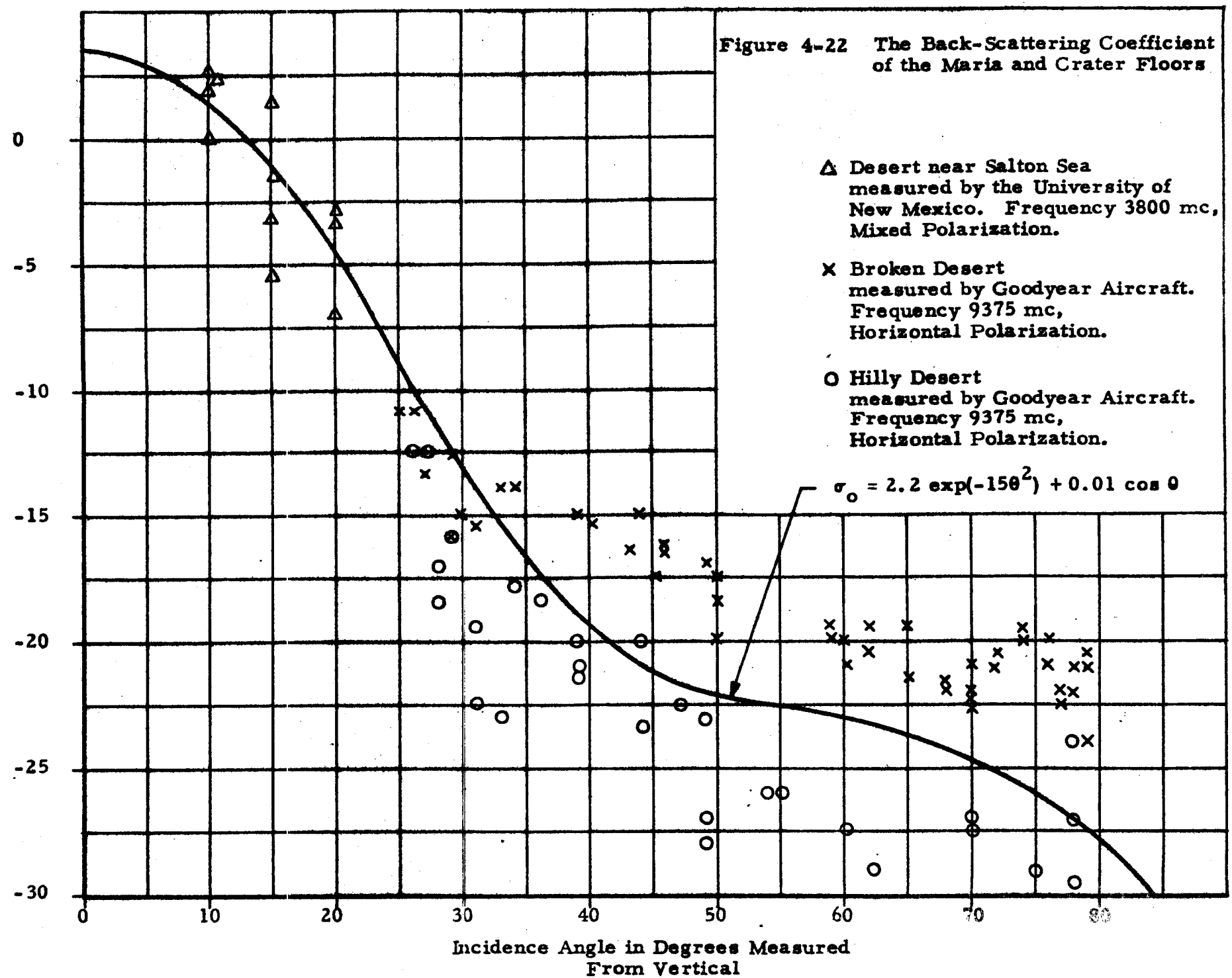
Figure 4-22 The Back-Scattering Coefficient of the Maria and Crater Floors
Δ Desert near Salton Sea measured by the University of New Mexico. Frequency 3800 mc, Mixed Polarization.
× Broken Desert measured by Goodyear Aircraft. Frequency 9375 mc, Horizontal Polarization.
O Hilly Desert measured by Goodyear Aircraft. Frequency 9375 mc, Horizontal Polarization.
$\sigma_o = 2.2 \exp(-15\theta^2) + 0.01 \cos\theta$
σ_o in db
0
-5
-10
-15
-20
-25
-30
0
10
20
30
40
50
60
70
80
Incidence Angle in Degrees Measured From Vertical

4.4.3 Power Returned to the Sensor

The power returned to the sensor by a differential area dA is given by:

Power Returned by Differential Area dA	=	Transmitter Power	x	Transmission Efficiency	x	Transmitting Antenna Gain Toward Differential Surface Area	x	Range Spreading	x
Scattering Coefficient	x	**Differential Area Cross Section**	x	**Range Spreading**	x	**Antenna Capture Area**	x	**Reception Efficiency**	(141)

Substituting symbols in equation (141):

$$P_r\Big|_{dA} = P_t \times K_t \times G_t(x,y) \times \frac{1}{4\pi R^2(x,y)} \times \sigma_o\left[\theta(x,y)\right] dA \times \frac{1}{4\pi R^2(x,y)}$$

$$\times \frac{G_r(x,y)\lambda^2}{4\pi} \times K_r \qquad (142)$$

where

P_t	=	transmitter power
K_t	=	transmitting system efficiency
$G_t(s,y)$	=	transmitting antenna gain toward surface element
$R(x,y)$	=	range to target
$\sigma_o\left[\theta(x,y)\right]$	=	radar cross section per unit area of surface, commonly called the surface scattering coefficient
dA	=	differential area on surface
$G_r(x,y)$	=	receiving antenna gain toward surface element
K_r	=	receiving system efficiency
θ	=	incidence angle measured from vertical

then:

$$P_r\Big|_{dA} = \frac{K_t K_r P_t \lambda^2}{64\pi^3} \frac{G_t(x,y)G_r(x,y)\ \sigma_o\ \theta(x,y)}{R^4(x,y)} dA \qquad (143)$$

For equal transmitting and receiving antenna gains

$$G_t(x,y) = G_r(x,y) = G(x,y) \tag{144}$$

and (143) becomes (after dropping the invariant constants)

$$P_r\Big|_{dA} \propto \frac{G^2(x,y)\ \sigma_o\left[\theta(x,y)\right]}{R^4(x,y)} \qquad dA \tag{145}$$

To find the power returned to the radar by any finite area, it is necessary to integrate equation (145). Because the integral is prohibitively involved for most practical cases, approximations will have to be made for the terms $G(x,y)$ and $\sigma_o\left[\theta(x,y)\right]$ in the integrand.

The exact form of $G(\psi)$, where ψ is the angle measured from the beam axis, is not known. As an approximation, $G(\psi)$ will be assumed to have the form of the gain function of a constant amplitude, constant phase, antenna aperture distribution. Then

$$G(\psi) = \left[\frac{\sin\left(\frac{\pi d}{\lambda}\sin\psi\right)}{\frac{\pi d}{\lambda}\sin\psi}\right]^2 \tag{146}$$

where

d = the antenna aperture diameter

λ = the radiated wavelength

The antennas anticipated for these missions have a d/λ of at least 14.5. Then equation (146) becomes

$$G(\psi) = \left[\frac{\sin\left(45.5\sin\psi\right)}{45.5\sin\psi}\right]^2 \tag{147}$$

Either the σ_o from the varied terrain of Figure 4-21, or the maria of Figure 4-22 may be used for the backscatter determination.

The maria σ_o will be used throughout the remainder of this discussion for three reasons:

(1) The maria covers a large portion of the moon's surface, and consequently would be encountered more often by an orbiting vehicle than the idealized average characteristic derived from direct lunar measurements from the earth.

(2) σ_o for the maria has a larger variation with incidence angle and consequently would give a larger ranging error from the non-symmetry about the antenna beam axis when the antenna is aimed at any angle other than vertical.

(3) The lunar landing would most likely occur on a mare or crater floor.

The scattering coefficient to be considered is then:

$$\sigma_o = 2.2 \exp(-15\theta^2) \tag{148}$$

The cos θ term has been dropped because it is of small relative importance.

Finally

$$R = h/\cos\theta$$

where h is the vehicle altitude.

Then equation (146) becomes

$$P_r\Big|_{dA} \propto \left[\frac{\sin(45.5 \sin\psi)}{45.5 \sin\psi}\right]^4 \times \exp(-15\theta^2) \times \cos^4\theta \; dA \tag{149}$$

where

ψ = the angle to the surface element dA from the beam axis

θ = the angle to the surface element from the vertical

The integration of equation (149) and its influence on the ranging and velocity sensing functions will now be determined.

4.4.4 Error in Range Measurement Due to Terrain

The slant range tracker determines the range to the surface by tracking the centroid of the return pulse. Any non-symmetry of the leading and trailing edges of the return pulse will be reflected as an error in the indicated range. The variation of the surface scattering coefficient and range within the illuminated area will cause the leading edge of the returned pulse to rise more steeply during its initial portion and the trailing edge to decay more steeply during its initial portion. The result is a shifting of the centroid of the return pulse toward a smaller range. The induced error is the difference between the apparent range and the actual range on the axis of the antenna beam.

The range tracker responds to the voltage rather than the power return. Restating equation (149) in terms of the voltage return:

$$V\Big|_{dA} \propto \sqrt{P_r}\Big|_{dA} \propto \left[\frac{\sin(45.5 \sin\psi)}{45.5 \sin\psi}\right]^2 \times \cos^2\theta \sqrt{\exp(-15\theta^2)} \quad dA \qquad (150$$

To find the power returned by a specific arc-shaped differential range segment, dr, equation (150) would have to be expressed in polar coordinates and integrated over the polar angle. The expression of the antenna gain function, involving ψ, would be prohibitively complex in this coordinate system. Therefore, as an approximation to the gain function averaged over a differential range segment, the gain function in the plane of incidence will be used.

The geometrical model chosen for the error analysis was an antenna with a 3-1/2 degree half-power beamwidth aimed at an angle 20 degrees from vertical. The solution procedure was to plot equation (150) taking dA to be the area of the differential range segment. Figure 4-23 shows the normalized square-root of the power returned as a function of the range referred to the range on the beam axis. Nonsymmetry of this curve would cause a ranging error. The graphical integration of Figure 4-23 yielded the shape of the leading and trailing edges of the return pulse, as shown in Figure 4-24.

The graphical integration of the area under the leading edge and the trailing edge of the pulse indicated that the indicated range would be 0.02 percent less than the actual range.

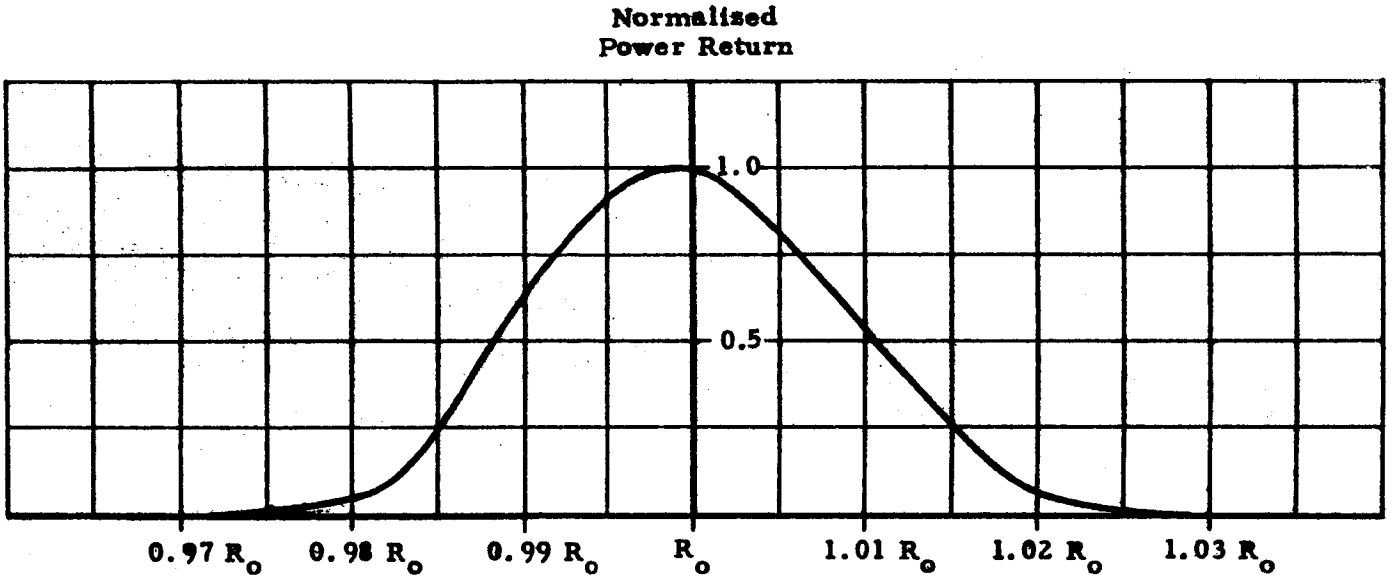

Figure 4-23. The Normalized Square-Root of the Power Returned vs Range Normalized to Range on Beam Axis (R_o)

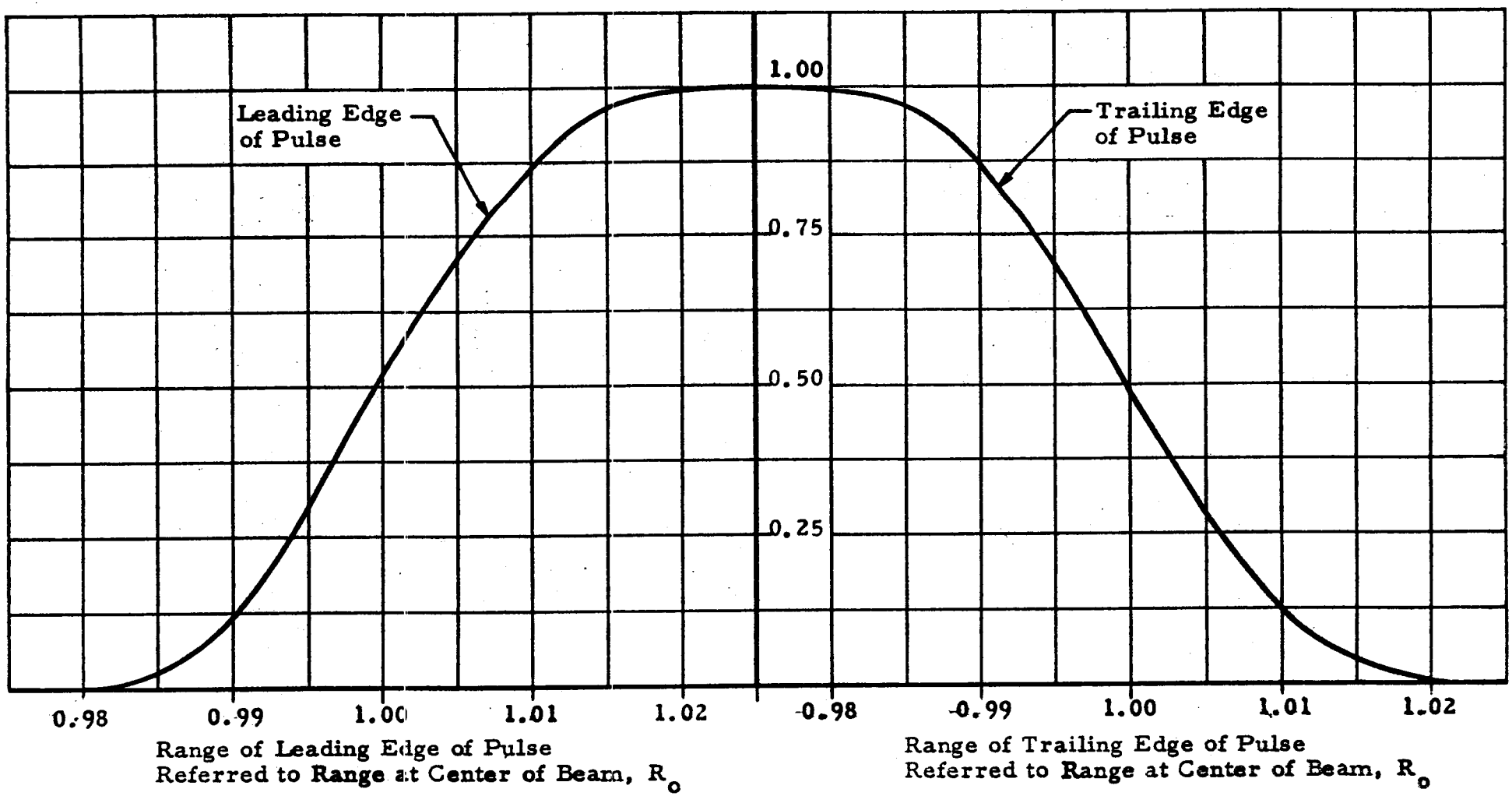

Figure 4-24. The Shape of the Leading and Trailing Edges of the Return Pulse

As the sidelobe returns were not included in the above analysis, an assessment of their effect upon ranging was made. The first sidelobes will influence the ranging results at lower altitudes where their doppler shift from the main beam will be small due to the low velocity so that they will be included within the tracking filter bandwidth. The sidelobes of the antenna (about 21 db below the main beam for a typical antenna design) were found to contribute a tracking error an order of magnitude smaller than the error induced by the dissymmetry of the main antenna lobe itself and can be neglected.

4.4.5 Doppler Velocity Sensor Terrain Induced Error

The doppler velocity sensor determines the closing rate to the surface by tracking the centroid of the doppler velocity spectrum. The shape of the spectrum varies widely depending upon beam orientation and the direction of the vehicle velocity. For this error estimate the antenna is assumed to point 20 degrees from the vertical and have a half-power beamwidth of $3\frac{1}{2}$ degrees. If the vehicle is traveling perpendicular to the beam pointing direction, the doppler spectrum will be widest, but will be almost symmetrical with a small resultant error in the indicated closing rate. If the vehicle is traveling in the same direction as the antenna is pointing, the spectrum will be narrowest, but will be entirely on the lower side of the doppler frequency return from the center of the beam axis. It is this case which has been chosen for analysis as it represents an extremum. Referring again to equation (150) :

$$V|_{dA} \propto \left[\frac{\sin(45.5 \sin\psi)}{45.5 \sin\psi}\right]^2 \cos^2\theta \sqrt{\exp(-150^2)} \quad dA \tag{150}$$

The doppler frequency shift of the return from a point on the surface is

$$F_d = \frac{2v}{\lambda} \cos\psi \tag{151}$$

Referring this frequency shift to the frequency shift, F_{do}, of the return on the antenna axis

$$\frac{F_{do} - F_d}{F_{do}} = \frac{\frac{2v}{\lambda}(1-\cos\psi)}{\frac{2v}{\lambda}} = 1 - \cos\psi \qquad (152)$$

The isodoppler contours are in the shape of elliptical rings centered about the beam axis. In equation (150), the product

$$\cos^2\theta \sqrt{\exp(-150^2)} \qquad (153)$$

was found to be linear within three percent over the extent of the half-power beamwidth. Therefore, these terms may be dropped in the integral as they will average to nearly a constant over each ellipically shaped ring. Then equation (150) reduces to

$$V_{dA} \propto \left[\frac{\sin(45.5\sin\psi)}{45.5\sin\psi}\right]^2 dA$$

Expressing dA in increments of doppler frequency

$$dA = \text{ring circumference x differential radius between scatterers yielding the doppler frequency, } f_d, \text{ and those yielding } f_d + \Delta f_d \qquad (154)$$

The circumference of the elliptical ring will be proportional to $\tan\psi$. From equation (151.)

$$f_d = \frac{2v}{\lambda}\cos\psi$$

and

$$d(f_d) = -\frac{2v}{\lambda}\sin\psi\, d\psi \qquad (155)$$

Defining ρ as the distance from the beam axis to the mean radius of the ring and R_o as the range to the surface along the beam axis

$$\rho = R_o \tan \psi \tag{156}$$

$$d\rho = R_o \sec^2 \psi \; d\psi \tag{157}$$

Using equation (155)

$$d\rho = \frac{-R_o}{\cos^2 \psi} \quad \frac{\lambda}{2v} \quad \frac{1}{\sin \psi} \quad d(f_d) \tag{158}$$

then

$$dA \propto \frac{1}{\cos^3 \psi} \quad d(f_d) \tag{159}$$

Finally

$$V\Big|_{d(f_d)} \propto \left[\frac{\sin (45.5 \sin \psi)}{45.5 \sin \psi}\right]^2 \quad \frac{1}{\cos^3 \psi} \quad d(f_d) \tag{160}$$

A graph of equation (160) is shown in Figure 4-25. The indicated closing velocity is seen to be .049 percent less than the actual closing velocity to the point on the surface intercepted by the antenna beam axis. This will be the largest error for any vehicle direction, with the beam aimed at 20 degrees from the vertical. The error induced in the doppler tracking network by the first antenna sidelobe was found to be an order of magnitude smaller than the error introduced by the main lobe assymmetry.

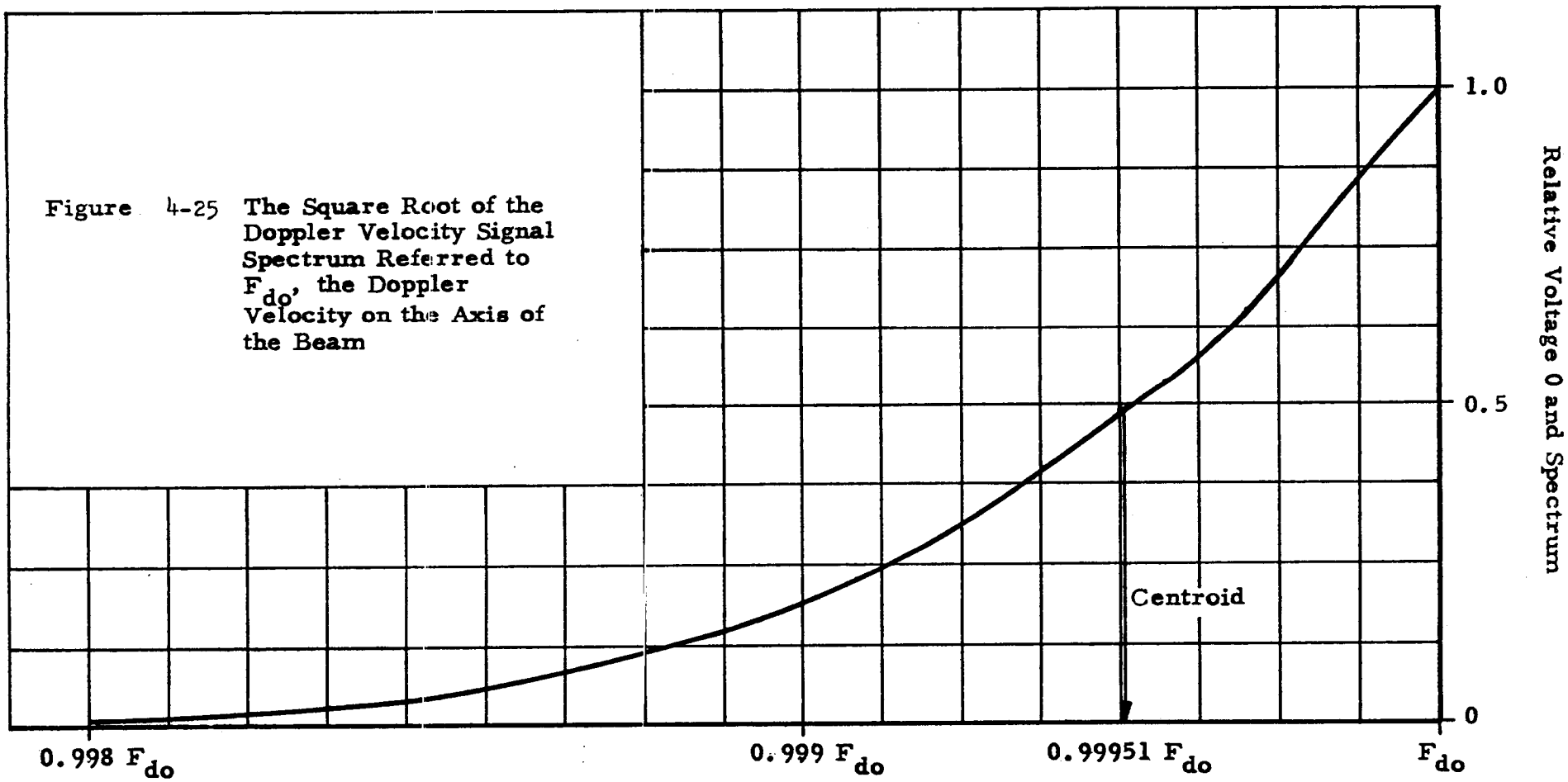

Figure 4-25 The Square Root of the Doppler Velocity Signal Spectrum Referred to F_{do}, the Doppler Velocity on the Axis of the Beam

5. EXPERIMENTAL PROGRAM

5.1 INTRODUCTION

An experimental program was carried out under the auspices of the Study to develop modules for use in the extended range altimeter, a critical sensor for all nonbeacon-assisted landings (see Figure 4-13 for a block diagram). The altimeter would be integrated with the STELATRAC beacon tracking radar, providing a composite sensor useful for spacecraft guidance at long and intermediate ranges. The experimental program was undertaken to isolate potential design problems, prove the circuits, fulfill the basic operational objectives, and confirm the system analysis to the extent possible within the Study scope. The experimental program should be continued to provide an operating feasibility model of the altimeter and an altitude and altitude rate simulator for static and dynamic testing and evaluation purposes. The simulator consists primarily of standard unmodified laboratory test equipment and would be used to simulate terrain spread spectrum return, evaluate effects of flight dynamics upon receiver tracking behavior, and determine sensor accuracy and threshold performance.

Only the core of the extended range altimeter system was instrumented. The peripheral subsystems such as the power supply (or power converter), antenna, and data processing equipment were not implemented. These subsystems, although not completely functionally independent, are sufficiently divorced from the essential altimeter circuitry so that accurate test data could be obtained in the future with available laboratory instrumentation. On the basis of program economy, the companion subsystems are not warranted initially.

Each of the modules that have been developed for the altimeter are packaged in a brassboard configuration. It is believed that this form of packaging offers some of the electrical advantages of flight packaged units such as isolation from electrical interference without restricting any circuitry modifications necessitated during subsequent subsystem tests. In addition, brassboard packaging can be accomplished in the laboratory economically and within a constricted time schedule. This type of packaging was successfully used during the STELATRAC rendezvous radar feasibility studies. Photographs of the packaged modules are shown in the sections where each module is discussed.

Many of the modules required for the implementation of the feasibility model of the altimeter were developed previously for the STELATRAC rendezvous radar project and, where practical, would be incorporated in the altimeter. The following list, Table 5-1, illustrates the modules that require development specifically for the extended range altimeter. Secondly, the list indicates the number of modules potentially interchangeable between the extended range altimeter and the STELATRAC rendezvous radar. Such a characteristic is useful for logistic and spare parts purposes.

Table 5-1. Module Availability

Modules to be Developed Specifically for Altimeter	Modules Previously Developed for STELATRAC Usage
AGC'd Amplifier	Directional Coupler, 20 db
Frequency Discriminator*	Orthomode Mixer
PRF Generator*	IF Preamplifier
AGC'd Bandpass Amplifier	IF Amplifier & Detector
Synchronous Demodulator*	Limiter-Amplifier
Dither Oscillator	D-C Amplifier (2 each)
	Low Power X-Band Source
	High Power X-Band Source
	65 MC Oscillator
	Balanced Modulator

Altitude and altitude rate simulation equipment would be required to accurately and dynamically test the system functions of the feasibility demonstration model. Functionally, it would receive the transmitted signal, delay it for a time corresponding to 2 h/c, degrade the pulse shape as programmed, add an appropriate noise disturbance, and retransmit the signal. The time delay would be realized by a delay line that could be adjusted to represent a varying altitude. The parameters such as signal amplitude, noise level, and pulse shape degradation would be controllable to provide a capability for completely exercising the sensor.

*These modules were developed during the conduct of the present Study.

5.2 PRF GENERATOR

5.2.1 Introduction

A PRF generator is used in the altimeter to alternately gate the transmitter and receiver multiplier chains and to provide a 30 cps jitter signal for altitude error sense determination. Isolation between the transmitter and receiver is obtained by time sharing the antenna, i.e., turning the receiver OFF when the transmitter is ON and turning the transmitter OFF when the receiver is ON. The gating signals are applied directly to the varactor bias points of each of the X-16 frequency multipliers, thereby effecting total turn-off of their respective signals.

The dither signal is employed to sense the PRF error and control the pulse repetition frequency to match the two-way propagation time to the half-period of the modulation waveform. The dither is imposed on the transmitter signal, the local oscillator signal, and the injected reference signal by the PRF generator and is subsequently detected by the synchronous demodulator in the altitude tracker section of the altimeter. Thus information from the synchronous demodulator controls the pulse repetition frequency so as to maximize the gated return energy.

Because of the system accuracy considerations, fast rise and decay times are required for the gate pulses. In addition, a slight delay--about 30 nanoseconds--is required between the turn-off of the transmitter gate pulse and the turn-on of the receiver gate pulse and vice versa. The time lag prevents the receiver from receiving a direct-coupled signal from the transmitter, which would cause saturation. If saturation were permitted to occur in the narrowband portion of the receiver, the receiver would be desensitized for relatively long time periods due to its long recovery time.

5.2.2 Circuit Description

The PRF generator, in addition to providing the capabilities mentioned above, must exhibit a reasonably linear frequency versus control voltage characteristic for proper closed loop operation. This requirement, plus the

relatively extensive frequency sweep requirement, 340 cps to 42 kc, suggests a circuit utilizing two oscillators, one being voltage-controlled. The output signals are heterodyned to produce the desired pulse repetition frequency. The individual oscillator frequencies are much greater than the PRF range leading to a narrow (percentage-wise) frequency deviation specification for the VCO. As a result, a linear frequency versus control voltage characteristic can be realized via simple circuitry.

A block diagram of the PRF generator (with pertinent waveforms included) developed for the altimeter circuit study is shown in Figure 5-1. The two oscillators consist of a highly stable, low phase noise, crystal oscillator, and an L-C VCO, operating at nominal frequencies of 1.0 mc and 1.021 mc, respectively. The L-C VCO output signal frequency can be controlled over a frequency range from 1.0 mc to 1.042 mc to provide the required PRF range. The crystal oscillator can be frequency modulated at a 30 cps rate with a variable frequency deviation to provide the required dither signal over the design range of altitudes.

The two oscillator signals are heterodyned and filtered to produce a dithered signal to drive the Schmitt trigger, where it is squared. Following shaping, it is differentiated to produce the timing pulses, as shown in the block diagram. The timing pulses trigger the logic circuit which in turn generates the two gating pulse trains--one gates the transmitter and the second, shifted 180 degrees in phase, gates the receiver. The logic circuit consists of two flip-flops and "AND" and "OR" gates, and output emitter followers. Provision for controlling the amplitude of each gate pulse is included in the logic circuit.

A photograph of the brassboard model of the PRF generator is shown in Figure 5-2.

5.2.3 Test Results

The electrical characteristics of the developed PRF generator satisfied the above design objectives. The generated pulse repetition frequency was linear with respect to the control voltage within 15 percent. The output pulses,

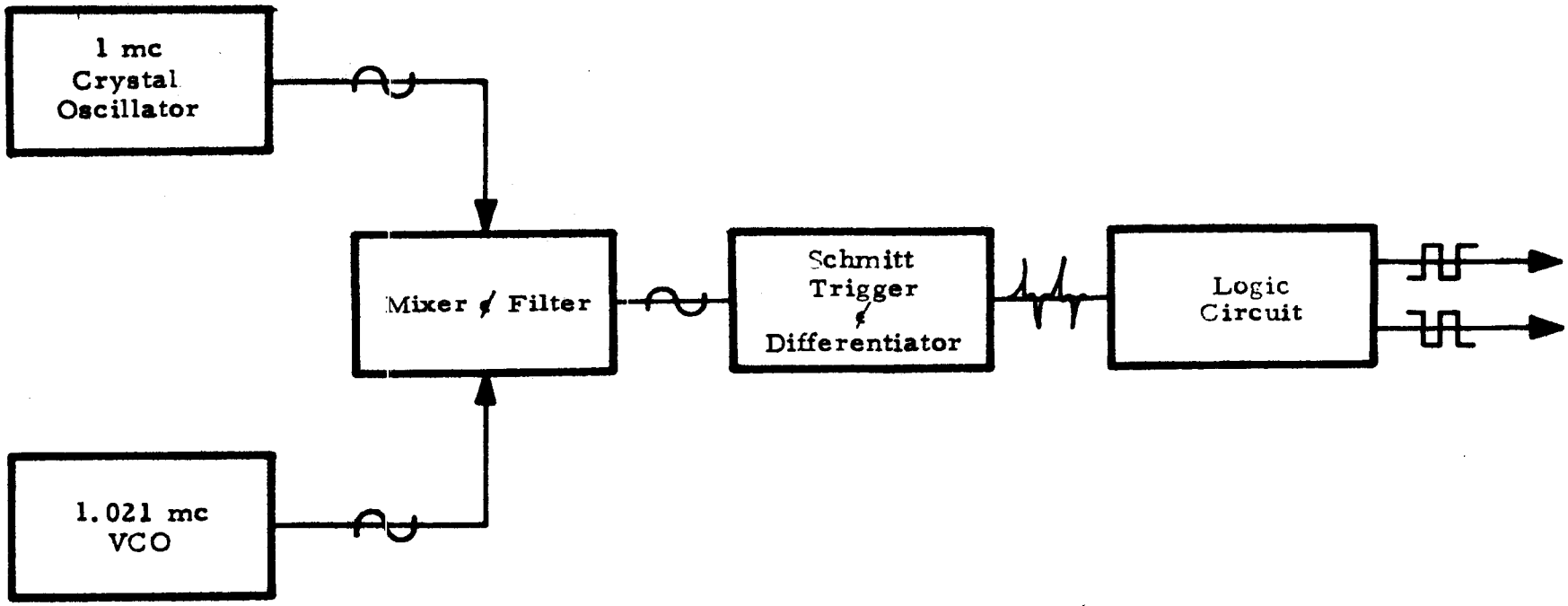

Figure 5-1 Block Diagram - PRF Generator

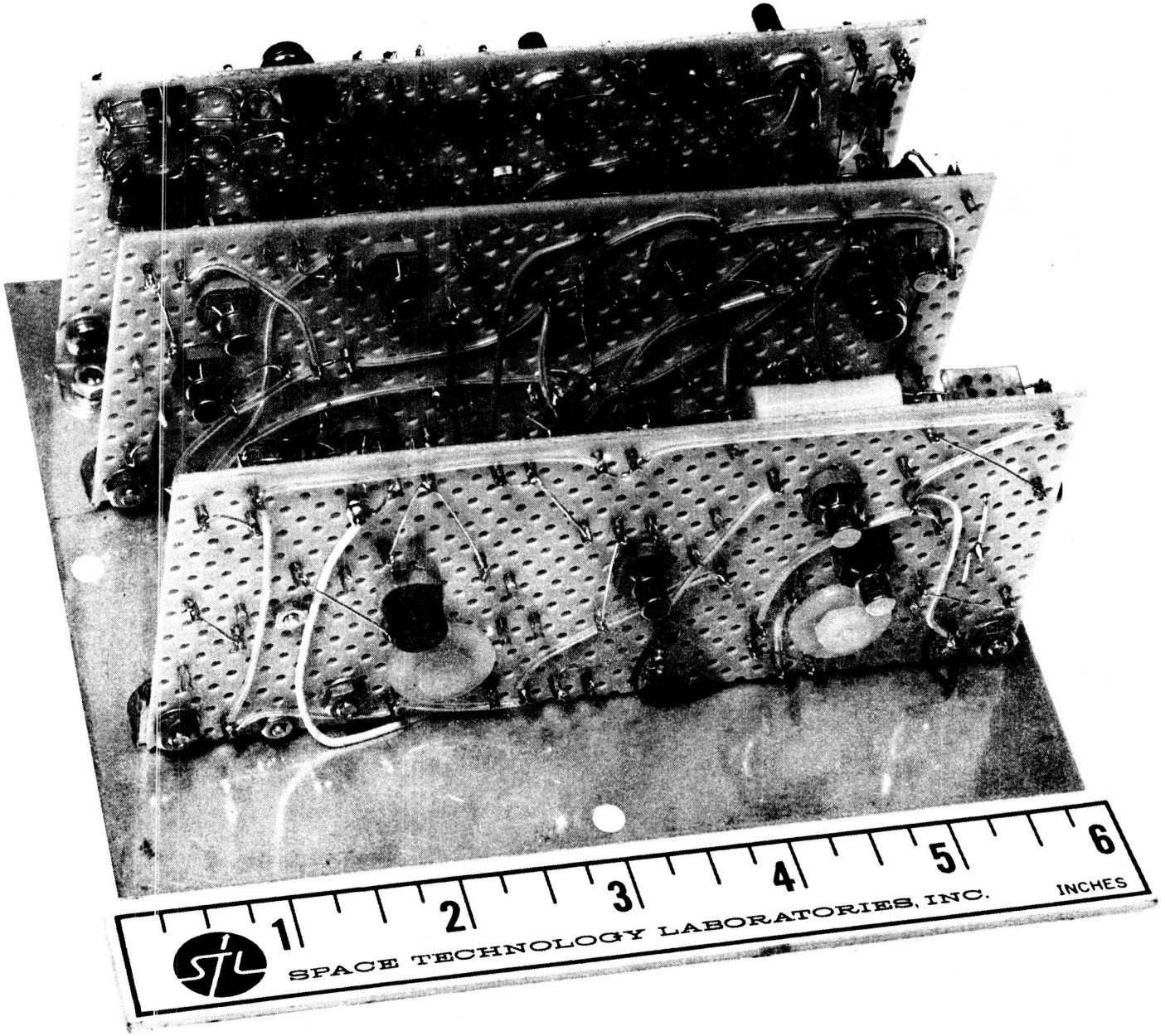

Figure 5-2. Brassboard Model - PRF Generator

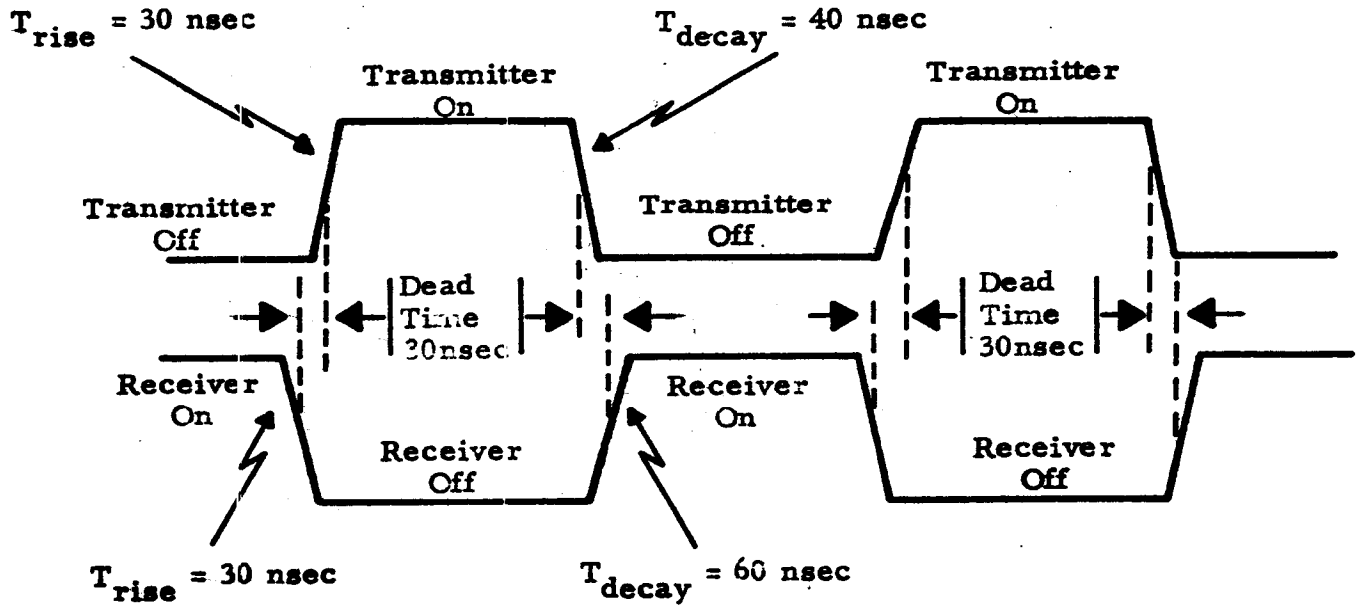

Figure 5-3 Output Gate Pulse Shapes

Figure 5-3, had a rise time less than 30 nanoseconds over the entire operating frequency range, negligible droop, satisfactory decay time, and the specified dead time.

5.3 SYNCHRONOUS DEMODULATOR

5.3.1 Introduction

The amplitude of the 30 cps error signal from the altitude tracking loop amplitude detector is proportional to the magnitude of the altitude tracking error. The phase of the 30 cps receiver signal, relative to the dither oscillator signal, is either 0 or 180 degrees, depending on the sense of the error signal, i.e., whether the PRF is too high or too low. The magnitude and sense of the error signal is translated to a d-c voltage by a synchronous demodulator whose reference is obtained from the dither oscillator. The synchronous demodulator is described in this section.

5.3.2 Circuit Description

A schematic of the synchronous demodulator is given in Figure 5-4. It uses two diode bridge gates connected in parallel. A reference signal, furnished by the dither oscillator and applied in push-pull to the bridges through series diodes, is used as the gating signal. The 30 cps receiver signal to be detected is fed to the center taps of the diode bridges. With no reference signal present, the diodes of the bridges are conducting and the instantaneous voltage level of the 30 cps receiver signal appears across the 4.7 k demodulator load resistor. With the reference signal present (normal operating conditions), the diodes of the bridges are switched OFF and ON by the reference signal waveform, thus gating the 30 cps receiver signal ON and OFF at the demodulator output.

In order to ensure good switching action, the dither reference signal is first passed through the limiter-amplifiers Q_1 and Q_2. Low source impedance for the push-pull driver is provided by the two emitter followers Q_4 and Q_5. The reference signal applied to Q_4 must be inverted from that applied to Q_5 and is accomplished by the inverter amplifier Q_3. D-C coupling of the bridge to the emitter followers Q_4 and Q_5 ensures preservation of the square waveform of the reference signal and good switching action.

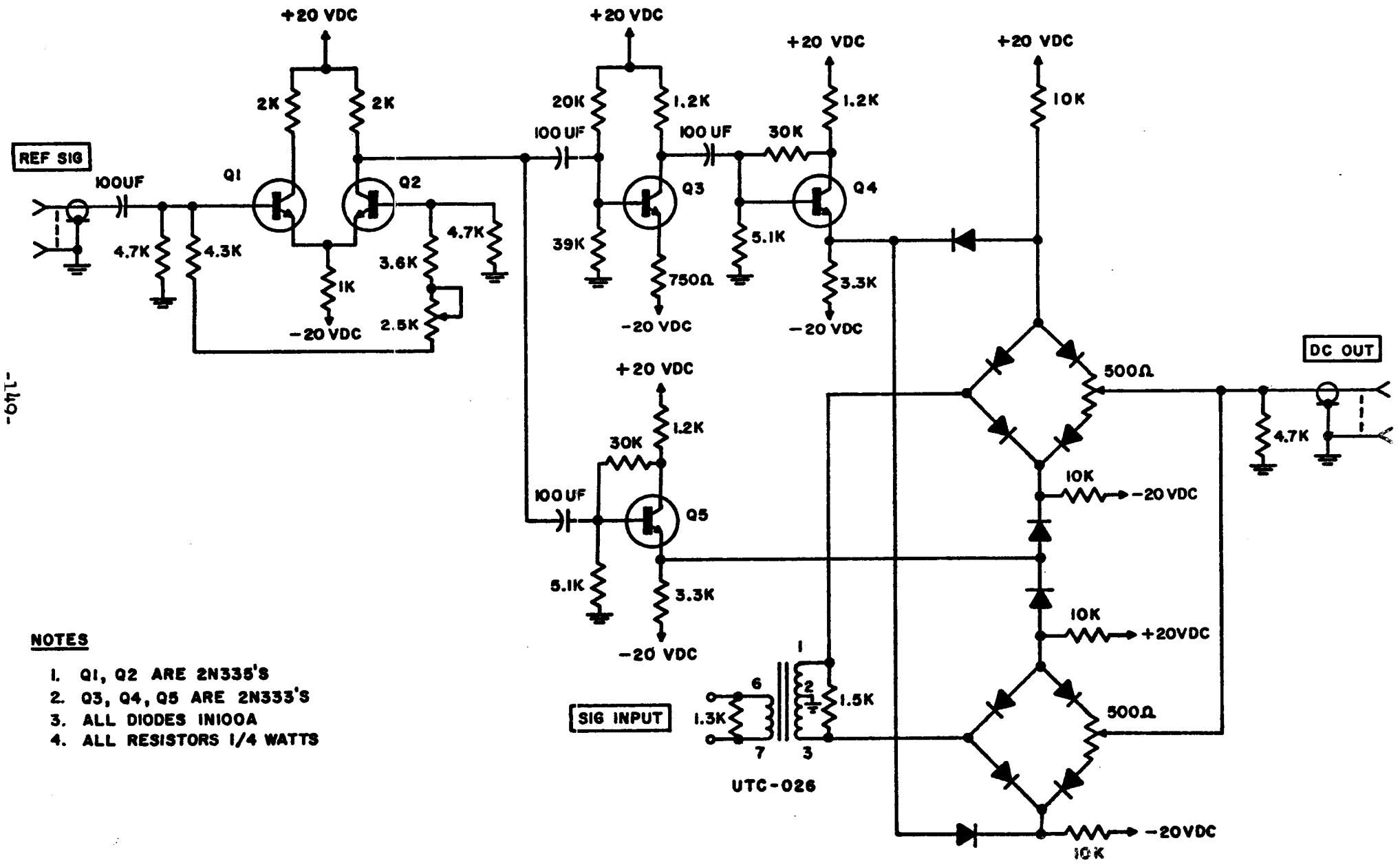

NOTES

1. Q1, Q2 ARE 2N335'S
2. Q3, Q4, Q5 ARE 2N333'S
3. ALL DIODES IN100A
4. ALL RESISTORS 1/4 WATTS

Figure 5-4 30 Cycle Synchronous Demodulator

5.3.3 Test Results

The brassboard model of the synchronous demodulator shown in Figure 5-5 provides adequate voltage sensitivity for the altitude tracking loop. Table 5-2 is a tabulation of the 30 cps receiver input level versus the d-c output voltage. Column 3 of the table illustrates the very low sensitivity of the demodulator to the second harmonic of the receiver signal. The drift of the null point of the bridge output was negligible, being of the order of 2 mv.

Table 5-2. Synchronous Demodulator Sensitivity (30 cps Dither Frequency)

E_{in} (across primary)	E_{out} (at bridge)	Sensitivity to 60 Cycles
0.5 v p/p	+50 mv d-c -53 mv d-c	0
1.0 v p/p	+100 mv d-c -100 mv d-c	0
1.5 v p/p	+155 mv d-c -155 mv d-c	0
2.0 v p/p	+210 mv d-c -210 mv d-c	1.0 mv d-c approx.
2.5 v p/p	+260 mv d-c -260 mv d-c	2.0 mv d-c approx.
3.0 v p/p	+310 mv d-c -310 mv d-c	3.0 mv d-c approx.
15.0 v p/p	+1.55 v d-c -1.55 v d-c (no indication of clipping)	

5.4 FREQUENCY DISCRIMINATOR

5.4.1 Introduction

The accuracy of the frequency determination in the frequency tracking loop is a direct function of the stability of the frequency discriminator. An appreciation of the discriminator requirements can be derived from the following example. For a descent rate of 0.3 m/sec, the doppler shift is 20 cps at X-band. As the frequency measurement is performed at the second i-f of 500 kc, an allowable drift of 0.3 m/sec in the reference output position corresponds to a stability factor of 1 part in 25,000.

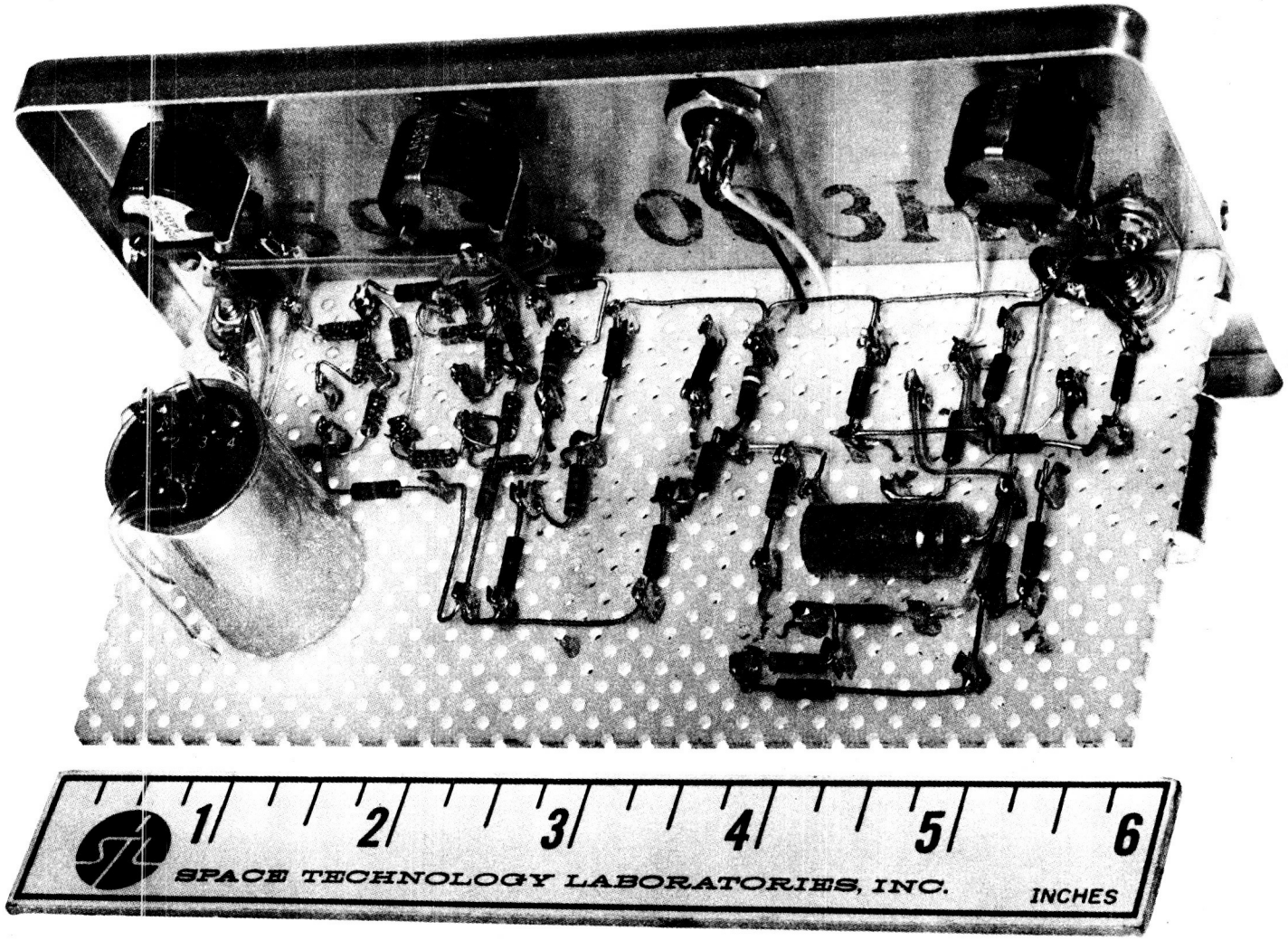

Figure 5-5. Brassboard Model Synchronous Demodulator

The generic types of circuits available for frequency discriminators include those employing passive frequency sensitive circuits, crystal discriminators, and those utilizing a stable signal source as a reference. The best drift stability factor that can be obtained with a passive L-C type of discriminator, the simplest configuration circuitwise, is about 1 part in 1,000. This value falls short of the system requirements.

Crystal discriminators are capable of providing drift stabilities in excess of 1 part in 25,000; however, the bandwidth associated with this type of discriminator is insufficient.

The discriminator configuration satisfying both the drift stability and the bandwidth specification employs a stable reference signal for sensing frequency error. Circuitry utilizing this technique can be readily developed in simple form, ensuring reliability and low power consumption. Its drift stability can be made that of the reference signal frequency--up to 1 part in 10^8 if necessary.

5.4.2 Circuit Description

A block diagram of the stable reference frequency discriminator investigated for use in the altimeter is shown in Figure 5-6. A positive d-c signal is available if the frequency of the unknown signal is greater than that of the reference signal, and a negative d-c signal if the unknown signal frequency is less than the reference. The d-c signal level is fixed, either positively or negatively, and is independent of the amount of difference between the reference and unknown signals.

The basic circuit operation can be explained by assuming the reference signal is given by

$$E_R = E_o \cos \omega_o t$$

and the unknown signal is

$$E_U = K E_o \cos \left[(\omega_o \pm \omega_d) t + \phi \right]$$

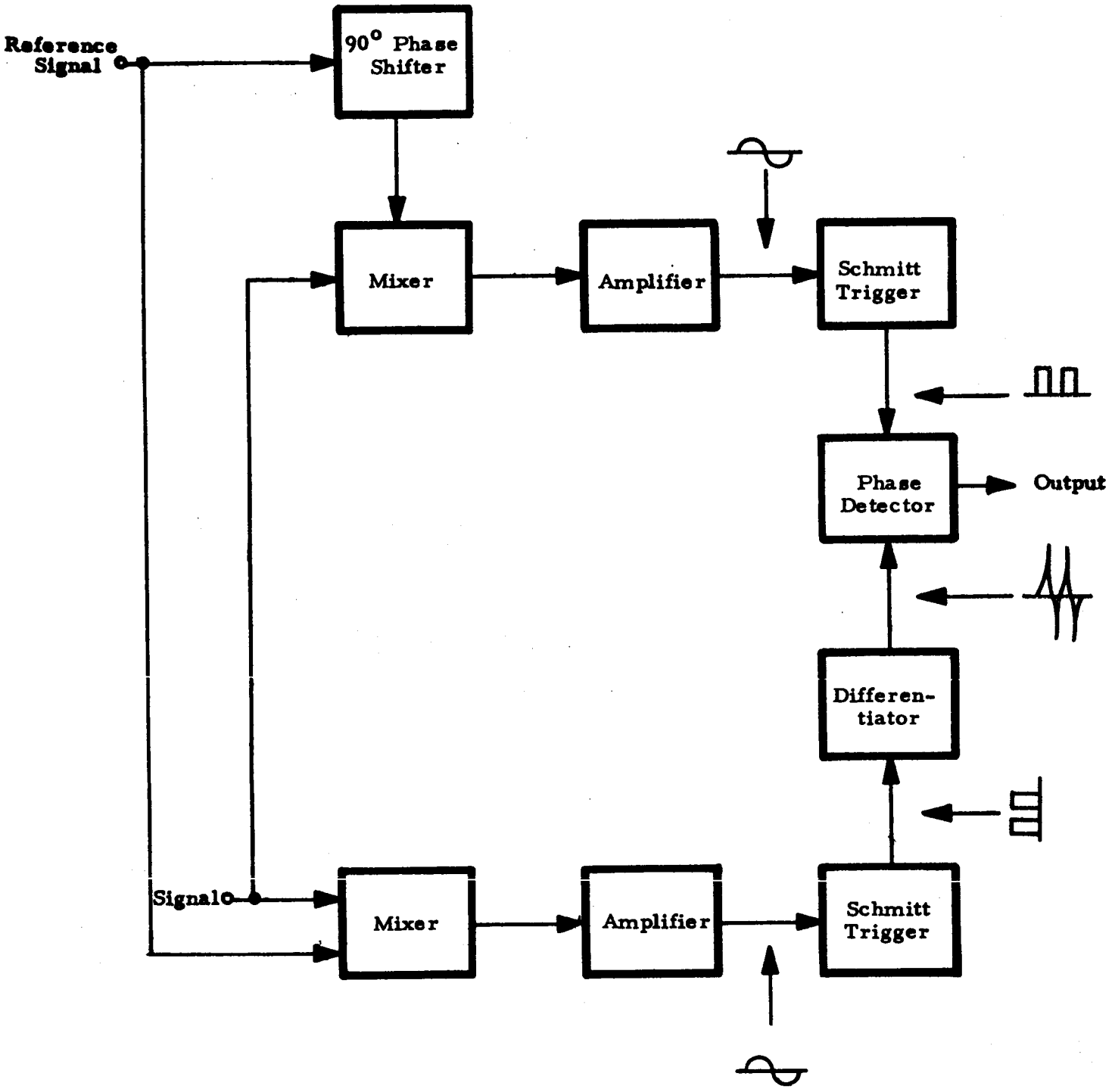

Figure 5-6 Block Diagram of Frequency Discriminator

where

E_o = amplitude of reference signal

$K E_o$ = amplitude of unknown signal

ω_o = reference signal angular frequency

ω_d = difference in angular frequencies of the reference and unknown signals

ϕ = a constant phase shift

In the "unknown signal" channel, a part of the unknown signal and a part of the reference signal are mixed to give an i-f of

$$E_A = K_2 E_o \cos (\pm \omega_d t \pm \phi)$$

In the other channel, the two signals are also mixed subsequent to the introduction of a 90-degree phase shift in the reference signal, giving an i-f of

$$E_B = K_2 E_o \cos (\pm \omega_d t \pm \phi + \pi/2)$$

If the unknown signal frequency is greater than the reference signal frequency, the two i-f's are

$$E_A(+) = K_2 E_o \cos (\omega_d t + \phi)$$

$$E_B(+) = K_2 E_o \cos (\omega_d t + \phi + \pi/2)$$

Conversely, if the unknown signal frequency is less than that of the reference signal, the i-f's are

$$E_A(-) = K_2 E_o \cos (\omega_d t + \phi)$$

$$E_B(-) = K_2 E_o \cos (\omega_d t + \phi - \pi/2)$$

The 90-degree lead or lag condition of E_A, with respect to E_B, thus determines whether the unknown frequency is greater or less than the reference signal frequency.

The technique employed for determining the phase of E_A, with respect to E_B, consists of amplifying the i-f signal, squaring the wave shape of the two signals by means of triggers, and then differentiating the squared signal in the "unknown signal" channel. (The waveshapes existing at various points in the

circuitry are shown in Figure 5-6.) The two signals are then compared in a phase detector circuit, giving a positive d-c output signal if the positive impulse and the squarewave are in phase and a negative d-c output if the positive impulse and the squared wave are out of phase. The phase detector circuit consists of a gate, a backlash circuit, and another Schmitt trigger, and provides either a positive or a negative signal output, depending on the relative lead-lag signal conditions.

5.4.3 Test Results

A breadboard model of the frequency discriminator circuit was built and operated in the frequency controlled loop shown in block diagram form in Figure 5-7. This loop, although not identical to that of the altimeter system, is functionally similar and hence capable of providing an evaluation of the frequency discriminator characteristics.

During operation, the amount of frequency deviation (overshoot) of the 4.0 mc VCO about its mean was controllable by the element values of the integrating circuit and the sensitivity of the frequency discriminator. The operation of the circuit continued to be satisfactory when the frequency of the reference signal was adjusted to $\pm$14 kc from its mean value. The operation of the circuit in the presence of noise was not evaluated; however, no major problems are expected in this area.

5.5 X-BAND POWER SOURCE

5.5.1 Introduction

Frequency multiplication can be achieved via a large number of different devices, e.g., vacuum tubes, ferrites, semiconductor diodes, etc. The basic requirement in each case is that the device exhibit nonlinearities in its operating characteristic.

There is appreciable interest currently in varactor multipliers because 1) they provide highly efficient frequency conversion, 2) varactors are passive devices requiring at most the application of an external d-c bias voltage, 3) they operate over a wide frequency range--from less than 1.0 mc to frequencies

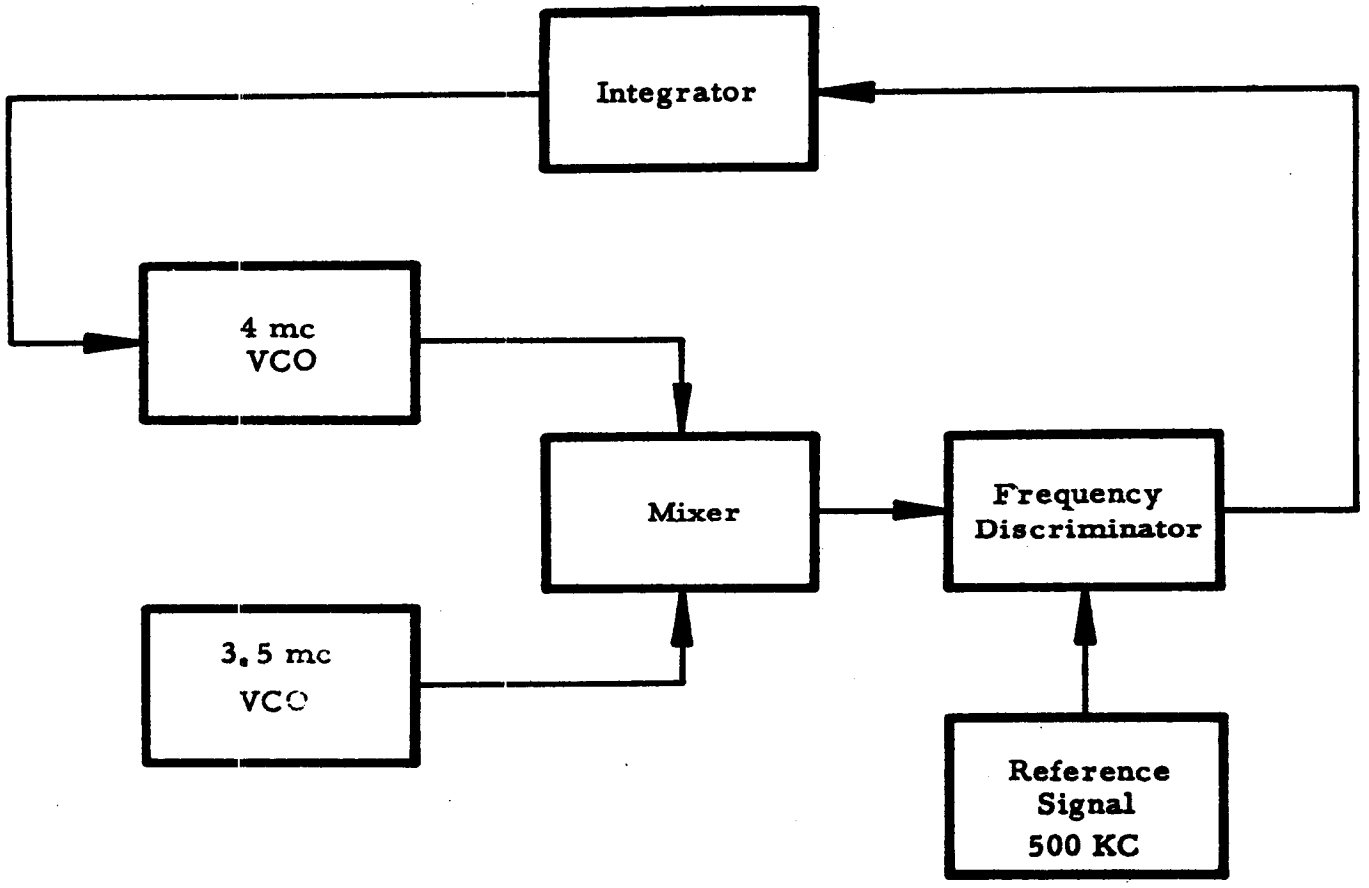

Figure 5-7 Frequency Discriminator Test Setup

in excess of K-band, and 4) they require relatively simple external circuitry for proper operation. Manley and Rowe showed that 100 percent efficient frequency multiplication is theoretically achievable with lossless nonlinear reactances and associated circuitry. In practice, the varactor and external circuitry is not lossless, although the latter approaches 90 to 95 percent efficiency if low loss circuits of the coaxial or waveguide type are utilized.

The efficiency of the multiplier is intimately related to the Q of its varactor. For microwave operation, loss in the varactor diode is normally much greater than external circuit losses, therefore varactors with high Q's are essential if multipliers are to be used as efficient power sources.

The power handling capability also depends on the capabilities of the varactor. The maximum applicable peak input power is limited by the diode reverse breakdown voltage characteristic and the average power rating depends on the power dissipation factor of the diode.

Variation of the varactor bias affords a ready means for switching or gating the output power. In addition, the bias can be adjusted to compensate for deleterious temperature effects. The design and performance features of the X-band power source are described in the following portions of this section.

5.5.2 Circuit Description

The design of the X-band power source, a unit of which was delivered to MSFC in partial fulfillment of the requirements of this contract, is unique in that it emphasizes maximum operational stability, efficiency, and reliability in a space environment, while minimizing size and weight (see Figure 5-8). Each doubler consists of completely enclosed input and output coaxial cavities coupled by a varactor connected in shunt (across the E-field). The shunt mounting provides an effective heat sink to the metallic cavity walls for one end of the varactor, minimizing local hot spots. Self-biasing is incorporated in the first three doublers and external biasing in the last doubler.

The electrical length of the cavities is an odd multiple of a quarter wavelength, the exact multiple determined by size considerations. Vernier tuning is accomplished by varying the penetration depth of a screw-driven plunger contained within the center conductor, which varies the circuit capacitance.

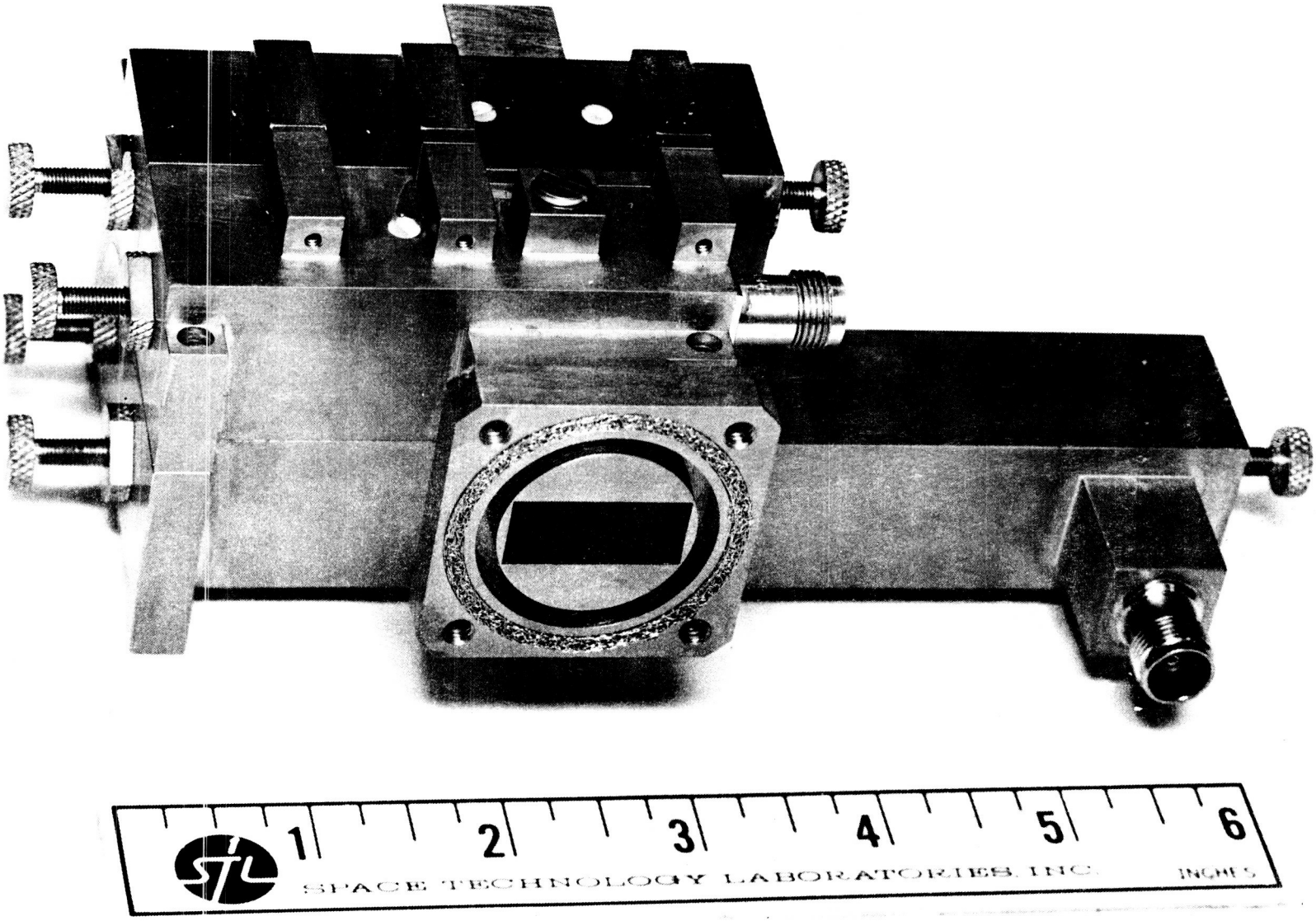

Figure 5-8. X-Band Power Source

The output cavity of one doubler and the input cavity of the succeeding doubler are identical so that coupling mismatch is minimized. Direct coupling between units is employed because it provides better conversion efficiency than either loop or probe coupling. Impedance transformations to intermediate impedance levels such as to a 50-ohm interconnecting coaxial line are avoided, improving operating efficiencies.

The last doubler stage is modified from the standard coaxial form, since the output terminal is X-band waveguide. It features a coax-to-X-band waveguide transition and is constructed so that squarewave or pulse modulation may be applied to its varactor diode. The diode coupling assembly is insulated from the waveguide with dielectric tape to provide d-c isolation and an r-f bypass.

For weight reduction, aluminum with electroless nickel plating is employed. The dielectric material is Rexolite and the connectors are aluminum with irradiated polyolefin dielectric. The end plates are cemented in place with conductive epoxy after electrical testing. All diodes are mounted in fine wire mesh "fuzz buttons" to provide shock mounting and to ensure good electrical contact. Formed gaskets of the same material are used between units to minimize r-f leakage.

The design of the X-band power source is such that each of the four doublers are normally integrated into a single package; however, each doubler may be operated individually to facilitate tuning during the initial assembly phase. This design feature shortens test time by permitting individual cavity tuning and adjustments without incurring interferring reactions from the other doublers. Subsequent to testing each doubler, the units are successively integrated, starting with the lowest two frequency units. After the addition of each unit, the power output is measured and the output signal spectrum can be analyzed to ensure low spurious content.

5.5.3 Test Results

In discussing the data which was taken on the individual doublers and the complete chains, it is convenient to number the doublers--1, 2, 3, and 4--designating the lowest frequency doubler as "1" and the highest as "4".

The conversion losses obtained with the doublers singly and in various combinations are tabulated in Table 5-3. Output power was measured by matching into a 50-ohm detector.

Table 5-3. Conversion Loss of Multiplier

Doubler Configuration	Output Power (dbm)	Conversion Loss (db)	Input Power (dbm)
1	30.8	2.2	+33
1, 2	28.3	4.7	+33
1, 2, 3	24.5	8.5	+33
1, 2, 3, 4	20.2	12.8	+33

The output spectrum was viewed at the output of each doubler and combination of doublers, both with and without filtering, In all cases, spurious signals were greater than 35 db below the desired signal.

The output power was 110 milliwatts for an input power level of 2 watts. If the input power level is varied appreciably from 2 watts, the input and output impedance matching tuners should again be retuned to obtain maximum efficiency. This is necessary because the multiplier input and output impedances are dependent on drive level.

6. SENSOR ERROR ESTIMATES

6.1 BEACON ASSISTED DESCENT

The error estimates are predicated upon the specifications of Section 3 and the subsystems described in Section 4. The errors are evaluated at the specification limits although in many instances, especially with respect to vehicle dynamics, these bounds are not concurrent with low signal levels. (To be exact the error estimates should be correlated with the descent profile as the error sources are functionally related to the flight history) Secondly, the selection of the optimum smoothing function requires specific inputs pertaining to the guidance law, vehicle dynamics, etc. The thermal noise errors are graphically plotted as a function of smoothing time in those instances where smoothing in excess of that performed by the analog tracking circuitry is required to satisfy the specifications. Errors for the beacon assisted descent are evaluated first.

6.1.1 Coarse Range

Accuracy at ranges beyond the fine range ambiguity resolving capability of the beacon tracking radar is established by the coarse ranging mode. Coarse range is given by

$$R = \frac{c}{4\pi\Delta f}\Delta\phi_m - \frac{cf_o}{4\pi\Delta f\, f_c}\Delta\phi_c \qquad (1)$$

where

R = coarse range

c = velocity of propagation

f_o = modulating frequency at sweep limit (before sweeping)

Δf = sweep interval

f_c = X-band carrier frequency

$\Delta\phi_m$ = modulation phase change in an arbitrary time interval encompassing the sweep

$\Delta\phi_c$ = carrier phase change in same time interval

The system parameters selected for the error evaluation are:

Transmitter power	100 mw
Radar antenna aperture (angle track at half power point)	0.6 m
Transponder antenna gain	11 db
Receiver noise figure	11 db

Losses	10 db
Sweep interval (Δf)	150 kc
Carrier channel effective bandwidth	200 cps
Subcarrier channel effective bandwidth	1000 cps
Data extraction effective bandwidth	470 cps

The error equation for coarse range is

$$\epsilon_R = \frac{\partial R}{\partial \Delta f}\epsilon_{\Delta f} + \frac{\partial R}{\partial \Delta \phi_m}\epsilon_{\Delta \phi_m} + \frac{\partial R}{\partial f_o}\epsilon_{f_o} + \frac{\partial R}{\partial f_c}\epsilon_{f_c} + \frac{\partial R}{\partial \Delta \phi_c}\epsilon_{\Delta \phi_c} \qquad (2)$$

Error coefficient relations and magnitudes are

$$\frac{\partial R}{\partial \Delta f} = \frac{-R}{\Delta f} = \frac{-R}{1.5} \times 10^{-5} \text{ meters/cps}$$

$$\frac{\partial R}{\partial f_o} = \frac{-\Delta R}{\Delta f} = \frac{-\Delta R}{1.5} \times 10^{-5} \text{ meters/cps} \qquad (3)$$

$$\frac{\partial R}{\partial f_c} = \frac{f_o \Delta R}{f_c \Delta f} = \frac{-4}{1.5}\Delta R \times 10^{-11} \text{ meters/cps}$$

$$\frac{\partial R}{\partial \Delta \phi_m} = \frac{c}{4\pi \Delta f} = 159 \text{ meters/rad}$$

$$\frac{\partial R}{\partial \Delta \phi_x} = \frac{-cf_o}{4\pi \Delta f\, f_c} = 0.067 \text{ meters/cps}$$

where ΔR is the change in range during a coarse range measurement.

The error budget (3σ values) given below in Table 6-1 is calculated for a range of 30.5 km. ΔR is taken to be 1.8 km corresponding to a sweep interval of 3 seconds and an expected range rate of 0.6 km/sec at this range.

Table 6-1. Beacon Tracker Coarse Range Error Estimate

Item		Uncertainty	Range Error
Δf		3×10^{-5}	0.9
f_o		3×10^{-5}	1.5
f_c		3×10^{-7}	negl.
$\Delta\phi_m$			
	Thermal Noise	4.4 degrees	12.2
	Instrumentation	0.2 degrees	0.6
	IF (sweep error)	0.1 degrees	0.3
	Tracking Error	0.5 degrees	1.4
	Oscillator Phase Noise	2.6 degrees	7.3
$\Delta\phi_c$		360 degrees	0.4
	3σ RSS Total (with thermal noise)		14.4 meters
	3σ RSS Total (without thermal noise)		7.7 meters

In the above tabulation, oscillator frequency uncertainties are consistent with the performance of present STELATRAC equipment. The 470 cps effective bandwidth of the post detection ranging circuitry is necessary to accomodate the phase rate resulting from the three second sweep at the maximum range of 700 km. Instrumentation errors are those measured for the breadboard STELATRAC data extraction which is fundamentally similar to the proposed data extraction equipment. Tracking errors are based on present receiver designs. The oscillator phase noise errors are extrapolated from STELATRAC measurement data.

The error budget above indicates that ambiguities can be resolved somewhat in excess of 30 km, i.e. range can be resolved if the error is less than 19 meters. Accuracy of the coarse range data is slightly better than 0.05% since the parameter dependent and fixed errors are essentially negligible in the region where ambiguities cannot be resolved.

6.1.2 Fine Range

Ranging accuracy within the region where ambiguities may be resolved is determined by the calibration stability of the receiving system operating in the fine range mode. Fine range is given by

$$r = \frac{\lambda_m}{4\pi} (\phi_m - 4\pi n) \qquad (4)$$

where

r = fine range

λ_m = modulation (ranging signal) wavelength

n = number of complete wavelengths encompassed in the range interval R

ϕ_m = modulation phase

The error in fine range is

$$\epsilon_r = \frac{\partial r}{\partial f_m} \epsilon_{f_m} + \frac{\partial r}{\partial \phi_m} \epsilon_{\phi_m} \qquad (5)$$

where

$$\frac{\partial r}{\partial f_m} = \frac{-r}{f_m} = \frac{-r}{4} \times 10^{-6} \text{ meters/cps}$$

$$\frac{\partial r}{\partial \phi_m} = \frac{c}{4\pi f_m} = 0.1 \text{ meters/degree}$$

The first term of the error relation is entirely negligible at ranges where fine range accuracy is required. Receiving system stability, thermal noise, and instrumentation are the only error sources of concern. Analyses have shown that, at worst, stability of the receiving system over a 30-day period and over a wide temperature range will be less than 0.6 meters. These calculations are primarily based on experimental test results of components in the STELATRAC feasibility demonstration equipment. Test results of STELATRAC to date have been well within this predicted upper bound. Fine range instrumentation errors are easily held within a few degrees. Likewise, thermal noise causes a negligible error inside the region where the specified accuracy of the sensor is one meter. Thus, a bias accuracy of 1 meter can be achieved.

6.1.3 Range Rate

Range rate determination by measuring the doppler shift of the X-band carrier is inherently a very accurate process. It has been demonstrated in the STELATRAC feasibility equipment that doppler accuracy does not degrade up to the very point where thermal noise causes the tracking receiver to break lock. The accuracy limitations in the STELATRAC equipment are uncertainty in knowledge of the doppler bias and the quantization error. For a 0.5 second data extraction interval, the latter is 0.006 m/sec rms (without doppler scaling).

Doppler bias accuracy is established by the relative stability of the reference oscillators in the receivers. For stabilities which are realized without oven thermal control, say one part in 10^5, the rate error is less than 0.03 m/sec. A comparable amount of error could occur due to oscillator calibration inaccuracy. It is thus seen that the 0.15 m/sec range rate specification is easily met.

6.1.4 Angle and Angle Rate

The following error estimates for angle and angle rate are based on a typical design for a space stabilized angle tracker.* Sequential lobing is performed by electronic phase shifters in the antenna feeds. The lobing modulation is detected coherently since the necessary carrier reference is available from the phase-locked receiver which is part of the ranging system. The general characteristics of the angle tracker are:

Effective Bandwidth of Angle Servo	2.6 cps
Velocity Error Coefficient	
Tracking Loop	40 sec^{-1}
Stabilization Loop	200 sec^{-1}
Antenna Slope Factor (0.6 meter aperture and operation at 3 db crossover point)	0.29 $\frac{ratio}{degree}$

Tracking error estimates are based on the following maximum performance requirements.

Line-of-sight angle rate	$6^\circ/sec$
Line-of-sight angle acceleration	$0.6^\circ/sec^2$
Vehicle Angle rate	$6^\circ/sec$
Vehicle angle acceleration	$3^\circ/sec^2$

The error in angle due to thermal noise is evaluated from

$$\sigma_\theta = \frac{\sqrt{\Phi B_n / S}}{K_d} \quad (deg) \qquad (6)$$

*9752-0005-MU-000, CW X-Band Radar Development" Interim Report No. 1, Space Technology Laboratories, Inc., 1 June 1961.

where

I = the spectral density of the noise referred to the antenna

S = signal power

B_n = effective bandwidth of the angle servo

K_d = antenna slope factor $(\frac{\text{ratio}}{\text{degree}})$

Tracking errors are evaluated using the above error coefficients and the tracker transfer functions of the cited reference. A tabulation of the antle errors is shown in Table 6-2. Bounds are given for many of the errors since in most cases, only performance limits are presently known. The thermal noise error shown is calculated for the maximum range case (700 km) after smoothing for one second. It decreases proportional to range, since signal power increases in an inverse proportion to range squared for a beacon system. The angle data, if smoothed, exceeds the desired tolerance of 0.3 degrees. However, smoothing of one-half to one second, which is certainly permissible at long ranges, brings the angle error into tolerance.

Angle rate errors are primarily due to thermal noise. These are shown in Figure 6-1 as a function of smoothing time. It is seen from Figure 6-1 that the rate error at maximum range is sizable compared with the desired accuracy of 0.03 degrees/sec. However, smoothing up to ten seconds is estimated to be feasible at long ranges, whereas only six seconds is necessary for the present system parameters. At close ranges, one- or two-second smoothing will suffice.

Table 6-2. Angle Error Estimate (3σ)

Item	Error Magnitude
Thermal noise (raw tracker data smoothed for 1 second)	<0.13*
Instrumentation	
Angle tracker	0.03
Boresight shift due to drift in conical scan pattern phase shifter	<0.09
Gyro drift	negl.
Data pickoff error	0.02
Boresight error	0.06
Multipath	<0.06
Tracking errors	
Vehicle angle rate	zero
Vehicle angular acceleration	negl.
Line-of-sight-angle rate	<0.15
Line-of-sight angle acceleration	<0.15
3σ Angle Error Bound, RSS Total	<0.28 degrees

*Decreases proportional to range. Value given is for 700 km.

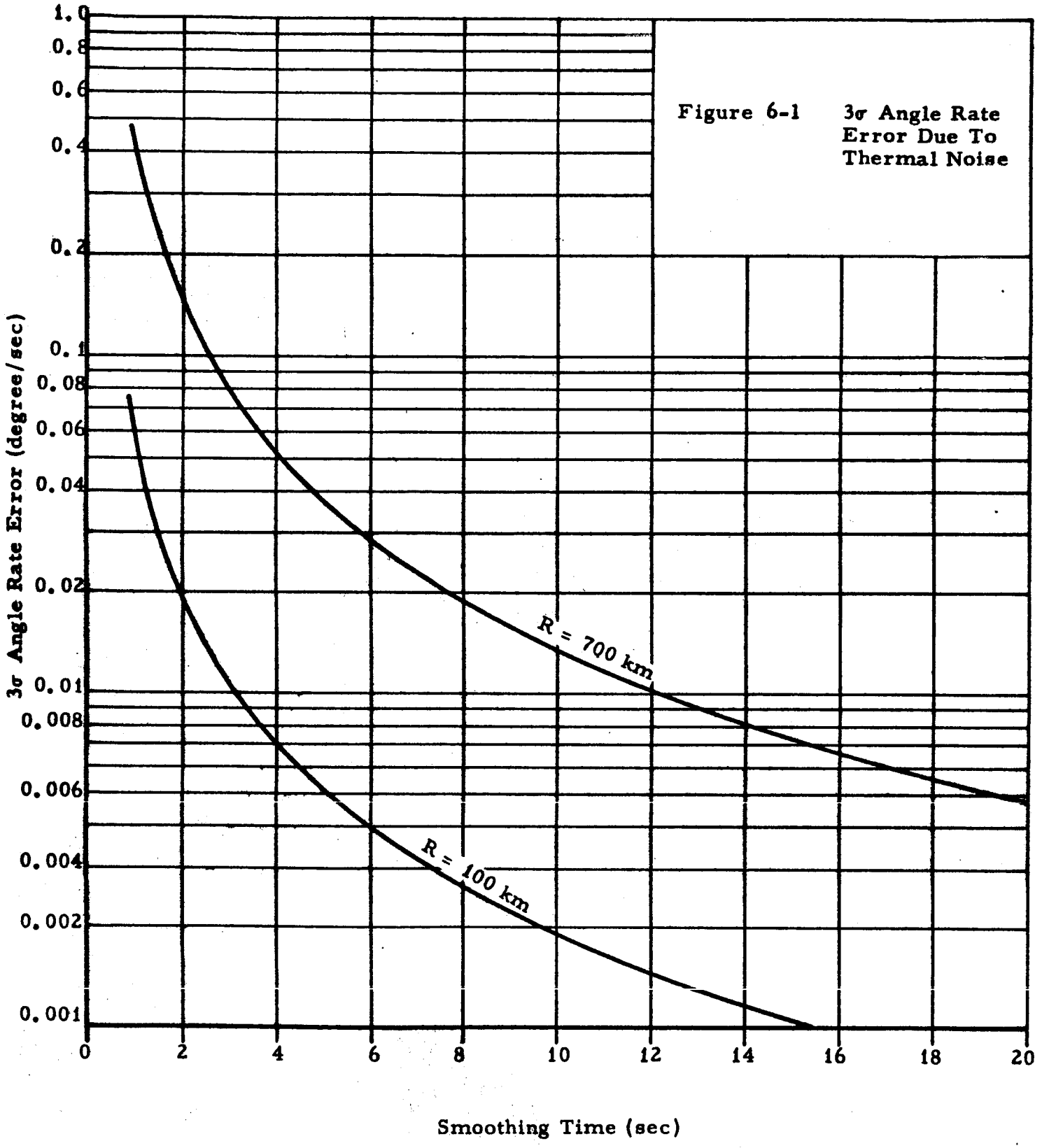

Figure 6-1 3σ Angle Rate Error Due To Thermal Noise

6.2 EXTENDED RANGE ALTIMETER

Section 4.2 gives the relations and system parameters needed for estimating the altimeter errors. Extraction of altitude from the measurements involves only a scaling of the pulse repetition period, i.e., multiplying by one-fourth the propagation velocity. Thus the error in altitude is simply a direct combination of the individual PRF errors produced by the electronic system.

Many of the error magnitudes are tabulated as bounds on the error as the system parameters vary with altitude and a single set of error estimates is not exact. Similar complications arise due to the fact that only certain performance maximums are known and errors such as those due to the tracking characteristics of the PRF servo depend not only on these maxima but on the complete time history. A complete error profile must await a simulation study of the PRF tracker, partially due to the fact that simplifications were found necessary to make the design and error analysis problem tractable. Also certain errors which depend on the detailed intricacies of circuit components cannot be assessed analytically and their effects must be evaluated experimentally. Lastly, little is known about the lunar surface in the statistical detail necessary for an evaluation of errors arising from this source.

Table 6-3 shows the error estimates or bounds derived for an altimeter compatible with the present STELATRAC equipment. As indicated by the explanatory captions following Table 6-3 a longer data time (17 seconds) would permit the fulfillment of the specification on altitude determination under the worst case conditions assumed. However, as discussed in Section 4.2.2.1 the assumed lunar scattering coefficient of -10 db is quite pessimistic so that a much smaller smoothing time may suffice.

It is expected that all sources of error not evaluated in Table 6-3, other than the terrain error, will be insignificant. If it is found that the present design is too sensitive to amplitude scintillation, the tracker can be operated at a multiple of the PRF once the altitude ambiguity is resolved. This would provide more samples to determine the PRF control loop error signal and thus reduce sampling noise and improve the error sensitivity of the PRF tracker.

Table 6-3. Solid-State Extended Range Altimeter Error Estimate

Item	Error Magnitude
Thermal Noise Error (at 220 km)	$< 2.1\%$*
Instrumentation	
Synchronous Demodulator Drift and Zero Set (5 mv)	0.01%
Integrating Amplifier Drift	
Temperature (0.4 mv, 25°C variation)	0.008%
Aging (0.7 mv, 30 days)	0.015%
PRF VCO Noise	. . .**
Gating Error (estimated)	1.5 meters
Receiver Errors	. . .**
Dither Errors	$<0.02\%$
Data Processing	0.1%
Terrain Error (amplitude scintillation)	. . .***
Tracking Errors****	
Static Error	$<0.05\%$
Velocity Error	$<0.05\%$
Acceleration Error	$\leq 0.05\%$
RSS Total 3σ error with thermal noise	$<2.1\% \pm 1.5$ meters
RSS Total 3σ error without thermal noise	$<0.14\% \pm 1.5$ meters

*Diminishes as h for constant tracker bandwidth, however, the bandwidth increases as $1/\sqrt{h}$ according to present analysis. A computer simulation for a typical family of altitude profiles is required to confirm the analysis. The 0.5% specification can be realized by a data smoothing of 17 seconds for example, at maximum altitude.

**Believed to be negligible relative to the 0.5% desired accuracy. Requires experimental verification.

***A tentative analysis of the terrain amplitude scintillation spectrum has been completed. However, further study is required to confirm the approximations and numerically evaluate.

****Tracking errors have been set low purposely to allow for higher performance spacecraft and for some variation in tracker gain due to the time delay term. Further compromise in this area may be advisable to reduce thermal noise error.

Data processing via digital techniques was investigated. For digital measurement purposes, the dither rate and the amount of dither are not too significant as long as the following conditions are satisfied:

1. The sample period is a multiple of the dither rate.
2. A signal designating the times the dither frequency is switched is provided.

Two ways for determining the frequency of the PRF were evaluated. They were 1) (N count) measuring the cycles per unit time and 2) (phase measurement) measure the period of one cycle. A measurement accuracy of 0.1 percent can be achieved with state-of-the-art circuits, i.e., highest frequencies to be processed are below 4 mc.

6.3 SLANT RANGE TRACKER - VELOCITY METER

Section 4.2 gives the relations needed for estimating the errors due to electronic portions of this sensor while system parameters and the composition of errors from other sources are given in Section 4.3. Section 4.4 covers the terrain bias and sidelobe error investigations.

Many of the errors vary as complicated functions of the position of the velocity vector relative to the vehicle and the lunar surface. In order to get a complete description of the errors and their variations along the descent trajectory in the desired coordinates, a machine computation is required. The complications of providing error estimates for the slant range tracker are essentially the same as those pointed out in the case of the high altitude altimeter. Therefore, only bounds can be given for the majority of the errors for both the velocity meter and slant range tracker (long range mode). The only significant error for the slant range tracker operating in the low altitude mode arises from the phase instability of the receiver. The calibration stability of the receiver is based on experimental test results and analysis of the STELATRAC equipment.

Table 6-4 shows a tabulation of the error estimates or bounds for all portions of the equipment. The velocity errors are given in the coordinates of the velocity meter. Channel 1 is associated with the beam directed along the vehicle longitudinal axis and channels 2 and 3 are offset by 20° from the longitudinal axis in orthogonal planes.

Table 6-4. Error Estimates, Slant Range Tracker-Velocity Meter

Velocity Errors	Error Magnitude	
	Slant Range Channel (No. 1)	Channels No. 2 and No. 3
Thermal Noise	0.015%	0.008%
Instrumentation		
Integrating amplifier drift	<0.02 m/sec	<0.02 m/sec
Discriminator drift	<0.02 m/sec	<0.02 m/sec
Reference oscillator drift	<0.005 m/sec	<0.005 m/sec
Channel cross coupling		
Thermal noise	. . .	0.008%
Bias or drift errors	. . .	<0.03 m/sec
Fluctuation Noise	. . .	<2.1%
Tracking error	. . .	<0.3 m/sec
Terrain bias	. . .	<0.15%
Sidelobe errors	negl.	negl.
Fluctuation noise (raw tracker data)	<4.2%	<2.1%
Terrain bias(20° incidence, velocity along beam)	<0.15%	<0.15%
Tracking errors		
Static error (VCO drift and doppler offset)	<0.09%	<0.03 m/sec
Dynamic lag (<60 sec sustained acceleration)	<0.3 m/sec	<0.3 m/sec
Antenna alignment and environment errors (3σ error of 0.5° in all angles)	0.4%	0.16%
3σ RSS Totals(raw data)	~4.2% ± <0.32 m/sec	<3.0% ± <0.43 m/sec
3σ RSS Total Random Error with 0.5 sec smoothing *	~0.7%	<0.4%

*A detailed acceleration profile and properly matched polynomial constrained filter must be known to give a meaningful estimate of the actual lag error for this degree of smoothing. The remaining errors are independent of smoothing time and are essentially negligible relative to the 0.5 m/sec desired accuracy.

Table 6-4. (contd)

Range errors

a) PRF Tracking mode

	Error Magnitude
Thermal Noise	$<0.75\%$*
Instrumentation	1.5 meters**
Terrain Bias (20° incidence)	$<0.06\%$
Tracking Errors(all sources for design criterion of 0.1% maximum error each source)	$<0.17\%$
Terrain Noise	*** . . .
3σ RSS Total	$<0.77\% \pm 1.5$ meters

b) Low Altitude Mode

	Error Magnitude
Calibration Stability	0.6 meters
Thermal Noise	negl.
Error due to drift of modulation frequency	negl.
Terrain Error	negl.
3σ RSS Total	0.6 meters

*See Note * of Table 6-3

**See Instrumentation Errors of Table 6-3

***See Note *** of Table 6-3

7. PHYSICAL AND ELECTRICAL CHARACTERISTICS

The weight, volume, and power estimates of the beacon tracker-extended range altimeter and slant range tracker-velocity meter are tabulated in Table 7.1. In each case, the estimate is based on the system as it would be when flight packaged.

Table 7.1

Lunar Sensor Weight, Volume, and Power Estimates

System	Weight	Volume	Power
Beacon-assisted			
Beacon radar transceiver	17.1 lbs	.0105m^3	34 watts
Beacon radar antenna	23 lbs	N/A	35 watts
Transponder transceiver	15.5 lbs	.0095m^3	30 watts
Transponder antenna	1 lb	N/A	Zero
Nonbeacon-assisted			
Extended range altimeter transceiver	17.9 lbs	.0107m^3	33 watts
Extended range altimeter antenna	(uses common antenna with beacon tracker)		
Slant range tracker - velocity meter transceiver	20 lbs	.0125m^3	48 watts
Slant range tracker - velocity meter antenna	4 lbs	N/A	Zero

The flight packaged systems have modular construction, each module employing miniaturized circuit techniques for the transistorized portions of the systems, and waveguide and coaxial line construction for the r-f portions. Welded cordwood packaging techniques were assumed for circuitry operating at frequencies below 100 kc, and two-dimensional circuits are assumed for circuits operating at intermediate frequencies. The two-dimensional circuits, although much less dense than the cordwood constructed circuits, permit the necessary component shielding. Examples of a cordwood package and a two-dimensional package are illustrated in Figures 7-1 and 7-2 respectively.

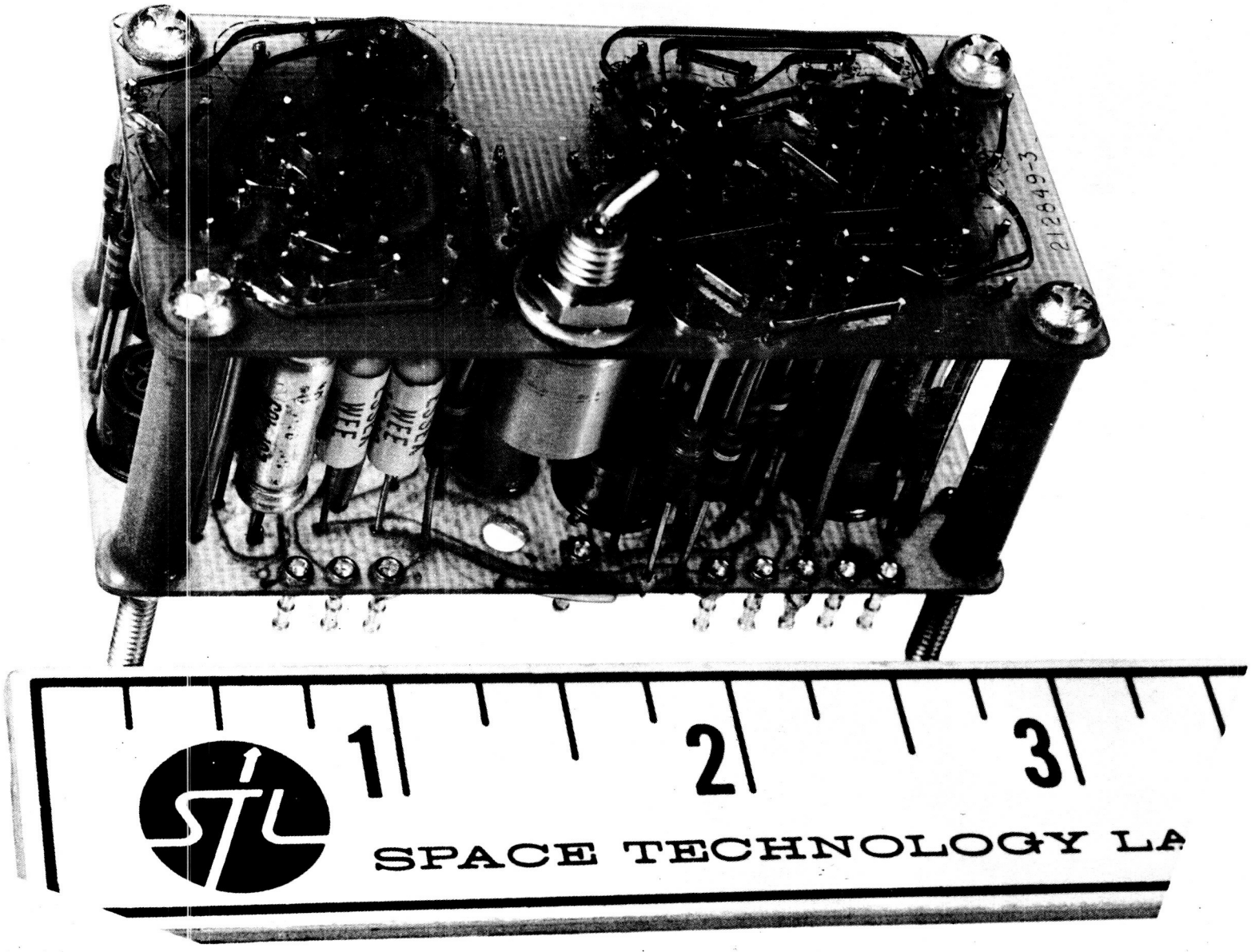

Figure 7-1. Dual Integrator Networks
(Cordwood Construction)

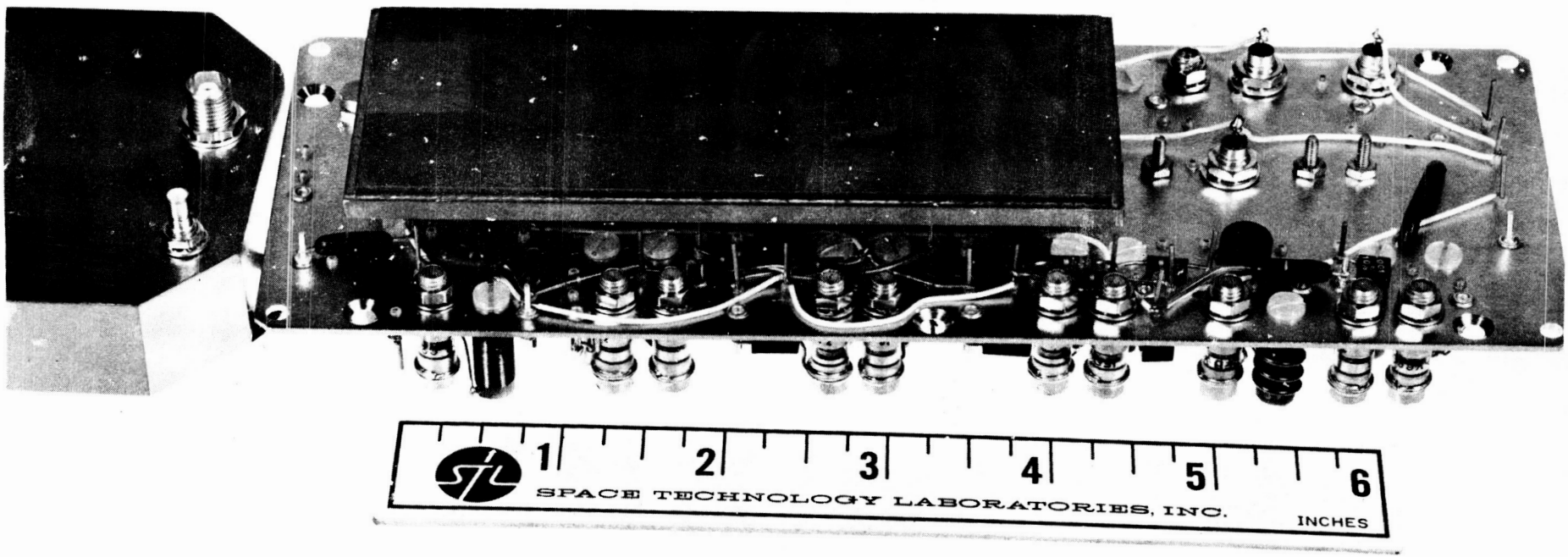

Figure 7-2. Multiplier and 107 MC Power Amplifier
(Two Dimensional Construction)

In order to provide the necessary shock and vibration protection for the electronic circuits, the units are partially potted, or conformally coated, with a suitable epoxy compound. This partial potting technique provides the necessary protection while contributing only a small increase in weight.

The weight and size estimates are based on an actual parts count of the STELATRAC beacon tracking radar feasibility model and on packaging densities representative of those achieved in STL's OGO and 823 programs for similar types of circuitry. The power estimates of the transceivers are based on the actual power consumed by the STELATRAC radar feasibility model. The parts count was appropriately modified to reflect the circuit additions and modifications necessitated by the specific system requirements.

Because the power converters associated with each system are normally considered to be a component part of that system, the weight, size, and power of the converters are included with that of its associated system. A 70-percent efficiency was assumed for each power supply, and the weights of each estimated to be, nominally, about two pounds.

8. RELIABILITY ASSESSMENT

8.1 INTRODUCTION

A numerical reliability assessment has been performed for the solid-state beacon tracking radar (STELATRAC), the extended range altimeter, and the slant range tracker-velocity meter as they would exist subsequent to flight packaging. The results of the analysis are shown in Table 8-1. Since the detailed mission profiles are not known, the data has been presented in terms of mean-time-between-failures (MTBF) rather than as probability of success.

Table 8-1. Reliability (MTBF) Estimates For Lunar Landing Sensors

System	MTBF (Hours) OGO Type Parts	Minuteman M-Level Parts
Beacon Assisted		
Beacon Tracking Radar	9,100	18,100
Beacon Tracking Radar Antenna (also used with the extended range altimeter)	14,835	18,221
Beacon	10,333	21,639
Beacon Antenna	282,486	282,486
Non-Beacon Assisted		
Extended Range Altimeter	9,700	21,200
Slant Range Tracker-Velocity Meter	6,600	13,800
Slant Range Tracker-Velocity Meter Antenna	211,864	211,864

The reliability results shown under "OGO Type Parts" were obtained using failure rates of existing parts, many of which are used in STL's Orbiting Geophysical Observatory assemblies. The "Minuteman M-Level" data is predicated on special reliability procedures, as outlined in "Minuteman Reliability Engineering Directive", Boeing Document D2-10744, dated January 1961. A detailed discussion of these failure rates and the associated environmental and packaging factors is contained in Sections 8.2 and 8.3, respectively.

If standard STL techniques and procedures for large programs (such as production of flight units) are followed, the potential reliability mentioned above can be achieved. It should be noted that "potential reliability" implies elimination of systematic and environmental problems, so that failure rates of component parts are typical of their proper application. The elimination of these problems, popularly known as "debugging", is generally not accomplished in initial packaging designs, but is generally dependent upon a development effort including implementation of a comprehensive reliability program (design reviews, specifications reviews, etc.).

The reliability estimates presented in Table 8-1 assume all components are in series and a failure of any component will cause system malfunction. This is a pessimistic premise, as all failures are not catastrophic. Redundancy is discussed in Paragraph 8.5.

8.2 RELIABILITY ANALYSES

The basic input information required to carry out the system reliability analysis is:

a. A count of all parts necessary to satisfactorily perform the required functions

b. Laboratory failure rates for these parts at applicable operating temperature and percentage of rated electrical stress

c. An environmental and packaging multiplication factor to convert laboratory failure rates to a packaged equipment spaceborne failure rate

d. Failure distribution functions to convert failure rates to probability of survival figures

The remainder of the Reliability Assessment Section will discuss these inputs and their effect on reliability.

8.3 PARTS COUNT

An accurate parts count of each of the three systems is presented in Table 8-2. The power converters are included in the parts tabulation of the respective units. In order to generalize, it was assumed that each system--the beacon tracking radar, the extended range altimeter, and the slant range tracker-velocity meter--operates independent of the other two. However, the extended range altimeter and the beacon tracker are integrated and use a common antenna, transmitter, r-f circuitry, and similar low frequency circuitry. Combining minimizes the component count in relation to the total for two independent units.

8.4 BASIC PARTS FAILURE RATES

Average laboratory failure rates for various part types are presented in Table 8-3. for the beacon tracking radar, extended range altimeter, and slant range tracker-velocity-meter. The heading of each column indicates the source of failure rates from which the data in the column is obtained, together with the appropriate average operating temperature and average percentage of rated stress. It should be noted that these failure rates are based on unassembled part failures and do not include the effects of packaging or operating environment. Factors to account for these effects are discussed in Section 8.5.

For the part type failure rates used in the reliability analysis, consideration was given to part failure data from several major programs. STL investigated the part type failure rate data used in industry and compared this information with its own data. This study has been concentrated on diodes, transistors, and carbon composition resistors, since these parts make up the majority of spacecraft electronic parts and billions of part-hours of data have been accumulated. Numerous sources of part failure rate data have been examined, together with the reliability procedures necessary to attain these rates. Some of these sources of data, together with historical average failure rate information are presented below in Table 8-4.

Table 8.2. Lunar Landing Sensors Parts Count Tabulated As Beacon-Assisted and Non-Beacon Assisted Mode

Parts Count	Transistor, Silicon	Diode, Silicon	Diode, Zener	Resistor, Carbon Comp.	Capacitor, Tantalum	Capacitor, Ceramic Glass	Capacitor, Trimmer	Transformer	Coil & RF Chokes	Thermister	Crystal	Resistor, Variable	Varactor	Feed Thru Capacitor	Circulator	Torque Motor	Angle Transducer	Waveguide Unit	Bearings	Ferrite Isolator	Rate Gyros
Assembly																					
Beacon Assisted																					
Beacon Tracking Radar	116	88	11	434	94	294	56	28	119	1	5	23	13	14	1			5		2	
Beacon Tracking Radar Antenna (Also used with the Extended Range Altimeter	42	28		171	11	58		9	12			5	8			2	2	7	4		2
Beacon	109	79	9	455	77	142	44	31	64	3	2	16	12	21	1			5		2	
Beacon Antenna																		3			
Non Beacon Assisted																					
Extended Range Altimeter	136	94	7	473	35	305	43	16	100	3	5	21	13	18	2			5		2	
Slant Range Tracker-Velocity Meter	257	163	11	986	153	557	50	20	170		7	31	14	12	4			5		2	
Slant Range Tracker-Velocity Meter Antenna																		4			

Table 8-3. Piece Part Failure Rate X 10^{-9}
Lunar Landing Sensors

		30°C and 25% Rated Stress STL/BTL (OGO)	30°C and 25% Rated Stress Minuteman M-Level *
Bearings		35	--
Capacitor:	Ceramic/Glass	5	1
	Tantalum	40	--
	Trimmer	40	30
Choke - RF		10	--
Coil		10	--
Crystal		76	--
Crystal Filter		304	--
Diode - Silicon		51	20**
Feed Thru Filter		70	--
Ferrite Circulator		1250	--
Ferrite Isolator		1250	--
Motor - Torque		500	--
Resistor - Carbon Composition		18	1
	Variable	58	--
Transformers		40	--
Transistors - Silicon		153	30
Varactor		51	--
Waveguide		590	--

* Minuteman M-Level parts as described in Minuteman Reliability Engineering Directive, Boeing Document No. D2-10744, Dated January 1961.

** For low stress computer applications use 4.

Table 8-4. Historical Average Failure Rates (Failures per 10^{-9} Hours)

Part Type	Diode	Transistor	Carbon Composition Resistor
RCA (1953)	300	400	200
STL (1955)	150	450	20
BTL/STL (1959)	50	150	18
Atlas Ground Computer (1959)	50	120	4
Titan Ground Computer (1961)	1	10	1
Minuteman M-Level (1963)	4	30	1

The BTL/STL electronic part* failure rates used in this analysis were initially presented by Bell Telephone Laboratories and subsequently updated by STL to reflect advances in component state-of-the-art. The failure rates for the Titan Ground Computer are statistically significant, as can be seen from the following chart of Failures vs. Operating Time, collected between February 1957 and July 1961.

	Operating Time (Billion Hours)	Failures
Diodes	1.73	2
Transistors	0.22	2
Resistors	1.55	1

Achievement of the Titan Ground Computer Failure rates requires a low electrical stress, an intensive reliability program, and circuits which are not affected by large variations in part tolerance.

---

*Failure rates for electromechanical and mechanical parts were obtained from the Martin Company Reliability Application and Analysis Guide, MI-60-54(Rev. 1, July 1961.

8.5 FAILURE RATE ENVIRONMENTAL FACTOR

The failure rates discussed in the previous paragraph are appropriate to a laboratory environment without packaging space restrictions. A factor of 2.0 has been used to convert these electronic part failure rates to packaged equipment in a translunar environment. This allows a 100 per cent increase in laboratory failure rate to account for packaging restrictions and space environment. To date there is insufficient data to statistically verify a 2.0 factor, but it is clear that factors are implied and STL considers for packaged equipment in space the range will be between 1.0 and 3.0. No additional degradation has been assumed for launch or landing.

8.6 AREAS OF POTENTIAL IMPROVEMENT

As indicated in Table 8-1 a significant improvement in the estimated reliability of the extended range altimeter, the beacon tracking radar, and the slant range tracker-velocity meter electronics results if parts having the Minuteman M-Level failure rates are used. However, undertaking such a program would increase the cost appreciably.

Another method of improving reliability is through redundancy. This can be accomplished via designed-in redundancy or, using a general definition of the term via on-board maintenance and component replacement. Either approach implies increased weight, size, and power some place in the spacecraft. However, this is a most fruitful area and requires detailed investigation when mission and operational profiles are established, as there are many system tradeoffs involved.

An interesting feature of the STELATRAC beacon tracking radar approach permits redundancy in any of the range, range rate, and angle channels with the addition of lightweight receiver modules. This capability exists due to the double sideband modulation employed. A separate receiver channel can process each sideband so that failure of receiver circuitry in one channel would not be catastrophic. No complex switching logic or sensing instrumentation is required to implement this capability.

8.7 RELIABILITY COMPARISONS, DIFFERENT BEACON TRACKING RADAR ANTENNA CONFIGURATIONS

A reliability analysis was made to determine the preferred form of angle sensing implementation based exclusively upon reliability considerations. The types of antenna configurations evaluated are typified by the following:

1. A conically scanning antenna gimbaled and space stabilized. The conically scanning beam is assumed to be electronically controlled via varactor diode phase shifters.

2. A body-fixed interferometer antenna. In order to meet the requirements of antenna gain and angle sensing accuracy, the three elemental antennas composing the array are separated by greater than one wavelength. This condition permits ambiguous angle data to be obtained from the system, necessitating a method for ambiguity resolution. This was provided for purposes of the comparison by adding an electronically scanning antenna to the interferometer system. The electronically scanning antenna is assumed to be the same type as the conically scanning antenna, but having a larger antenna beamwidth. The arrangement possesses sufficient accuracy for ambiguity resolution purposes.

3. An interferometer antenna, gimbal mounted. The interferometer antenna is assumed to be identical to the aforementioned one, including the electronically scanning ambiguity resolving array, except that it is mounted on a nonstabilized gimbal structure. This configuration is included principally for comparative purposes, but could be of importance if large search angles are required.

The reliability potential of each of the systems is presented in Table 8-5 in terms of an MTBF estimate of the antenna plus the associated angle sensing circuitry.

Table 8-5

System	MTBF-OGO Type Parts	MTBF-Minuteman M-Level Parts
Conical Scan Antenna, Gimbaled and Space Stabilized	14,800 hours	18,200 hours
Interferometer Antenna, Body-Fixed	15,000 hours	40,600 hours
Interferometer Antenna, Gimbaled, without Space Stabilization	12,500 hours	26,300 hours

The MTBF values for the different systems indicate that there is no definite advantage, from a reliability standpoint, of any one of the configurations over any other for OGO type components. If Minuteman M-Level components are used, the body-mounted interferometer antenna is the more reliable system.

A further point that should be considered in comparing the reliabilities of the three antenna configurations is the relative complexity of the computer circuitry necessary to process the data from each configuration. The angle data from the gimbal angle pickoff is directly usable in comparison to the angle data from an interferometer system. Thus, more computer capacity is required by the interferometer configuration, which tends to reduce the overall reliability of the angle sensing data.

Obviously, the weight and power consumption of the antenna system is least for the fixed configuration and highest for the gimbaled, space-stabilized unit. However, overall system weight and power may not be so ordered due to differences in antenna gain.